Theoretical and experimental study of wave propagation in brass musical instruments

Jonathan A Kemp

A thesis submitted in fulfilment of the requirements

for the degree of Doctor of Philosophy

to the

University of Edinburgh

2002

Abstract

The concept of input impedance is a very useful representation of the resonance characteristics of an acoustic horn. A large part of this work discusses its theoretical and experimental determination. It is demonstrated that higher modes, waves with a non-uniform pressure distribution on the plane perpendicular to the axis of the instrument, should be used in the theory of wave propagation in musical instruments featuring a flared bell as an improvement on assuming plane wave propagation.

The impedance at the output end of an acoustic horn is known as the radiation impedance. The existing method for the calculation of the multimodal radiation impedance of a cylindrical tube terminated in an infinite baffle is reviewed. New work is then presented for the calculation of the radiation impedance of a rectangular duct terminated in an infinite baffle. An existing method for calculating the input impedance of an acoustic horn of cylindrical cross-section starting from the radiation impedance is utilised. The method is then formulated for horns of rectangular cross-section. Pressure field calculations are also presented.

In acoustic pulse reflectometry an acoustic pulse is directed into the object under test and the sampled reflections analysed to provide the internal profile and the input impedance. It is shown that better agreement is observed between the experimental and theoretical input impedance when higher modes are included in the calculation.

Currently the bore reconstruction analysis assumes plane wave propagation since this provides a simple formula for the frequency independent reflection and transmission coefficients at changes in cross-section in a pipe. The multimodal reflection and transmission coefficients are, however, frequency dependent. A higher-mode method is presented to calculate the reflection of an impulse with the aim of improving the technique's accuracy for horns which feature a large rate of flare at the end. Digital filters designed to represent losses and cancel reflection from the sound source are also shown to increase accuracy and make possible the measurement of longer objects.

Declaration

I declare that this thesis has been composed by me and that the work is my own.

.....

Acknowledgments

A big thank you goes to my supervisors, Prof. Murray Campbell and Prof. Clive Greated for their help and support. I would like to acknowledge Dr. Noam Amir of Tel Aviv University who provided the inspiration for many theoretical aspects of the work. Discussions with Dr. Maarten van Walstijn, Dr. David Sharp and Dr. Jim Buick were also invaluable. I thank Dr. Sarah Sneddon for proof reading.

My office friends and colleagues past and present in the fluids and acoustics group (known as Susan's gang) deserve a hand. That's Sandra, Seona, John C_1, Calum, Steve, Ted, Mark, Orlando, Maarten, Dave S_2., Alan, Khurom, Jim, Tom, Anthony, Shona, Susan, Scott, Dave F., Dawn, Smir, John C_2, Jon, Howard, Craig, Adrian, Dave S_1., Alix, Arny, and Naz in order of distance from my desk. Cheers too for the staff of the School of Physics' electronics and mechanical workshops.

I would like to thank the School of Physics cricket team (E=MCC). Thanks go to the guys from Teannaich ceilidh band: Mark, Andrew, Colin and Mike.

Thanks also to Mum, Dad, Joanna, Sarah, Grant and my grandparents.

This work was funded by the Engineering and Physical Sciences Research Council (EPSRC).

Contents

List of Figures

List of Tables

Chapter 1

Introduction to the study of wind instrument acoustics

1.1 Background

The physical principles responsible for the sound we hear from musical instruments have been the subject of study since ancient Greek times. As the physical sciences developed, wave motion was used to explain the behaviour of water and light in addition to the production of audible sound. Frequency analysis techniques were developed illuminating the sensations of pitch and tone. The arrival of accurate microphones and sound reproduction equipment allowed quantitative experimental measurement of the resonance characteristics of musical instruments. With the invention of the computer, numerical methods became available

for predicting the properties of musical instruments, to confirm the accuracy of the wave motion theory and to analyse how suggested changes in an instrument would effect the playing properties.

This work concentrates on brass musical wind instruments. The sounds we hear from such instruments result from wave motion caused by rapid compressions and expansions of the air inside the tubing. We begin with a qualitative explanation of the acoustic behaviour of air columns. This discussion will show how a quantity called the input impedance can provide information on the playing frequencies of brass musical instruments. This quantity, along with the internal profile, will be investigated both experimentally and theoretically in the body of work which follows.

1.2 Acoustic resonance

Consider a cylindrical pipe open at both ends. We define the acoustic pressure as the difference between the air pressure and the equilibrium atmospheric pressure. To a first approximation the acoustic pressure is zero at the open ends of the tube. The acoustic pressure inside the air column, however, may be non-zero and change with time. The air column can therefore contain standing waves giving a sinusoidal pressure amplitude along the length of the tube such that an integer number of half wavelengths fit into the tube length.

This condition is obviously fairly crude since it ignores the radiation of sound from the ends of the tube. However, in reality, the acoustic pressure amplitude is generally much higher in the tube than outside, meaning that this condition gives a reasonable first approximation for the wavelengths of sound which lead to resonance. These standing waves have frequencies which are integer multiples corresponding to the set of musical pitches we call the harmonic series. The harmonic series consists of a fundamental, the pitch an octave above the fundamental, the octave and a fifth (or twelfth) above the fundamental, the double octave above the fundamental and so on.

Now going on to consider a cylindrical pipe open at one end and closed at the other, our first approximation indicates that the pressure is only required to be zero at the one open end. The air column can therefore contain standing waves such that an odd number of quarter wavelengths fit into the tube length. The fundamental has a frequency half that of a tube of the same length open at both ends and the frequencies are the odd components of the harmonic series.

1.3 Exciting the air column

In order to create a musical sound in a wind instrument the player blows air into some sort of excitation mechanism. For the clarinet and saxophone this consists of a single piece of reed mounted onto the mouthpiece with a small gap between.

Increasing the air pressure in the mouth cavity initiates an oscillatory regime with the reed opening and closing the gap, periodically letting air flow into the instrument to support pressure standing waves in the air column. The oboe and bassoon feature a double reed, with the gap between two pieces of cane regulating the flow.

When brass musical instruments are played, the player's lips are stretched across the mouthpiece. The lips behave much like the reeds of woodwind instruments, therefore brass instruments are said to have a lip reed mechanism. The operation of this lip reed can be understood by considering the forces acting on the lips and the pressure field in the instrument.

There are two simplified models which help to explain lip reed action, called the inward and outward striking reeds [1]. Obviously a brass player's lips will blow open if the mouth cavity pressure is sufficiently large. A reed which follows this behaviour is called the outward striking reed. On the other hand a high pressure in the mouth will lead to air moving in the gap between the lips, lowering the pressure there. The lips are thus sucked together, experiencing a force known as the Bernoulli force. This is what we refer to as an inward striking reed. The actual nature of the lip reed is the study of current research, as reviewed in Campbell [2]. The results seem to suggest that the lip reed can behave more like inward or outward striking reeds depending on the resonance frequencies of the lips and of the air column.

1.4 Input impedance

The pressure standing waves in a brass musical instrument have a pressure antinode at the mouthpiece end. This indicates that the lips effectively close the mouthpiece end of the instrument. If the air column of the instrument was cylindrical then the resonance frequencies would be the odd components of the harmonic series. However, brass instruments have internal profiles which expand along their length meaning that the mode frequencies are raised, with the lower modes being raised to the largest extent. The flare of the bell is designed to bring the resonances into an approximately harmonic relationship. The exception is the lowest resonant frequency which is lower than it would be for a true harmonic relationship in instruments with a significant amount of cylindrical tubing such as the trumpet and trombone.

As discussed previously, an oscillating volume velocity is put into the instrument through the lips to support the resonance. A small fraction of the energy in the pressure oscillations in the instrument's air column will be transmitted out to the surrounding air. These pressure waves are audible to the player and listeners as musical notes at the pitch corresponding to the frequency of the excitation. Valves and tuning slides are often included to enable the player to alter the length of the air column and therefore change the resonances.

Sound can be produced by skilled players at any of the resonant frequencies or

at a frequency slightly away from a resonance by careful control of lip tension. It should also be noted that the velocity source at the lips will in practice have many harmonically related frequency components. The amplitude of the impedance at these frequencies will then influence the pitch and harmonic content of the resulting sound. For instance, well-tuned, harmonically related resonance peaks will mean more harmonic content and a brighter tone.

If the frequencies present in the excitation are all well away from resonant frequencies, very low sound levels will result and in practice the reflections of sound within the instrument will force the lips of the player to change their oscillations to play at a frequency where components of the excitation are supported by air column resonances. As mentioned before, the resonance frequencies of the trumpet and trombone are close to being harmonically related, except the lowest resonance which is flat (ie. lower in frequency than would be required for a harmonic relationship). If the player excites the instrument at the frequency of this bottom resonance the note is weak because the upper harmonics are not supported by resonances. However, if a note is played such that the harmonics in the excitation match the harmonically related resonances, the note is strong. This is known as the pedal note. Note that the pitch perceived by a human listener is the same as that for a sinusoidal oscillation at the fundamental of the harmonic series even when the component of the fundamental actually present in the sound is very weak.

In order to characterise the behaviour of an instrument we use a frequency dependent quantity called the input impedance. The input impedance is the ratio of the pressure and volume velocity at the input or mouthpiece end. In terms of brass instruments this means the input impedance gives a measure of the sound pressure amplitude in the mouthpiece due to a given amplitude of sinusoidal excitation created by the varying flow of air between the lips. A plot of input impedance against frequency will have peaks at the resonance frequencies. The sharpness of the peak also indicates information a player can recognise. The sharper a peak is, the easier the resonance will be to play and the more difficulty a player will experience in attempting to play at a frequency slightly away from the resonant frequency.

1.5 Input impedance measurement techniques

1.5.1 Frequency domain measurement

Accurate experimental measurement of the input impedance was first achieved by closing the mouthpiece with a flat plate containing a small capillary and a microphone [3, 4, 5]. The capillary feeds a known sinusoidal volume velocity into the mouthpiece and the microphone measures the pressure response. The input impedance is deduced from the ratio of the measured pressure and volume velocity. We call this a frequency domain experiment since it must be repeated for

each frequency of interest. Recent developments in the field of frequency domain excitation include the use of a chirp signal which consists of a sinusoid of rapidly changing frequency. All frequencies of interest may then be measured in a short time interval.

1.5.2 Acoustic pulse reflectometry

The alternative to frequency domain measurement is to measure the time domain response, for instance, by acoustic pulse reflectometry. The history of this technique has been reviewed in detail in the thesis of Sharp [6]. A summary is presented here.

Acoustic pulse reflectometry was at first developed as a technique for the study of the earth's crust, especially for oil exploration. Generating an explosion at the surface causes an impulsive acoustic wave to travel down into the earth. A proportion of the incident wave is reflected when a change in density occurs within the rocks. In general there will be many layers of different density within the rocks in the earth's crust resulting in a complicated response which can be measured at the surface. Ware and Aki [7] were the first to provide an algorithm for calculating the densities of the layers from this impulse response. Their method assumed no acoustic energy was lost to heat during propagation.

Applying the same technique to propagation in air means producing an air-

borne pulse, for instance using a loudspeaker or spark discharge. Reflections of sound within tubular acoustic structures then arise at changes of cross-sectional area. This was first suggested by Sondhi et al. as a way of determining the internal area profile of the mouth cavity [8, 9]. Experiments were performed on vocal tracts and lungs by Jackson et al. [10, 11]. A spark was used as a sound source, with the resulting pulse travelling along a section of cylindrical tubing called a source tube, then into the airway under test. The resulting reflections were measured by a microphone in the source tube wall. The reason for the source tube was to physically separate the in-going pulse signal from the impulse response. Measurements on human patients were performed by Fredberg et al. [12] and clinical use followed [13].

The first attempt at using pulse reflectometry on musical wind instruments was made by Benade and Smith [14]. While the lack of losses in the Ware-Aki algorithm posed no problem for the measurement of human airways, the longer length of many musical instruments means that losses play an important role in the impulse response and need to be included for an area profile algorithm to provide accurate results. Further work was performed by Smith [15]. Watson and Bowsher found that a reasonable reconstruction could be found by changing the dc offset in the experimental measurement untill the algorithm predicted the desired value of the bore radius at the open end [16]. This method of finding the bore is not always accurate since losses are not included explicitly. The effect of losses and dc offset are qualitatively similar meaning that the lack of losses may

be loosely compensated for by a false dc offset value. An alternative algorithm was developed by Amir et al. which incorporated viscothermal losses [17, 18]. This was used by Sharp et al. to provide accurate reconstructions of the internal profile of brass instruments [6, 19, 20].

While the main motivation for development of time domain measurement was to perform the calculation of the area profile from the measured response, the input impedance can also be deduced from the impulse response. The experiments presented in this thesis were performed using acoustic pulse reflectometry. Chapter 5 describes the existing setup for the measurement of musical wind instruments and we then go on to discuss practical improvements to the technique in chapter 7.

1.6 Calculation of the input impedance

As discussed in section 1.4, a plot of the input impedance of a wind instrument provides information on its resonance properties. Theoretical calculation of the input impedance is therefore useful for analysing the effect of a change to the bore of an instrument without having to build a new one each time. Also the theoretical study of sound propagation in instruments provides an insight into the way in which the instruments work.

1.6.1 Multimodal propagation

In chapter 2 we describe how the input impedance may be calculated theoretically using multimodal decomposition. We present the background to this technique here and go on to explain why it is useful for describing the behaviour of musical instruments in the introduction to chapter 2.

The problem of wave propagation in a uniform duct has a well known solution in the form of a sum of modes. While the lowest order mode has planar wavefronts, the higher order modes have non-uniform pressure distributions on a plane perpendicular to the direction of propagation. In a uniform pipe the modes propagate independently while at a change in cross-section the modes couple [21]. Each mode propagates with a different wavelength along the central axis for a given excitation frequency [22]. Furthermore, each mode (with the exception of the planar component) has a cut-off frequency below which the wavelength is imaginary and propagation is not possible. In general, the wave equation in an acoustic duct with a non-uniform cross-section is not solvable analytically, meaning we must resort to numerical methods.

A numerical calculation is often performed ignoring the effects of the higher order modes [23, 24]. The results are valid at low frequency because the higher order modes are non-propagating and at low rates of flare because the coupling between modes is minimised.

Higher order modes have been included in the theory of acoustic ducts by various authors. Individual discontinuities in tubes were probably first treated with higher modes included explicitly in papers by Miles [25, 26, 27]. The solution of the wave equation in ducts of varying cross-section was treated by Stevenson for acoustic horns [28] and for electromagnetic waves in conducting horns known as waveguides [29]. In electromagnetic theory there are 6 components of the electric and magnetic vector fields whereas the acoustic pressure is a scalar field. The theory of acoustic horns followed as a simplification of the electromagnetic theory, hence tubular objects in acoustics are refered to as acoustic waveguides. The equations provided by Stevenson cannot be solved explicitly, however. In order to determine the behaviour of a duct of varying circular cross-section, the internal profile must be approximated by a series of concentric cylinders as described by Alfredson [30]. The same may be done for horns of varying rectangular cross-section by using concentric oblongs.

Input impedances have been calculated by Oie et al [31] and in papers by Pagneux et al [32, 33] which form the basis for the theoretical work of chapter 2. Part of the procedure inevitably involves calculation of the radiation properties at the mouth of the horn.

If we assume that the highest frequency of interest is sufficiently low that only the plane mode may propagate in the duct, the radiation condition may be obtained from Levine and Schwinger [34] for a cylindrical pipe of zero wall

thickness or from Ando et al. [35, 36] for a cylindrical pipe of a certain wall thickness. We wish to keep the applicability of our method at high frequencies. There is no general expression currently available for the radiation condition without assuming that an infinite baffle is present around the opening of the horn. This radiation condition is due to Zorumski [37] for a cylindrical pipe and due to Kemp et al. [38] for a rectangular duct. Chapter 3 reviews the analysis of the radiation condition. The input impedance calculation method is then implemented in chapter 4.

In chapter 6 a multimodal method for calculating the reflections of a pressure wave from a tubular object is discussed. Initial work is shown for the case of a single discontinuity in two infinite tubes with acoustic pressure waves incident from only one side. This theory was initially formulated by Miles [25] in a summation notation and no calculations were presented. We will show how the situation may be easily represented in the matrix notation of Pagneux et al. [32] and calculations performed will show the response in both the frequency and time domains.

1.7 Aims and outline of thesis

The aims of this thesis are:

1. to study and develop the theory of multimodal propagation in acoustic

horns, in order to enable the influence of higher mode propagation to be assessed.

2. to describe acoustic pulse reflectometry as a means of measuring the properties of brass musical instruments, and to perform experiments to give examples of its use.

3. to develop acoustic pulse reflectometry to enable the measurement of longer instruments and to speed up the measurement process.

4. to discuss the possibility of including higher modes in the analysis of pulse reflectometry data.

Chapter 2 consists of a review of the theory of wave propagation in tubular objects first assuming plane wave propagation and then using multimodal expressions. This material is a review with amendments and corrections of the method of Pagneux et al. [32] for waveguides of circular cross-section and new work for objects of rectangular cross-section is also presented. A method for the calculation of the input impedance and pressure field is then derived.

In order to perform a multimodal calculation of the input impedance, the radiation impedance (the impedance at the open end of the horn) is needed as a starting point. Chapter 3 presents a numerical method for its calculation. The method for pipes of cylindrical cross-section is due to Zorumski [37] while the results for pipes of rectangular cross-section is due to the current author [39]. Chapter 4 brings chapters 2 and 3 together, giving an example calculation of the

input impedance and pressure field calculations for the bell section of a trumpet.

Chapter 5 is a review of acoustic pulse reflectometry. Experimental measurements of the input impulse response, the input impedance and the bore reconstruction are presented together with the analysis techniques.

In chapter 6 the multimodal reflection of sound from a single discontinuity between two infinite pipes is considered. The reflection is frequency dependent, with theoretical results presented showing the reflectance as a function of frequency and the time domain response. Analysis of pulse reflectometry experiments currently assumes plane wave propagation. A discussion of the possibility of incorporating multimodal propagation in the pulse reflectometry bore reconstruction algorithm then follows.

In chapter 7 we discuss and implement various improvements to pulse reflectometry. The first of these simply makes an existing process for removal of a dc offset in the measurement more accurate and convenient. Next we increase the length of instruments that may be measured by using post-processing to remove unwanted interference due to reflection of sound from the source. Finally we investigate the use of maximum length sequences, pseudo random signals resembling white noise, which are used to increase the signal to noise ratio in measurements.

Chapter 8, which concludes the thesis, gives an overview of the achievement of the aims and suggests ideas for future work.

Chapter 2

Multimodal propagation in acoustic horns

2.1 Introduction

Pressure disturbances in air-filled free space travel away from their source at a rate known as the speed of sound. The simplest mode of propagation of sound is in the form of plane waves where the wavefronts are flat two dimensional planes. The pressure variations can then be described entirely by a propagating sinusoidal pressure profile along the third spacial direction, perpendicular to the wavefront planes.

Most musical wind instruments consist of pipes of circular cross-section. In

fact many, such as the flute and the clarinet, feature an air column roughly cylindrical in shape. The acoustic waves set up within wind instruments have wavefronts perpendicular to the walls, meaning that the waves inside a cylindrical pipe are plane waves. Instruments whose bore is conical with a small enough apex angle object may also be assumed to contain plane waves in their air column. The air column can then be modelled by approximating the bore by a series of short concentric cylinders whose radius matches that of the instrument at each step along its length. If there are very many very short cylinders the bore of the cylinder series almost exactly matches the bore of the instrument. The plane waves in the cylindrical sections behave like plane waves in free space except that they are partially reflected and partially transmitted by any changes of cross-sectional area within the pipe.

For acoustic horns (such as the brass musical instruments) which feature rapidly flaring air columns, the wavefronts become more spherical in the bell section of the instrument in order to meet the wall at 90 degrees. A calculation of the properties of the instrument may still be made assuming plane wave propagation although the results will be far less accurate than for instruments without any flaring section. The basic theory of sound propagation in a musical wind instruments is set out in the literature mainly assuming plane wave propagation. To go beyond this, the actual pressure field can be expressed in terms of the sum of the plane waves present in the tube and the contribution from the modes of the duct whose pressure profile is not uniform on the plane perpendicular to

the central axis. This method is labelled modal decomposition or multimodal propagation.

This chapter comprises of a review of plane wave propagation in pipes of constant cross-section and at a discontinuous change in cross-section. The discussion then moves on to treat multimodal propagation. In order to describe fully the acoustic behaviour of an acoustic horn we must include the acoustic effect of radiation of sound from the open end. Chapter 3 will therefore treat this problem.

2.2 Plane waves in a uniform section of tube

Consider an infinite cylindrical pipe whose central axis we label z. We will begin by treating loss-less plane wave propagation in such a pipe. The pressure on any plane perpendicular to z is constant, so the pressure is simply a function of z and time, t. The wave equation is then ([40] p.107)

$$\frac{\partial^2}{\partial z^2} p = \frac{1}{c^2} \frac{\partial^2 p}{\partial t^2} \tag{2.1}$$

where $c \approx 343$ m/s is the speed of sound. The complex solution is

$$p(z,t) = \left(A e^{-ikz} + B e^{ikz} \right) e^{i\omega t} \tag{2.2}$$

where the real part of p is the physically observable pressure variation from the equilibrium atmospheric pressure value. A is the complex amplitude of the forward travelling pressure wave (in the positive direction along z) with the absolute value being the peak pressure in the forward wave and the real part defining the wave's phase by setting the value of the pressure at $z = 0, t = 0$. Similarly B is the complex pressure amplitude for the backward travelling wave. k is the wavenumber of the sinusoidal wave with the corresponding wavelength $\lambda = 2\pi/k$. ω is the angular frequency given by $\omega = 2\pi f$ where f is the frequency of the wave.

To verify that equation (2.2) is indeed a solution we can substitute into equation (2.1) giving

$$-k^2 p = -\frac{\omega^2}{c^2} p. \tag{2.3}$$

The equality holds because $c = \omega/k = f\lambda$.

These pressure changes are compression waves; they correspond to changes in the typical movements of gas molecules in the direction of propagation. The motion of the molecules in the air may be modelled by considering the motion of an "acoustic particle" large enough to contain millions of molecules but small enough that the acoustic variables are constant throughout its volume [40] p.99. To find the volume velocity from the pressure we use the linear inviscid force equation ([40] p.104):

$$\rho \frac{\partial v}{\partial t} = -\nabla p. \tag{2.4}$$

Here v is the acoustic particle velocity and ∇ is the gradient operator given by

$$\nabla p = \hat{x}\frac{\partial p}{\partial x} + \hat{y}\frac{\partial p}{\partial y} + \hat{z}\frac{\partial p}{\partial z} \tag{2.5}$$

where $\hat{x}$ is a unit vector along the x direction etc. For plane waves the pressure varies only along the z axis. The velocity is then a vector parallel to the z axis. Like the pressure, the velocity will be sinusoidal with time dependence $\exp(i\omega t)$. Substituting equation (2.2) into equation (2.4) gives the z component of the velocity as

$$v_z = \frac{1}{\rho\omega}\left(kAe^{-ikz} - kBe^{ikz}\right)e^{i\omega t}. \tag{2.6}$$

We will see when we come to consider ducts of varying cross-section, that it is useful to deal with a quantity called the volume velocity, defined as $U = v_z S$ where S is the cross-sectional area of the pipe. The volume velocity is then

$$U(z,t) = \frac{S}{\rho c}\left(Ae^{-ikz} - Be^{ikz}\right)e^{i\omega t}. \tag{2.7}$$

The acoustic impedance is then defined as being the ratio of the pressure and volume velocity. For forward travelling waves this is the characteristic impedance, $Z_c = \rho c/S$ and for backward travelling waves this is $-Z_c = -\rho c/S$ where $\rho = 1.21\mathrm{kg\,m^{-3}}$ is the equilibrium density of air. While the acoustic impedance of travelling plane waves is $\pm\rho c/S$, the acoustic impedance of the combination of forward and backward going waves must be calculated from the ratio of the

pressure and velocity resulting from both:

$$Z = \frac{p}{U} = \frac{\rho c}{S} \frac{Ae^{-ikz} + Be^{ikz}}{Ae^{-ikz} - Be^{ikz}}. \tag{2.8}$$

So far we have provided a formula for the volume velocity and impedance at any point in a duct of constant cross-section provided A and B (the complex amplitude of the forward and backward travelling pressure waves at $z = 0$) are known. Our eventual aim is to be able to work out the acoustic variables at one end of a series of concentric cylinders from the acoustic variables at the other end. The first step is to be able to project acoustic variables down a cylindrical section from an arbitrary z axis position. Consider the cylindrical pipe in figure 2.1. Two planes are defined: plane 1 is at $z = z_1$ and plane 0 is a distance d to the left of this. We want to know how to project the acoustic variables from plane 1 to plane 0.

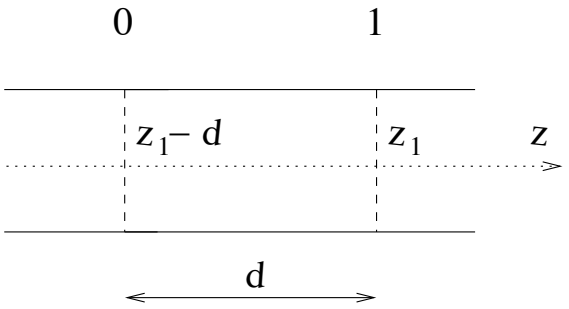

Figure 2.1: Uniform pipe

Labelling $p^{(0)}$ as the pressure on plane 0, by substituting the z coordinate of

$z = z_1 - d$ into (2.2) we get

$$\begin{aligned} p^{(0)} &= Ae^{-ik(z_1-d)} + Be^{ik(z_1-d)} \\ &= (Ae^{-ikz_1} + Be^{ikz_1})\cos(kd) + (Ae^{-ikz_1} - Be^{ikz_1})i\sin(kd). \end{aligned} \tag{2.9}$$

Now the pressure on plane 0 can be found from $p^{(1)}$ and $U^{(1)}$, the pressure and volume velocity on plane 1.

$$p^{(0)} = \cos(kd)p^{(1)} + i\sin(kd)Z_cU^{(1)} \tag{2.10}$$

where $Z_c = \rho c/S$. Similarly, for the volume velocity on plane 0, putting $z = z_1 - d$ into (2.7) gives:

$$U^{(0)} = i\sin(kd)Z_c^{-1}p^{(1)} + \cos(kd)U^{(1)} \tag{2.11}$$

The impedance, $Z^{(0)}$ on plane 0 can be obtained by dividing the pressure and volume velocity there:

$$Z^{(0)} = \frac{p^{(0)}}{U^{(0)}} = \frac{\cos(kd)p^{(1)} + i\sin(kd)Z_cU^{(1)}}{i\sin(kd)Z_c^{-1}p^{(1)} + \cos(kd)U^{(1)}} \tag{2.12}$$

Dividing through by $U^{(1)}$ gives $Z^{(0)}$ in terms of $Z^{(1)}$, the impedance on plane 1:

$$Z^{(0)} = \frac{p^{(0)}}{U^{(0)}} = \frac{\cos(kd)Z^{(1)} + i\sin(kd)Z_c}{i\sin(kd)Z_c^{-1}Z^{(1)} + \cos(kd)} \tag{2.13}$$

Notice that if a travelling wave is present at plane 1 in say the positive z direction

only we get $B = 0$ and $Z^{(1)} = Z_c$. Equation (2.13) then reduces to $Z^{(0)} = Z_c$ showing that the impedance is unchanged by projection along the cylinder. In general, however, the impedance will be changed by projection.

2.3 Plane waves at a change in cross-section

A wave experiences partial reflection and partial transmission at a change in impedance. Such a change occurs at a change in cross-sectional area since the characteristic impedance depends on S. Consider the discontinuous join between two cylinders shown in figure 2.2. We label as plane 1 the cross-section with area

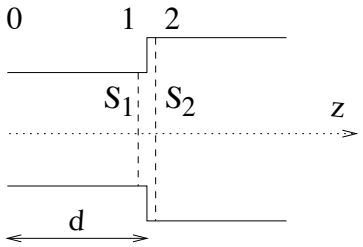

Figure 2.2: Detail of a waveguide consisting of straight sections of length d joined discontinuously

S_1 immediately to the left of the discontinuity. Plane 2 is defined to be the cross-section with area S_2 immediately to the right. The pressure and volume velocity on either side of a change of cross-section are equal, meaning that $p^{(1)} = p^{(2)}$ and $U^{(1)} = U^{(2)}$ in the current notation. It follows that the acoustic impedance is the same on each side of the discontinuity (ie. $Z^{(1)} = Z^{(2)}$).

It should not seem strange that the acoustic impedance is unaltered by the change in cross-section because the characteristic impedance $Z_c = \rho c/S$ has changed and the acoustic impedance has therefore altered relative to the characteristic impedance. We may use equation (2.13) to work out the impedance at plane 0 and the effect of the new cross-section will then have an effect on the resulting $Z^{(0)}$ value.

To further illustrate the point, we must deal with the forward and backward going waves in each cylinder. A and B are the complex pressure amplitudes for the waves in the cylinder to the left of discontinuity, meaning the pressure there from equation (2.2) is

$$p^{(1)} = \left(Ae^{-ikz} + Be^{ikz}\right) e^{i\omega t}. \tag{2.14}$$

C and D are the forward and backward going complex pressure amplitudes in the cylinder on the right of the discontinuity giving

$$p^{(2)} = \left(Ce^{-ikz} + De^{ikz}\right) e^{i\omega t}. \tag{2.15}$$

Using $p^{(1)} = p^{(2)}$ at the discontinuity (noting that planes 1 and 2 may be taken to be at the same z coordinate, just on opposite sides of the infinitely sharp discontinuity) gives

$$A + B = C + D. \tag{2.16}$$

From equation (2.7) the we volume velocity in plane 1 is

$$U^{(1)} = \frac{S_1}{\rho c}\left(Ae^{-ikz} - Be^{ikz}\right)e^{i\omega t} \tag{2.17}$$

and the volume velocity in plane 2 is

$$U^{(2)} = \frac{S_2}{\rho c}\left(Ce^{-ikz} - De^{ikz}\right)e^{i\omega t}. \tag{2.18}$$

Using the $U^{(1)} = U^{(2)}$ condition leads to

$$(A - B)S_1 = (C - D)S_2. \tag{2.19}$$

While the sum of the forward and backward waves is the same on either side of the discontinuity, the difference depends on the ratios of the cross-sections, hence the waves experience reflection and transmission coefficients.

In particular, consider if our pipes in figure 2.2 are infinite in length. A pressure wave is incident on the discontinuity from $-\infty$ with amplitude A. It is partially reflected with amplitude B back down the tube to $-\infty$ and partially transmitted to $+\infty$ with amplitude C. $D = 0$ since there is no backward going wave in S_2. We can solve (2.16) and (2.19) by eliminating C to get the reflection coefficient:

$$\frac{B}{A} = \frac{S_1/S_2 - 1}{S_1/S_2 + 1}. \tag{2.20}$$

A decrease in area means a positive reflection coefficient and an increase in area means a negative reflection coefficient while there is no reflection when $S_1 = S_2$. The transmission coefficient is obtained by eliminating B in the same equations:

$$\frac{C}{A} = \frac{2S_1/S_2}{S_1/S_2 + 1}. \tag{2.21}$$

To summarise, impedance is not effected by changes in cross-section and equation (2.13) describes how impedance changes when projected along a pipe of given cross-section. Now we have the equations necessary to work out the impedance at one end of a instrument of known internal profile provided the impedance at the other end is known. The impedance at the open end will depend on the geometry of the opening and is treated in detail in chapter 3. Projecting the impedance down to the input (mouthpiece) end gives us the input impedance, the amount of pressure produced in the mouthpiece by a unit volume velocity source. Now we have derived a method of input impedance calculation in the plane wave approximation, we will go on to do the same for multimodal propagation.

2.4 Multimodal equations in a uniform waveguide

The inclusion of higher modes in horn acoustics has been studied recently [32, 33, 38, 41, 42]. In general, the pressure and velocity in a cylinder can be expressed in terms of the modes of the duct whose amplitude patterns have n nodal circles and l nodal diameters on a circular cross-section where $(n, l) = (0, 0)$ is the plane wave mode. We are analysing axi-symmetric systems so we will treat axi-symmetric (nodal circle) modes only. The pressure and volume velocity are then vectors with a single subscript, n.

In the case of rectangular cross-section, the modes of the duct will have an integer number of nodal lines parallel to the y axis and an integer number of nodal lines parallel to the x axis. We will only treat systems that preserve symmetry about the central axis, so only modes with an even number of nodal lines in both dimensions need to be considered and the subscript $n = (n_x, n_y)$ will be used where there are $2n_x$ nodal lines parallel to the y axis and $2n_y$ nodal lines parallel to the x axis.

The pressure for each mode obeys the 3 dimensional wave equation:

$$\Delta p = \frac{1}{c^2}\frac{\partial^2 p}{\partial t^2}. \tag{2.22}$$

Here Δ is the Laplacian operator which may be expressed as the sum of the z direction component and the component on the x-y plane:

$$\Delta = \Delta_{\perp} + \frac{\partial^2}{\partial z^2} \tag{2.23}$$

where $\Delta_{\perp}$ is given in Cartesian coordinates as

$$\Delta_{\perp} = \left(\frac{\partial^2}{\partial x^2} + \frac{\partial^2}{\partial y^2} \right) \tag{2.24}$$

and in cylindrical polars as

$$\Delta_{\perp} = \left(\frac{\partial^2}{\partial r^2} + \frac{1}{r}\frac{\partial}{\partial r} + \frac{1}{r^2}\frac{\partial^2}{\partial \theta^2} \right). \tag{2.25}$$

The wave equation can be solved by expressing the pressure as a sum of the contributions of the modes of the duct where each term is the multiplication of the profiles along z, t and the x-y plane.

We can then solve the problem by separation of variables ([43] pp.540-556). From Pagneux et al. [32] the pressure and axial velocity are:

$$p(x, y, z, t) = \sum_{n=0}^{\infty} P_n(z)\psi_n(x, y)\exp(i\omega t), \tag{2.26}$$

$$v_z(x, y, z, t) = \frac{1}{S}\sum_{n=0}^{\infty} U_n(z)\psi_n(x, y)\exp(i\omega t), \tag{2.27}$$

where ψ_n is the pressure profile on the x-y plane and $P_n(z)$ is the pressure profile of the nth mode along the length of the tube. Similarly, $U_n(z)$ is the axial volume velocity profile of the nth mode along the length of the tube. $P_n(z)$ and $U_n(z)$ are in general complex numbers to take phase into account. Note that although it is convenient to refer to $U_n(z)$ as the volume velocity, the net volume velocity is U_0; the other entries are the amplitudes of the axial velocity distributions multiplied by the surface area but have no net contribution to the volume velocity [32].

Equation (2.26) gives the pressure as a series of terms, ψ_0 being unity, and so the $n = 0$ contribution represents plane wave propagation while the other modes have a non-uniform pressure profile. Substituting p from equation (2.26) into the wave equation (2.22) and dividing through by p gives:

$$\frac{1}{\psi_n}\Delta_\perp\psi_n + \frac{1}{P_n}\frac{\partial^2 P_n}{\partial z^2} = \frac{1}{\exp(i\omega t)}\frac{1}{c^2}\frac{\partial^2}{\partial t^2}\exp(i\omega t) \tag{2.28}$$

Since each term in this equation is a function of a different variable, each term must equal a constant. The differentiation with respect to t is straightforward giving

$$\frac{1}{c^2}\frac{\partial^2}{\partial t^2}\exp(i\omega t) = -k^2\exp(i\omega t) \tag{2.29}$$

with the eigenvalue $k = \omega/c$ being the free space wavenumber. Defining k_n to be

the wavenumber along z (commonly referred to as the propagation factor):

$$\frac{\partial^2}{\partial z^2} P_n(z) = -k_n^2 P_n(z). \tag{2.30}$$

The transverse term gives

$$\Delta_\perp \psi_n(x,y) = -\alpha_n^2 \psi_n(x,y) \tag{2.31}$$

with α_n being the eigenvalue of the nth mode. Physically α_n is the wavenumber in the x-y plane and is zero for plane wave propagation and is positive and real for the modes which feature nodal lines or circles.

It then follows from equation (2.28) that the wavenumbers follow the relation

$$k_n^2 = k^2 - \alpha_n^2. \tag{2.32}$$

The wavelength along z will be $\lambda_n = 2\pi/k_n$.

Note that in a pipe of uniform cross-section the solution of equation (2.30) gives

$$P_n(z) = A_n e^{-ik_n z} + B_n e^{ik_n z} \tag{2.33}$$

To find the corresponding volume velocities we use the force equation (2.4). The

z component of the velocity is

$$\rho \frac{\partial v_z}{\partial t} = -\frac{\partial p}{\partial z}. \tag{2.34}$$

giving the corresponding axial volume velocity as

$$U_n(z) = \frac{k_n S}{k\rho c}(A_n e^{-ik_n z} - B_n e^{ik_n z}). \tag{2.35}$$

We can note from this that the characteristic impedance, defined to be the ratio of pressure and volume velocity of forward travelling waves, also depends on the mode number, n. For plane waves it was $Z_c = \rho c/S$ but for the nth mode this becomes:

$$Z_c = \frac{k\rho c}{k_n S}. \tag{2.36}$$

Assuming loss-less propagation k_n is positive and real above cut-off point ($k_c = \alpha_n$) so the pressure varies sinusoidally along the z axis with a wavelength of $\lambda_n \geq \lambda$ where $\lambda = 2\pi/k$ is the free-space wavelength. Below the cut-off point k_n is negative and imaginary [42] so the pressure will be exponentially damped. Calculation of k_n first requires calculation of α_n which in turn depends on the boundary conditions in equation (2.31) (and therefore on the geometry of the duct). It will be treated for both lossy and non-lossy propagation in section 2.4.1 for ducts of circular cross-section and in section 2.4.2 for rectangular ducts.

We have seen that plane waves travelling across a section of tube are only reflected when the cross-section changes. The plane wave pressure amplitude at any point in a uniform section of tube may be obtained from a known plane wave pressure amplitude at a single point simply by projection using equation (2.10). Each of the other modes of the pipe will also only be reflected where the cross-section changes and so may be treated independently in a section of uniform cross-section. The wavenumber along the z axis becomes k_n for the nth mode and, as discussed earlier in the section, the characteristic impedance of the nth mode is $Z_c = \pm k\rho c/k_n S$. Projection of pressure and volume velocity complex amplitudes of the nth mode then follow from equations (2.10) and (2.11).

$$P_n^{(0)} = \cos(k_n d) P_n^{(1)} + i \sin(k_n d) \left(\frac{k\rho c}{k_n S} \right) U_n^{(1)}. \tag{2.37}$$

$$U_n^{(0)} = i \sin(k_n d) \left(\frac{k_n S}{k\rho c} \right) P_n^{(1)} + \cos(k_n d) U_n^{(1)}. \tag{2.38}$$

Here $P_n^{(0)}$ and $U_n^{(0)}$ are the complex amplitudes of the pressure and volume velocity of the nth mode on plane 0 and $P_n^{(1)}$ and $U_n^{(1)}$ are the complex amplitudes of the pressure and volume velocity of the nth mode on plane 1 with the planes separated by a distance d (see figure 2.1).

We define the pressure vector, $\mathbf{P}$, as a column vector consisting of the modal pressure amplitudes P_n and $\mathbf{U}$ as a column vector of the corresponding U_n values. A method of projecting the pressure and velocity vectors along a uniform section

of tube will now be discussed.

In matrix notation the pressure vector on plane 0 is given in terms of the vectors on plane 1 by

$$\mathbf{P}^{(0)} = D_1\mathbf{P}^{(1)} + D_2 Z_c \mathbf{U}^{(1)} \tag{2.39}$$

where D_1, D_2 and Z_c are diagonal matrices with the elements given by

$$D_1(n,m) = \begin{cases} \cos(k_n d) & : \quad n = m, \\ 0 & : \quad n \neq m, \end{cases} \tag{2.40}$$

$$D_2(n,m) = \begin{cases} i\sin(k_n d) & : \quad n = m, \\ 0 & : \quad n \neq m, \end{cases} \tag{2.41}$$

$$Z_c(n,m) = \begin{cases} k\rho c/k_n S & : \quad n = m, \\ 0 & : \quad n \neq m. \end{cases} \tag{2.42}$$

Similarly the volume velocity on plane 0 is given in terms of the vectors on plane 1 as

$$\mathbf{U}^{(0)} = D_2 Z_c^{-1}\mathbf{P}^{(1)} + D_1\mathbf{U}^{(1)}. \tag{2.43}$$

2.4.1 Solutions for a cylinder

In this section we will show the solutions of the wave equation for pipes of uniform cross-section. Consider a cylinder of radius R (cross-sectional area is $S = \pi R^2$)

as shown in figure 2.3. First we will examine the case of loss-less propagation

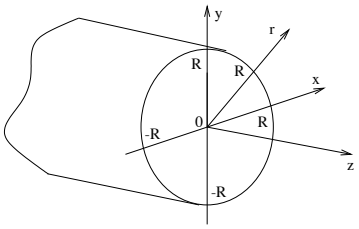

Figure 2.3: Cylindrical waveguide with radius R

along a duct of infinitely hard walls. No flow is allowed through the walls so the gradient of the pressure along the radial direction must equal zero at the wall. This boundary condition will be used to derive expressions for the mode profiles on the x-y plane, and the corresponding wavenumbers along the different dimensions. The modes in a uniform cylindrical duct will then be illustrated in a colour pressure map. We then go on to show the solutions for lossy propagation.

The profile of the various modes are the eigenfunctions defined in equation (2.31). In general, the solution need not be axially symmetric. Musical wind instruments are, however, generally designed so that the internal profile has no sharp sideways steps and only feature relatively gradual bends. This means that the behaviour may be modelled accurately by approximating the profile by a series of concentric cylinders. Only axially symmetric modes will have an effect on the response of an instrument assuming the excitation is also axi-symmetric. The present discussion will therefore be limited to axi-symmetric modes only. This approximation ignores the fact that the excitation from a brass instrument

player's lips is not perfectly axially symmetric.

Loss-less propagation

Assuming axi-symmetric pressure distributions only, equation (2.31) becomes:

$$\left(\frac{\partial^2}{\partial r^2} + \frac{1}{r}\frac{\partial}{\partial r}\right)\psi_n(r) = -\alpha_n^2\psi_n(r) \tag{2.44}$$

which can be manipulated into Bessel's equation of order zero [43] with the general solution ([43] p567)

$$\psi_n(r) = c_1 J_0(\alpha_n r) + c_2 Y_0(\alpha_n r) \tag{2.45}$$

where J_0 is Bessel function of the first kind of order zero and Y_0 is the Bessel function of the second kind of order zero. While Y_0 is singular at the origin, the pressure cannot have a singularity there. All the physically realisable solutions will therefore have $c_2 = 0$. The pressure on a cross-section on the x-y plane will therefore follow the shape of the Bessel function J_0. A three dimensional plot of J_0 is shown in figure 2.4 while figure 2.5 shows the function along the radial direction. It has a maximum at $r = 0$ and smoothly varies between positive and negative values. The rate at which this happens for $\psi_n = c_1 J_0(\alpha_n r)$ is determined by the x-y plane wavenumber, α_n. In order to work out the allowed values of α_n, we must consider the boundary conditions.

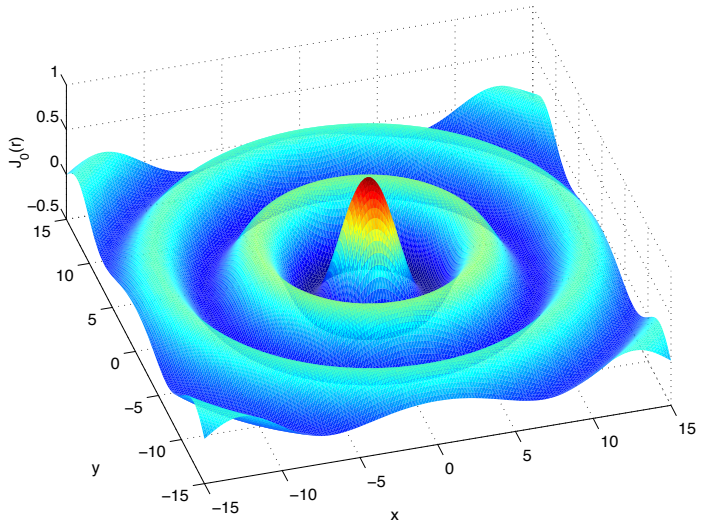

Figure 2.4: Three dimensional plot of the Bessel function of the first kind of order 0 against radius on the x-y plane

The boundary condition for loss-less propagation is

$$\frac{\partial \psi_n}{\partial r} = 0, \qquad r = R. \tag{2.46}$$

Using the orthogonality relation (as used by Kergomard [42])

$$\int_S \psi_n \psi_m dS = S\delta_{nm} \tag{2.47}$$

we get the solution

$$\psi_n = \frac{J_0(\gamma_n r/R)}{J_0(\gamma_n)} \tag{2.48}$$

where γ_n are the successive zeros of the derivative of the Bessel function of order

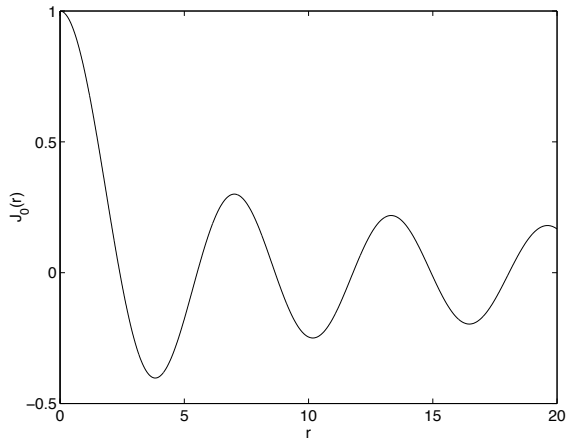

Figure 2.5: The Bessel function of the first kind of order 0

zero. From relation (A.3) in Appendix A we see that the derivative of J_0 is J_1. γ_n is therefore also equal to the zeros of the Bessel function of order one. These are tabulated for $n = 0$ to 45 in Appendix A. The corresponding values of α_n are then:

$$\alpha_n = \gamma_n / R. \tag{2.49}$$

Recalling equation (2.32) the z direction wavenumber is given in terms of the x-y plane wavenumber and the free space wavenumber as

$$k_n = \pm\sqrt{k^2 - \alpha_n}. \tag{2.50}$$

For $k > \alpha_n$ the square root is of a positive number and the positive sign should be taken in equation (2.50) so that k_n is a positive real wavenumber. For $k < \alpha_n$, however, the square root is of a negative number and the mode will have an

imaginary wavenumber in the z direction. Provided the negative sign is chosen in equation (2.50), the z direction pressure profile of that mode will then be

$$P_n(z) = A_n e^{-|k_n|z} + B_n e^{|k_n|z} \tag{2.51}$$

which shows exponential damping. The modes of a duct will therefore propagate provided the wavenumber (and therefore frequency) is above the cut-off frequency $k_c = \alpha_n = \gamma_n/R$ and will be exponentially damped otherwise. To summarise, the signs are chosen to be

$$k_n = \begin{cases} -\sqrt{k^2 - \left(\frac{\gamma_n}{R}\right)^2} & : \quad k < \frac{\gamma_n}{R}, \\ \sqrt{k^2 - \left(\frac{\gamma_n}{R}\right)^2} & : \quad k > \frac{\gamma_n}{R}. \end{cases} \tag{2.52}$$

Figure 2.6 displays a false colour image of the forward travelling modes in a cylinder (note one mode is in cut-off so is not really travelling). The horizontal axis runs parallel to the axis of the cylinder (z) while the vertical axis runs perpendicular to the axis of the cylinder such that the value 0 is the centre of the cylinder and -1 and 1 are the walls. To obtain the pressure distribution along the axis of the cylinder equation (2.52) was substituted into equation (2.33). This was multiplied by the transverse eigenfunction from equation (2.48) to give the full pressure field.

The real value of the complex pressure amplitude was chosen so that a snap-

shot of the pressure field is shown, rather than a time averaged value, as would be the case if the absolute value was shown. The relationship between the complex pressure amplitude and the time dependence of the pressure field will be discussed in more detail later, in section 2.7. Red indicates the pressure maximum and blue the pressure minimum in each graph.

Figure 2.6 shows plane wave propagation (n=0) for a wavenumber of $kR = \sqrt{50} \approx 7.071$. The n=1 mode with the same free space wavenumber is also shown. Notice that the pressure distribution follows the Bessel function profile across a line perpendicular to the cylinder axis. Since the modes we are considering are cylindrically symmetric the two nodal lines parallel to the z axis for n=1 become one nodal cylinder when this image is considered in 3 dimensions. The whole distribution varies sinusoidally along the z axis with the wavenumber k_n. Notice that $k_1 R = \sqrt{(kR)^2 - (\gamma_1)^2} = \sqrt{7.071^2 - 3.832^2} \approx 5.943$ so the z direction wavenumber has decreased and therefore the z direction wavelength has increased. This effect can be seen more clearly with the n=2 mode. The pressure distribution has two nodal cylinders and we can see that k_2 is approaching zero for this choice of free space wavenumber: $k_2 R = \sqrt{(kR)^2 - \gamma_2^2} = \sqrt{7.071^2 - 7.015^2} \approx 0.884$. The k value is below the cut-off point, $k = \gamma_n / R$ in the case of the n=3 mode. $k_3 R = -\sqrt{(kR)^2 - \gamma_3^2} = -\sqrt{7.071^2 - 10.173^2} \approx -7.314i$ meaning that the wave is exponentially damped or evanescent.

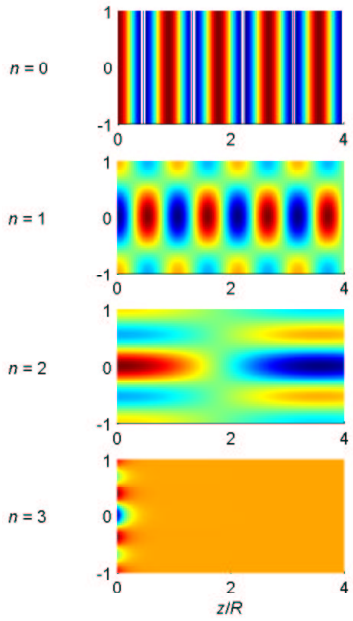

Figure 2.6: The modes in a cylindrical duct with $n = 0$ (plane wave mode), $n = 1$, $n = 2$ and $n = 3$ (evanescent). All have the same free space wavenumber

Lossy propagation

So far we have discussed the behaviour of acoustic waves in tubes assuming that none of the acoustic energy is lost to heat. In reality there is a boundary layer immediately beside the tube walls in which viscous and thermal losses occur. It is possible to use a lossy boundary condition to give lossy versions of ψ_n and α_n but the effect of losses will be noticeable in the z direction only because we will be considering objects which are significantly longer than they are wide. The inclusion or exclusion of the effect of losses will therefore be represented entirely by the choice of z direction wavenumber, k_n. Starting with a lossy boundary condition which allows a small acoustic particle velocity flow into the wall of the

tube, Bruneau et al [44] have produced a complex z direction wavenumber:

$$k_n = \pm\sqrt{k^2 - \left(\frac{\gamma_n}{R}\right)^2 + \left(\frac{2k}{R}\right)\left[\mathrm{Im}(\epsilon_n) - i\mathrm{Re}(\epsilon_n)\right]} \tag{2.53}$$

where ϵ_n is the boundary specific admittance at the wall. Admittance is the reciprocal of the impedance, so gives a measure of the acoustic velocity into the wall for a given acoustic pressure. The implication is not that there is really a flow into the walls (which are rigid in reality) but that the loss of energy at the boundary layer is simulated by imagining that such a flow exists. The boundary specific admittance is given by [44]:

$$\epsilon_n = \left(1 - \gamma_n^2/(k^2R^2)\right)\epsilon_v + \epsilon_t \tag{2.54}$$

with $\epsilon_v = (1+i)\ 2.03 \times 10^{-5} f^{1/2}$ and $\epsilon_t = (1+i)\ 0.95 \times 10^{-5} f^{1/2}$ under standard conditions. The full expressions for ϵ_v and ϵ_t in terms of the thermodynamic constants of air are given in [44].

The choice of signs is complicated by the fact that we are performing the square root operation on a complex number. To split k_n into real and imaginary parts, it is helpful to first express (2.53) as follows

$$k_n = \pm\sqrt{A_n + I_n - iR_n} \tag{2.55}$$

where A_n is the square of k_n in the absence of losses:

$$A_n = k^2 - \left(\frac{\gamma_n}{R}\right)^2, \tag{2.56}$$

R_n gives the imaginary part of the correction in k_n^2:

$$R_n = (2k/R)\mathrm{Re}(\epsilon_n), \tag{2.57}$$

and I_n is the real part of the correction in k_n^2:

$$I_n = (2k/R)\mathrm{Im}(\epsilon_n). \tag{2.58}$$

Now we can express k_n in terms of real and imaginary parts:

$$k_n = \chi_n + i\kappa_n. \tag{2.59}$$

Equating equations (2.55) and (2.59) we get

$$\chi_n^2 - \kappa_n^2 + 2i\chi_n\kappa_n = A_n + I_n - iR_n \tag{2.60}$$

which can be solved by simultaneous equations for the real and imaginary parts giving [44]

$$\chi_n = \frac{1}{\sqrt{2}}\sqrt{\left\{A_n + I_n + \sqrt{(A_n + I_n)^2 + R_n^2}\right\}} \tag{2.61}$$

and

$$\kappa_n = -\frac{1}{\sqrt{2}}\sqrt{\left\{-(A_n + I_n) + \sqrt{(A_n + I_n)^2 + R_n^2}\right\}}. \tag{2.62}$$

Putting $n = 0$ this equation gives the imaginary part of the plane mode wavenumber as $-2.98 \times 10^{-5} f^{1/2}/R$.

2.4.2 Solutions for a uniform rectangular duct

Consider a duct with rectangular cross-section with halfwidths a and b (cross-sectional area is $S = 4ab$) as shown in figure 2.7. The multimodal treatment

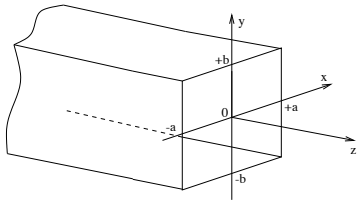

Figure 2.7: Rectangular waveguide with halfwidths a and b

discussed for cylindrical geometry was due to Pagneux et al [32]. A geometry was also discussed in [32] in which the walls are flat and parallel. The z axis went along the pipe axis, the pipe had a finite width in the y direction and was infinite in width along x. What follows is new work using the same method which formulates the problem of multimodal propagation in rectangular guides which are finite in both the x and y directions.

Loss-less propagation

The boundary condition for the eigenfunction of the nth higher mode defined in equation (2.31) is:

$$\frac{\partial \psi_n}{\partial x} = 0, \qquad x = -a, a \tag{2.63}$$

$$\frac{\partial \psi_n}{\partial y} = 0, \qquad y = -b, b \tag{2.64}$$

The solution is most conveniently expressed by separating it into the x dependent and y dependent parts:

$$\psi_n = \phi_{n_x} \sigma_{n_y} \tag{2.65}$$

where

$$\phi_{n_x} = \begin{cases} 1 & : \quad n_x = 0, \\ \sqrt{2}\cos(n_x \pi x/a) & : \quad n_x > 0. \end{cases} \tag{2.66}$$

$$\sigma_{n_y} = \begin{cases} 1 & : \quad n_y = 0, \\ \sqrt{2}\cos(n_y \pi y/b) & : \quad n_y > 0. \end{cases} \tag{2.67}$$

Performing the differentiation from equation (2.31) gives the corresponding eigenvalues as

$$\alpha_n = \sqrt{\left(\frac{n_x \pi}{a}\right)^2 + \left(\frac{n_y \pi}{b}\right)^2}. \tag{2.68}$$

As with circular cross-section it is possible to use a lossy boundary condition to give lossy versions of ψ and α but the effect of losses will be noticeable in the z direction only and will therefore be represented entirely by the choice of z

direction wavenumber, k_n.

$$k_n = \begin{cases} -\sqrt{k^2 - (n_x\pi/a)^2 - (n_y\pi/b)^2} & : \quad k^2 < (n_x\pi/a)^2 + (n_y\pi/b)^2\,, \\ \sqrt{k^2 - (n_x\pi/a)^2 - (n_y\pi/b)^2} & : \quad k^2 > (n_x\pi/a)^2 + (n_y\pi/b)^2\,. \end{cases} \tag{2.69}$$

Lossy propagation

Lossy propagation may be represented as with circular cross-section by working out the lossy z direction wavenumber, (Bruneau et al [44]). Starting from the lossy boundary condition gives k_n as

$$k_n = \pm\sqrt{A_n + I_n - iR_n} \tag{2.70}$$

where A_ν is the square of the non-lossy version of k_n which in rectangular geometry is

$$A_\nu = k^2 - \left(\frac{n_x\pi}{a}\right)^2 - \left(\frac{n_y\pi}{b}\right)^2. \tag{2.71}$$

The real part of the correction to k_n^2 is [44]

$$I_\nu = 2k\left((2-\delta_{n_x,0})\frac{\mathrm{Re}(\epsilon_x)}{a} + (2-\delta_{n_y,0})\frac{\mathrm{Re}(\epsilon_y)}{b}\right) \tag{2.72}$$

where the boundary specific admittances are

$$\epsilon_x = \left(1 - \left(\frac{n_x\pi}{ka}\right)^2\right)\epsilon_v + \epsilon_t \tag{2.73}$$

$$\epsilon_y = \left(1 - \left(\frac{n_y \pi}{kb}\right)^2\right) \epsilon_v + \epsilon_t \tag{2.74}$$

with $\epsilon_v = (1+i)\ 2.03 \times 10^{-5} f^{1/2}$ and $\epsilon_t = (1+i)\ 0.95 \times 10^{-5} f^{1/2}$. The imaginary part of the correction to k_n^2 is [44]

$$R_\nu = 2k \left((2 - \delta_{n_x,0}) \frac{\mathrm{Im}(\epsilon_x)}{a} + (2 - \delta_{n_y,0}) \frac{\mathrm{Im}(\epsilon_y)}{b} \right). \tag{2.75}$$

Using the same method as for cylindrical geometry, k_n is the sum of real and imaginary parts

$$k_n = \chi_n + i\kappa_n \tag{2.76}$$

where χ_n and κ_n are given by

$$\chi_n = \frac{1}{\sqrt{2}} \sqrt{\left\{ A_n + I_n + \sqrt{(A_n + I_n)^2 + R_n^2} \right\}} \tag{2.77}$$

and

$$\kappa_n = -\frac{1}{\sqrt{2}} \sqrt{\left\{ -(A_n + I_n) + \sqrt{(A_n + I_n)^2 + R_n^2} \right\}}. \tag{2.78}$$

2.5 Multimodal equations at a discontinuity

So far we have provided the equations describing the behaviour of the modes of uniform ducts with circular and rectangular cross-section. As mentioned before, the aim of this chapter is to enable the calculation of acoustic variables in a duct

of varying cross-section. The method employed here is to discretise the smoothly varying duct into a large number of concentric cylinders (or rectangles). While we have already seen equations which describe propagation within each cylinder, we still need to analyse how the modes of the duct are effected by changes of cross-section. This section deals with this problem.

Consider again the typical discontinuous join between two sections of tube of differing cross-section shown in figure 2.2. The pressure field at either side of the discontinuity must be equal on the section of air they share. However, the nth mode on S_1 will not match the nth mode on S_2 because the cross-sections are different. This means that when the nth mode is incident on the discontinuity, the pressure on the other side must consist of the sum of the contributions of many modes. We say that the wave experiences mode conversion at the discontinuity.

Now this will be put into our mathematical framework. We recall $\mathbf{P}^{(1)}$ is the vector of modal pressure amplitudes on the surface S_1 and define $\mathbf{P}^{(2)}$ as the vector of modal pressure amplitudes on the surface S_2. In circular cross-section, when $R_2 > R_1$, $\mathbf{P}^{(1)}$ can be found from $\mathbf{P}^{(2)}$ by projection. This procedure can also be performed in rectangular geometry when $a_2 > a_1$ and $b_2 > b_1$.

The following expression relating the pressure vectors on either side of the discontinuity is derived in appendix B using the orthogonality of Bessel functions:

$$\mathbf{P}^{(1)} = F\mathbf{P}^{(2)}, \qquad S_1 < S_2 \tag{2.79}$$

where F is a matrix with the elements defined by

$$F_{nm} = \frac{1}{S_1} \int_{S_1} \psi_n^{(1)} \psi_m^{(2)} dS. \tag{2.80}$$

When $R_1 > R_2$ or $a_1 > a_2$ and $b_1 > b_2$, the pressure must be equated on the smaller S_2 surface. This means that the equations look the same but with the labels 1 and 2 interchanged:

$$\mathbf{P}^{(2)} = V\mathbf{P}^{(1)}, \qquad S_1 > S_2 \tag{2.81}$$

where V is a matrix with the elements defined by

$$V_{nm} = \frac{1}{S_2} \int_{S_2} \psi_n^{(2)} \psi_m^{(1)} dS. \tag{2.82}$$

The integration in equation (2.80) will be performed analytically to get the elements of the matrix F. The expression for the elements of the matrix V will follow from the derivation by symmetry. Note that to avoid unnecessary complication we will not treat rectangular ducts which contract along the x direction while at the same time expanding along the y direction or vice versa.

The vector $\mathbf{U}$ can be projected by equating the axial velocity on the air shared by S_1 and S_2. Also the axial velocity is required to be zero into the wall surface perpendicular to the z axis which results from S_1 not equalling S_2. For $S_1 < S_2$ the axial velocity on either side is therefore matched on S_1 and set to zero on the

part of S_2 which is not in contact with S_1. The calculation is performed in detail in appendix B to give

$$\mathbf{U}^{(2)} = F^{\mathrm{T}}\mathbf{U}^{(1)}, \qquad S_1 < S_2 \tag{2.83}$$

where F^{T} is the transpose of F. For $S_1 > S_2$ the axial velocity is therefore equated over S_2 and set to zero on the part of S_1 not in contact with S_2.

$$\mathbf{U}^{(1)} = V^{\mathrm{T}}\mathbf{U}^{(2)}, \qquad S_1 > S_2. \tag{2.84}$$

2.5.1 Solutions for circular cross-section

The matrices F and V defined in (2.80) can be found analytically for circular cross-section using the standard integral in equation (A.1) of appendix A. A full derivation is given in appendix B. The result is that each element is a function of $\beta = R_1/R_2$ and the element (n, m) is given by

$$F_{nm}(\beta) = \frac{2\beta\gamma_m J_1(\beta\gamma_m)}{(\beta^2\gamma_m^2 - \gamma_n^2)J_0(\gamma_m)} \tag{2.85}$$

where $\beta = R_1/R_2$ and $F(0,0) = 1$ and

$$V_{nm}(\beta) = F_{nm}(1/\beta) \tag{2.86}$$

When the change in cross-section tends to zero (ie. β tends to 1) we obtain

$$F \approx I - \epsilon Q \tag{2.87}$$

with I being the identity matrix (a diagonal matrix with all the entries having a value of 1). ϵ is the fractional change in cross-section, $\epsilon = (S_2 - S_1)/S_1$ and Q is a matrix whose elements are given by

$$Q_{nm} = \begin{cases} 0 & : \quad n = m, \\ \frac{\gamma_m^2}{\gamma_m^2 - \gamma_n^2} & : \quad \text{otherwise.} \end{cases} \tag{2.88}$$

2.5.2 Solutions for rectangular cross-section

The F matrix defined in (2.80) may be presented most conveniently in rectangular coordinates by expressing each entry as the multiplication of two terms:

$$\begin{aligned} F_{nm}(\beta_x, \beta_y) &= \frac{1}{S_1} \int_{S_1} \psi_n^{(1)} \psi_m^{(2)} dS \\ &= \frac{1}{2a_1} \int_{-a_1}^{a_1} dx \phi_{n_x}^{(1)} \phi_{m_x}^{(2)} \frac{1}{2b_1} \int_{-b_1}^{b_1} dy \sigma_{n_y}^{(1)} \sigma_{m_y}^{(2)} \\ &= X_{n_x m_x} Y_{n_y m_y} \end{aligned} \tag{2.89}$$

$$X_{n_x m_x}(\beta_x) = \begin{cases} 1 & : \quad n_x = m_x = 0, \\ \sqrt{2}\text{sinc}(m_x \pi \beta_x) & : \quad n_x = 0, m_x > 0, \\ 2\text{sinc}(\pi(m_x \beta_x - n_x)) \frac{m_x \beta_x}{m_x \beta_x + n_x} & : \quad n_x > 0. \end{cases} \tag{2.90}$$

$$Y_{n_y m_y}(\beta_y) = \begin{cases} 1 & : \quad n_y = m_y = 0, \\ \sqrt{2}\text{sinc}(m_y \pi \beta_y) & : \quad n_y = 0, m_y > 0, \\ 2\text{sinc}(\pi(m_y\beta_y - n_y))\frac{m_y\beta_y}{m_y\beta_y + n_y} & : \quad n_y > 0. \end{cases} \tag{2.91}$$

where $\beta_x = \frac{a_1}{a_2}$ and $\beta_y = \frac{b_1}{b_2}$. When both β_x and β_y tend to 1 we get

$$X_{n_x m_x}(\beta_x) \approx \begin{cases} 1 & : \quad n_x = m_x = 0, \\ 1 - \frac{1}{2}\epsilon_x & : \quad n_x = m_x \neq 0, \\ \sqrt{2}(-1)^{m_x}(-\epsilon_x) & : \quad n_x \neq m_x, n_x = 0, \\ 2(-1)^{m_x + n_x}(-\epsilon_x)\frac{m_x^2}{m_x^2 - n_x^2} & : \quad n_x \neq m_x, n_x > 0. \end{cases} \tag{2.92}$$

$$Y_{n_y m_y}(\beta_y) \approx \begin{cases} 1 & : \quad n_y = m_y = 0, \\ 1 - \frac{1}{2}\epsilon_y & : \quad n_y = m_y > 0, \\ \sqrt{2}(-1)^{m_y}(-\epsilon_y) & : \quad n_y \neq m_y, n_y = 0, \\ 2(-1)^{m_y + n_y}(-\epsilon_y)\frac{m_y^2}{m_y^2 - n_y^2} & : \quad n_y \neq m_y, n_y > 0. \end{cases} \tag{2.93}$$

where $\epsilon_x = (a_2 - a_1)/a_1$ and $\epsilon_y = (b_2 - b_1)/b_1$. The V matrix will have entries given by

$$V_{nm} = F_{nm}(1/\beta_x, 1/\beta_y). \tag{2.94}$$

2.6 Method for calculation of input impedance

We have presented the equations for the pressure and axial velocity in a duct in terms of the unknowns $P_n(z)$ and $U_n(z)$. Now we define the left hand side

(negative z side) of a waveguide of arbitrary cross-section as the input end and the right hand side (positive z side) as the output end. The waveguide is then approximated by a series of uniform sections as shown in figure 2.8 (cylinders in circular geometry and rectangular sections in rectangular geometry).

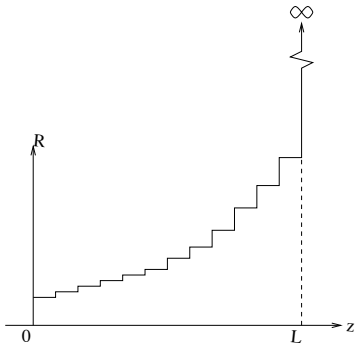

Figure 2.8: Horn approximated by a series of cylinders

In plane wave acoustics the impedance is defined as the ratio of the acoustic pressure and volume velocity. For the multimodal case we define the acoustic impedance matrix, Z, as follows:

$$\mathbf{P} = Z\mathbf{U} \tag{2.95}$$

so that

$$P_n = \sum_{m=0}^{\infty} Z_{nm} U_m \tag{2.96}$$

and therefore Z_{nm} is the factor of contribution to the pressure amplitude of the nth mode due to the volume velocity amplitude of the mth mode. The vectors

and matrices are infinite but must be truncated before numerical implementation.

2.6.1 Projection across a discontinuity

Using equations (2.79) and (2.83) we can show that the impedance matrix on surface 1 can be found from the impedance matrix on surface 2 at an expansion as follows:

$$Z^{(1)} = F Z^{(2)} F^{\mathrm{T}}, \qquad S_1 < S_2. \tag{2.97}$$

The equivalent at at a contraction of the bore follows from equations (2.81) and (2.84):

$$Z^{(1)} = V^{-1} Z^{(2)} (V^{\mathrm{T}})^{-1}, \qquad S_1 > S_2. \tag{2.98}$$

2.6.2 Projection along a cylinder

Substituting (2.39) and (2.43) into (2.95) gives an equation for the impedance at the left hand side of a uniform section of duct in terms of the impedance at the right hand side, being the multimodal version of equation (2.13):

$$Z^{(0)} = (D_1 Z^{(1)} + D_2 Z_c)(D_2 Z_c^{-1} Z^{(1)} + D_1)^{-1}. \tag{2.99}$$

Now if we simplify by multiplying top and bottom by D_1^{-1},

(N.B. This is a correction to the original version of my thesis)

$$Z^{(0)} = \left(iD_3\right)^{-1} Z_c - D_2^{-1} Z_c \left(Z^{(1)} + \left(iD_3\right)^{-1} Z_c\right)^{-1} D_2^{-1} Z_c \tag{2.100}$$

Here

$$D_3(n,m) = \begin{cases} \tan(k_n d) & : \quad n = m, \\ 0 & : \quad n \neq m. \end{cases} \tag{2.101}$$

The input impedance matrix may then be calculated from the output end impedance matrix by projecting alternately along a cylinder using equation (2.100) and across a discontinuity using equation (2.97) until the input end is reached.

Typically the acoustic horns that we will consider are cylindrical at the input end and only flare out towards the open end. The radiation impedance matrix at an open end is the subject of the next chapter. A waveguide terminated in an infinite cylindrical pipe is also a useful subject of theoretical study. In such an infinite terminating pipe all waves are forward going and the impedance is simply given by the characteristic impedance matrix of equation (2.42).

2.7 Method for calculation of pressure field

If we set $U_0 = 1$ and $U_n = 0$ for $n > 0$ at the mouth of the horn, we have a plane velocity at the input end of the horn. Physically this corresponds to driving the input with a rigid piston. Using stored values of the impedance along the guide

we can project the volume velocity vector forward to the end of the guide using the following equations:

$$\mathbf{U}^{(1)} = (-D_2 Z_c^{-1}(Z^{(0)} - Z_c) + E)\mathbf{U}^{(0)} \tag{2.102}$$

where D_2 is a diagonal matrix with the nth diagonal given by $i\sin(k_n d)$ and E is a diagonal matrix with the nth diagonal given by $e^{-ik_n d}$.

$$\mathbf{U}^{(2)} = F^{\mathrm{T}}\mathbf{U}^{(1)}. \tag{2.103}$$

The pressure vector at each point along the horn is then given by $\mathbf{P} = Z\mathbf{U}$.

The entries in the vector give the complex amplitude of each mode. Consider the time dependence of the plane wave component of the pressure at the input, having a complex amplitude $A + iB$:

$$p_0(t) = (A + iB)\exp i\omega t. \tag{2.104}$$

This will have a maximum amplitude of $\sqrt{A^2 + B^2}$ and vary sinusoidally in time:

$$p_0(t) = \sqrt{A^2 + B^2}e^{i(\omega t - \phi_0)} \tag{2.105}$$

where ϕ_0 is the angle of the pressure on the complex plane at $t = 0$:

$$\phi_0 = \angle(A + iB) = \begin{cases} \arctan(B/A) & : \quad A \geq 0, \\ \pi + \arctan(B/A) & : \quad A < 0. \end{cases} \tag{2.106}$$

Since the plane wave term in the volume velocity vector was chosen to be real at the input end, the volume velocity is at its maximum at $t = 0$ and the phase angle ϕ_0 for the plane component of the pressure vector at the input gives the phase angle by which the pressure leads the volume velocity. We will choose to plot the pressure field when the pressure at the input is at its maximum. From equation (2.105) we see that this occurs at time $t = -\phi_0/\omega$.

Now consider the pressure at some point along the length of the duct where the complex pressure amplitude of the nth mode is $C_n + iD_n$:

$$p(x, y, z, t) = \sum_{n=0}^{\infty} (C_n(z) + iD_n(z))\psi_n(x, y) \exp i\omega t. \tag{2.107}$$

Putting $t = -\phi_0/\omega$ and taking the real part gives the physically observable pressure field when the plane pressure is maximum at the input:

$$p(x, y, z, -\phi_0/\omega) = \sum_{n=0}^{\infty} (C_n(z)\cos\phi_0 + D_n(z)\sin\phi_0)\,\psi_n(x, y). \tag{2.108}$$

Figure 2.9 shows the pressure field calculated in this manner for a cylinder of length 5mm and radius $R_1 = 10$mm driven by a piston vibrating sinusoidally at 10

kHz connected to a cylinder of radius $R_2 = 15$mm assuming lossy propagation. 25 modes were used and the system was approximated by 1000 cylinders for the calculation. The termination on the right is the infinite cylindrical pipe termination $Z_c = \rho c/S$ where $S = \pi R_2^2$. Here red indicates the maximum value of the real part of the pressure and blue the minimum.

Notice that the wavefronts expand out from the opening. The contours of equal pressure are perpendicular to the walls as required by the hard walled boundary condition. The pressure is continuous at the discontinuity showing that the algorithm correctly projects the modes across.

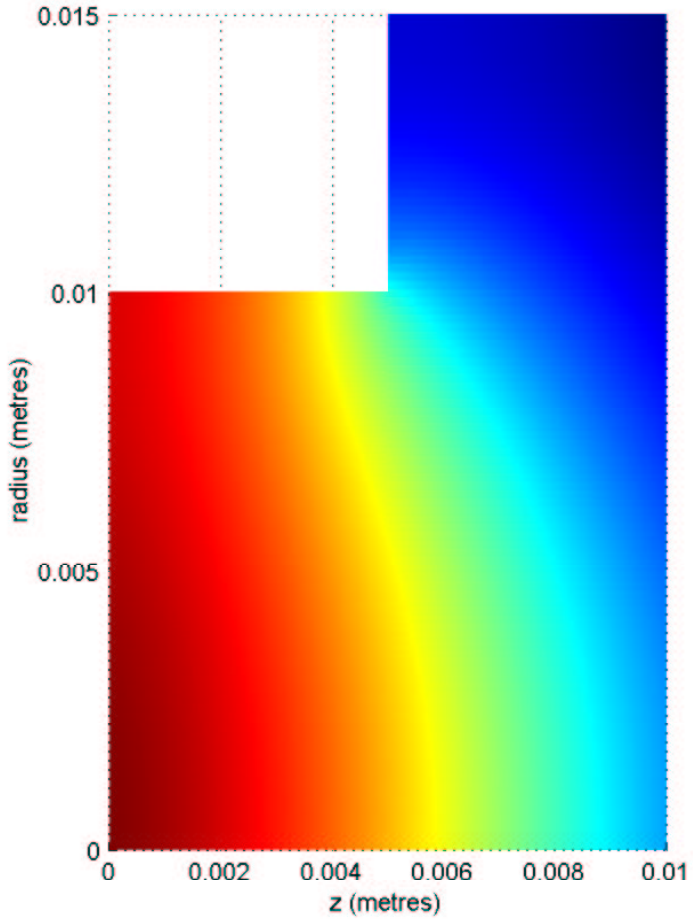

Figure 2.9: Pressure field of a piston driven cylinder terminated in an infinite cylindrical pipe

Chapter 3

Radiation impedance

3.1 Introduction

In chapter 2 a method was presented for calculating the impedance at any point along an acoustic horn from the impedance at any other part of the horn. For this to be useful we must get a starting point. In practice we are dealing with horns with a narrow input end and a wide flaring bell which radiates some of the sound into free space. While the input impedance will depend on the whole of the horn we are dealing with, the radiation impedance only depends on the geometry of the opening into free space and serves as our boundary condition.

Various methods of analysing the behaviour of the open end of a duct are discussed. As mentioned previously, in a pipe of constant cross-section, the higher

order modes propagate independently, while at a change of cross-section there exists mode coupling. If the rate of flare of an acoustic horn is large, the coupling of modes has a significant effect on the musical performance of the horn. An expression for the radiation impedance at an open end should therefore include mode coupling. In order to achieve a multimodal expression for the radiation impedance, it is currently necessary to assume the duct is terminated in an infinite baffle. Obviously, practical examples will not feature an infinite baffle at the opening and a small error in the input impedance calculation results. Numerical evaluation of the multimodal radiation impedance is performed by reference to Zorumski [37] for a cylindrical duct and to the current author, Kemp et al. [39], for a rectangular duct.

3.2 Ideal open end condition

A first approximation to the behaviour at the end of a duct may be obtained using the plane wave approximation. Recalling equation (2.20), the plane wave approximation reflection coefficient at a change in cross-section from S_1 to S_2 is given by:

$$\frac{B}{A} = \frac{S_1/S_2 - 1}{S_1/S_2 + 1}. \tag{3.1}$$

An open end corresponds to S_2 tending to infinity, so B/A tends to -1. The acoustic wave is reflected back down the duct 180^o out of phase implying standing

waves with zero pressure amplitude at the open end as mentioned in chapter 1. While this is useful for obtaining a first approximation for the behaviour of musical instruments it is obvious that, even ignoring mode conversion at the opening for the moment, a more accurate analysis of the end condition should account for the sound radiated from the end of the instrument.

3.3 The piston approximation

Going beyond the ideal open end condition, we may assume that only plane waves propagate in the duct but that a non-zero pressure arises at the end due to the radiation of sound from the end. This is called the piston approximation. In the low frequency limit, the result is that the pressure node is moved a fraction of a tube radius down the axis of the duct from the actual tube end. This is known as length correction and is discussed in pp.180-181 of Fletcher and Rossing [45]. The full expression for the piston approximation radiation impedance is available for an unflanged cylindrical duct due to Levine and Schwinger [34] and in the case of a flanged cylindrical duct due to Rayleigh [46]. Both are graphed in Fletcher and Rossing [45] pp.181-182. In rectangular geometry the radiation impedance of a rectangular piston (which is the equivalent to the impedance for the plane velocity and plane pressure modes in a rectangular duct) mounted in an infinite baffle has been treated [47, 48, 49, 50, 51].

3.3.1 Pressure radiation from a piston terminated in an infinite baffle

Consider a rigid piston in a rigid infinite baffle as shown in figure 3.1. The piston vibrates uniformly with a sinusoidal velocity of amplitude v normal to the baffle. In order to calculate the behaviour of this system, we split the piston into in-

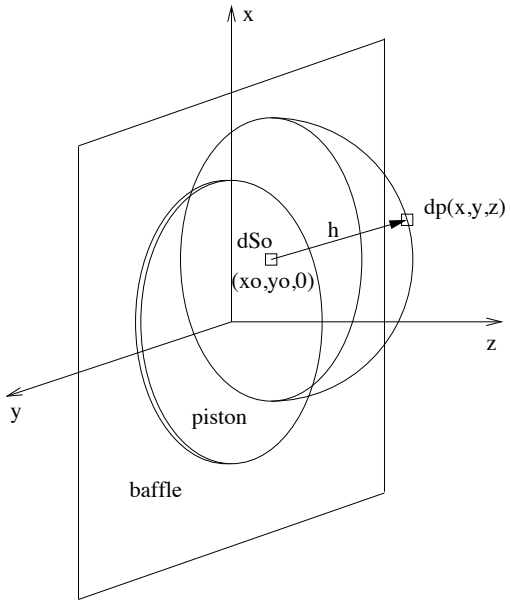

Figure 3.1: Piston in an infinite baffle

finitesimal simple source elements and sum the resulting pressure fields. A piston surface element of area dS_0 is present at $(x_0, y_0, 0)$. This surface element oscillates with a velocity amplitude of v normal to the baffle and acts as a simple source of spherical pressure waves. These are represented on the diagram by a hemispherical shell, with the acoustic pressure at a distance $h = \sqrt{(x-x_0)^2 + (y-y_0)^2 + z^2}$

from the source element given by [40]

$$dp(x,y,z) = i\omega\rho\frac{Q}{2\pi}\frac{e^{-ikh}}{h}, \tag{3.2}$$

where $Q = vdS_0$ is the simple source strength and a $e^{i\omega t}$ time factor is assumed throughout. The part e^{-ikh}/h is known as the Green's function and implies that the pressure oscillates sinusoidally in space with wavelength $\lambda = 2\pi/k$ and with an amplitude that dies as $1/h$. Integrating (3.2) over S, the surface of the whole piston, we get the total pressure field due to the sum of all the source elements that make up the piston.

$$p(x,y,z) = i\omega\rho\frac{v}{2\pi}\int_S dS_0\frac{e^{-ikh}}{h}. \tag{3.3}$$

Note that the integrand is singular (tends to infinity) as h tends to zero. This problem must be addressed before numerical integration is possible.

3.4 Pressure radiation from a duct terminated in an infinite baffle

An expression has been derived for the pressure field due to a rigid piston with a velocity amplitude of v on the surface of a baffle. Consider a uniform duct terminated in an infinite baffle. The plane wave mode will have a velocity source

identical to that of the piston. Recalling equation (2.27), the axial velocity due to the mth mode is given by the modal velocity amplitude U_m/S multiplied by that mode's transverse velocity profile $\psi_m(x_0, y_0)$. Replacing the piston velocity source in (3.3) with this velocity distribution gives the total pressure field assuming only the mth mode is present to provide a velocity source on the surface S.

$$p(x,y,z) = \frac{i\omega\rho}{2\pi S}\int_S dS_0 U_m \psi_m(x_0,y_0)\frac{e^{-ikh}}{h}. \tag{3.4}$$

In general, the total pressure field will be the sum of the contribution by all the modes:

$$p(x,y,z) = \sum_{m=0}^{\infty}\frac{i\omega\rho}{2\pi S}\int_S dS_0 U_m \psi_m(x_0,y_0)\frac{e^{-ikh}}{h}. \tag{3.5}$$

3.5 Multimodal radiation impedance of a duct terminated in an infinite baffle

In chapter 2 we defined the acoustic impedance in a duct as the ratio of the pressure amplitude to the volume velocity amplitude. We therefore wish to define the radiation impedance as the ratio of the pressure amplitude and the volume velocity amplitude on the radiating surface. An expression has been derived for the total pressure field in terms of the volume velocity amplitude. The next step is therefore to calculate the pressure amplitude of a particular mode at $z = 0$

from the total pressure field. To do this we first express the pressure field there as the sum of the contributions of all the modes,

$$p(x,y,0) = \sum_{m=0}^{\infty} P_m \psi_m(x,y). \tag{3.6}$$

Now we recall the orthogonality of the modes from equation (2.47):

$$\int_S \psi_n \psi_m dS = S\delta_{nm}. \tag{3.7}$$

Multiplying p by ψ_n and integrating over the surface area therefore gives

$$\int_S p(x,y,0)\psi_n(x,y)dS = \sum_{m=0}^{\infty} \int_S P_m \psi_m(x,y)\psi_n(x,y)dS = P_n S. \tag{3.8}$$

When this is rearranged, the pressure amplitude of the nth mode is given in terms of the total pressure field as

$$P_n = \frac{1}{S}\int_S p(x,y,0)\psi_n(x,y)dS. \tag{3.9}$$

Now we will work out how the pressure and velocity modes couple. Substituting equation (3.5), which gives the total pressure field due to the contribution of the velocity modes, into equation (3.9) gives

$$P_n = \frac{i\omega\rho}{2\pi S^2} \sum_{m=0} U_m \int_S dS \int_S dS_0 \psi_m(x_0,y_0)\psi_n(x,y)\frac{e^{-ikh}}{h}. \tag{3.10}$$

This expression gives the pressure amplitude of the nth mode due to the contributions of all the velocity modes, not just the nth velocity mode. The modes are therefore coupled at the opening as was expected.

Looking back to equation (2.95), the relationship between the pressure and velocity modes was given as

$$\mathbf{P} = Z\mathbf{U} \tag{3.11}$$

where Z is known as the impedance matrix. $\mathbf{P}$ is the column vector whose nth element is the pressure amplitude of the nth mode, P_n. Similarly, $\mathbf{U}$ is the column vector whose mth element is the volume velocity amplitude of the mth mode, U_m. Expressing this in summation notation, we get

$$P_n = \sum_{m=0}^{\infty} Z_{nm} U_m. \tag{3.12}$$

Comparison of equations (3.10) and (3.12) yields

$$Z_{nm} = \frac{i\omega\rho}{2\pi S^2} \int_S dS \int_S dS_0 \psi_m(x_0, y_0) \psi_n(x, y) \frac{e^{-ikh}}{h} \tag{3.13}$$

where Z_{nm} is the (n, m) element of the impedance matrix and gives the contribution to the nth pressure mode by the mth velocity mode. Because this is the impedance at the open end, we call the impedance matrix here the "radiation impedance matrix". Note that we are integrating twice: first we integrate to get the pressure field at $(x, y, 0)$ due to the sum of all source elements and then

we integrate this pressure at every point in the piston to isolate a single modal pressure amplitude component.

3.6 Multimodal radiation impedance of a cylindrical duct terminated in an infinite baffle

Radiation from a circular opening occurs in the majority of musical wind instruments and loudspeaker systems. In this section we review the radiation impedance resulting from the coupling of higher order modes in a cylindrical pipe terminated in an infinite flange. The method is that of Zorumski [37].

3.6.1 Analysis

Expressing (3.13) in cylindrical coordinates for a cylindrical duct of radius R:

$$Z_{nm} = \frac{i\omega\rho}{2\pi S^2} \int_0^{2\pi} d\theta \int_0^R r dr \int_0^{2\pi} d\theta_0 \int_0^R r_0 dr_0 \psi_m(r_0, \theta_0) \psi_n(r, \theta) \frac{e^{-ikh}}{h} \tag{3.14}$$

where

$$h = [r^2 + r_0^2 - 2rr_0 \cos(\theta - \theta_0)]^{\frac{1}{2}}. \tag{3.15}$$

As discussed in section 2.4.1, we will be treating cylindrically symmetric modes only. From equation (2.48), the mode profile on the surface is

$$\psi_n = \frac{J_0(\gamma_n r/R)}{J_0(\gamma_n)} \tag{3.16}$$

where γ_n is the nth zero of the Bessel function J_1 and is tabulated in appendix A.

Now we will give e^{-ikh}/h in terms of τ, a dummy variable of integration. We will show that all the other variables of integration will then have an analytic solution. Sonine's integral from Watson [52] p.416 gives:

$$\frac{e^{-ikh}}{h} = k\int_0^\infty \tau(\tau^2-1)^{-\frac{1}{2}} J_0(\tau kh)d\tau. \tag{3.17}$$

The integrand is imaginary when $\tau < 1$ and real when $\tau > 1$. Care must be taken when choosing the sign of $(\tau^2-1)^{-\frac{1}{2}}$ with the negative and imaginary interpretation taken here when $\tau < 1$. Notice that we have been using the opposite sign convention from Zorumski [37] for the imaginary part throughout because we are assuming a time factor of $e^{i\omega t}$ rather than $e^{-i\omega t}$.

Neumann's addition formula [52] p.358 is

$$J_0(\tau kh) = \sum_{q=-\infty}^{\infty} J_q(\tau kr)J_q(\tau kr_0)e^{iq(\theta-\theta_0)}, \tag{3.18}$$

which can be substituted into (3.17) to give

$$\frac{e^{-ikh}}{h} = k \sum_{q=-\infty}^{\infty} e^{iq(\theta-\theta_0)} \int_0^{\infty} \tau(\tau^2-1)^{-\frac{1}{2}} J_q(\tau kr) J_q(\tau kr_0) d\tau. \tag{3.19}$$

Now substituting (3.19) into (3.14) we get

$$Z_{nm} = \frac{i\rho c}{2\pi S^2} \int_0^{2\pi} d\theta \int_0^R r dr \int_0^{2\pi} d\theta_0 \int_0^R r_0 dr_0 \psi_m(r_0)\psi_n(r)$$
$$\times k^2 \sum_{q=-\infty}^{\infty} e^{iq(\theta-\theta_0)} \int_0^{\infty} \tau(\tau^2-1)^{-\frac{1}{2}} J_q(\tau kr) J_q(\tau kr_0) d\tau. \tag{3.20}$$

Note that $\int_0^{2\pi} d\theta e^{iq\theta} = 0$ unless $q = 0$, in which case it is equal to 2π. Integrating by θ and θ_0 then gives a factor of $(2\pi)^2$. When rearranged, the integral can be reduced to

$$Z_{nm} = \frac{i\rho c}{S} \int_0^{\infty} \tau(\tau^2-1)^{-\frac{1}{2}} D_n(\tau) D_m(\tau) d\tau, \tag{3.21}$$

where

$$D_n(\tau) = \frac{k\sqrt{2}}{R} \int_0^R r J_0(\tau kr) \psi_n(r) dr. \tag{3.22}$$

The integration in equation (3.22) can be found analytically (see equation (A.1) in appendix A):

$$D_n(\tau) = \frac{-\sqrt{2}\tau J_1(\tau kR)}{(\frac{\gamma_n}{kR})^2 - \tau^2}. \tag{3.23}$$

The four dimensional integral has now been reduced to a one dimensional integration, with the variable h (and therefore the singularity mentioned at the end

of section 3.3.1) eliminated. Noticing that in equation (3.21) the integral is real for $0 < \tau < 1$ and imaginary for $1 < \tau < \infty$, we split the integral into real and imaginary parts with variables $\tau = \sin\phi$ and $\tau = \cosh\xi$ respectively.

$$Z_{nm} = \frac{i\rho c}{S} \int_0^{\frac{\pi}{2}} \sin\phi(\sin^2\phi - 1)^{-\frac{1}{2}} D_n(\sin\phi) D_m(\sin\phi) \cos\phi d\phi$$
$$+ \frac{i\rho c}{S} \int_0^{\infty} \cosh\xi(\cosh^2\xi - 1)^{-\frac{1}{2}} D_n(\cosh\xi) D_m(\cosh\xi) \sinh\xi d\xi. \qquad (3.24)$$

Now $\cosh^2\xi - 1 = \sinh^2\xi$ and $\sin^2\phi - 1 = -\cos^2\phi$. Remembering that the negative imaginary interpretation should be taken for the resulting $(-\cos^2\phi)^{-\frac{1}{2}}$ we get

$$Z_{nm} = \frac{\rho c}{S} \int_0^{\frac{\pi}{2}} \sin\phi D_n(\sin\phi) D_m(\sin\phi) d\phi$$
$$+ \frac{i\rho c}{S} \int_0^{\infty} \cosh\xi D_n(\cosh\xi) D_m(\cosh\xi) d\xi. \qquad (3.25)$$

The first integral can be performed by numerical integration using Simpson's rule or an equivalent. In the second integral, however, the range extends to infinity. The integrand is an oscillatory function of ξ whose amplitude of oscillation decays exponentially to 10^{-6} typically at around $\xi = 10$. Numerical integration can then be performed from 0 and 10 without incurring any significant numerical errors.

3.6.2 Results

Graphs of the radiation impedance at a circular opening in an infinite baffle were produced by performing the numerical integration in equation (3.25) for a number of dimensionless frequencies (kR). In order to keep the general applicability of the results, as is standard practice, we will normalise the radiation impedance by dividing through by $\rho c/S$ rather than choosing a particular value of $S = \pi R^2$. Remembering that the radiation impedance is a matrix whose element Z_{nm} gives the pressure amplitude of the nth mode due to a given volume velocity amplitude of the mth mode, it is useful to distinguish between the $n = m$ and $n \neq m$ elements. The $n = m$ elements are referred to as direct impedances since they give the contribution to a pressure mode by the velocity mode with the same amplitude distribution.

Figure 3.2 shows the real and imaginary parts of the first three direct radiation impedances for a cylindrical opening in an infinite baffle. The real part is known as the radiation resistance and a large positive value for this indicates that acoustic energy is radiated efficiently from the opening. The imaginary part is called the radiation reactance and a positive value for this indicates a mass loading of the air column [40] pp.191-192, or equivalently a length correction [45] pp.180-181. At low enough frequency the radiation impedance is effectively zero. In this case, no matter how large the velocity amplitude is, no pressure is produced, indicating the presence of a pressure node at the open end. The ideal open end condition

then holds.

At low frequencies, $ka << 1$ and the impedance is small and imaginary. The very low radiation resistance means that almost no sound is radiated from the instrument. Nearly all the sound is reflected back down the tube. The small imaginary value of the impedance means that the velocity produces a small pressure, 90 degrees out of phase in the time domain, as is the case close to a pressure node in a tube supporting standing waves. A pressure node is therefore present, but has been shifted slightly from the end of the tube, which is why a correction must be made to the tube length when calculating the length of the standing waves.

At intermediate frequencies the resistance becomes larger than the reactance. The oscillatory look of all the graphs which follow in this chapter result from local maxima which occur as the wavelength becomes comparable with the tube width. In the high frequency limit the radiation impedance converges to the real value 1 (or $\rho c/S$ before normalisation) which is the characteristic impedance of plane waves in free space. This indicates that the waves are not reflected at the opening, but propagate out of the tube undisturbed and with 100% efficiency. This agrees with the intuitive behaviour of wave diffraction from an opening; high frequency waves are transmitted in a beam of the same cross-section as the opening. Standing waves cannot be set up in this regime as no energy is reflected back to contribute to resonance.

Note how the direct impedances of the modes converge more slowly as n increases. The normalised characteristic impedance of the mode n from equation (2.36) is k/k_n which tends to 1 from above when $kR >> \gamma_n$. It is therefore observed that the radiation impedance tends to the characteristic impedance termination value, which in turn tends to 1, more slowly as n (and therefore γ_n) increases.

Next we consider the elements of the impedance matrix for which $m \neq n$. These are referred to as coupled impedances since they give the contribution to a pressure mode by a velocity mode with a different amplitude distribution. Figure 3.3(a) shows the radiation impedance resulting from the coupling of the plane wave pressure mode ($n = 0$) and the mth velocity mode for $m = 1$ and $m = 2$. Figure 3.3(b) shows the radiation impedance resulting from the coupling of the pressure mode with one nodal circle ($n = 1$) and the mth velocity mode for $m = 0$ and $m = 2$.

At the zero frequency limit, the coupled radiation impedances go to zero, indicating that there is no component of the nth pressure mode due to the mth velocity mode and therefore no coupling for $kR << 1$. At intermediate frequencies we can see non-zero impedance terms (less in magnitude than for direct impedances) which indicate a certain amount of inter-modal coupling is taking place. In the high frequency limit we observe the radiation impedance tending to zero. The infinite pipe termination or characteristic impedance condition has

no inter-modal coupling, or equivalently the $m \neq n$ elements of the characteristic impedance matrix have a value of zero. The radiation impedance matrix therefore tends to the characteristic impedance matrix at high frequencies for all elements, for those with $n \neq m$ in addition to those with $n = m$ discussed earlier.

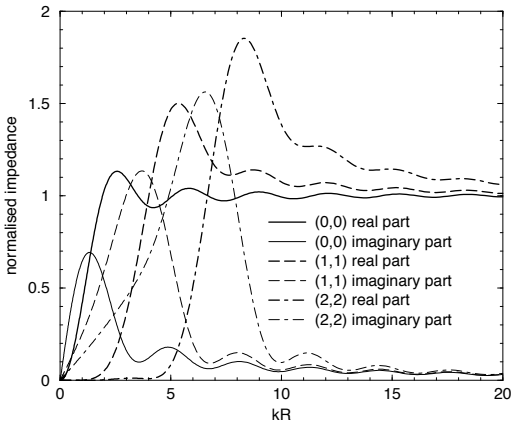

Figure 3.2: Normalised direct radiation impedance of the nth mode in a circular duct of radius R for $n = 0, 1, 2$.

3.7 Multimodal radiation impedance of a rectangular duct terminated in an infinite baffle

Radiation from a rectangular opening occurs in a variety of contexts, including organ pipes and horn drivers. This section derives an analytic expression for the radiation impedance resulting from the coupling of higher order modes in a rectangular pipe terminated in an infinite flange according to Kemp et al. [39]. Horn drivers mounted in loudspeaker cabinets are expected to be particularly

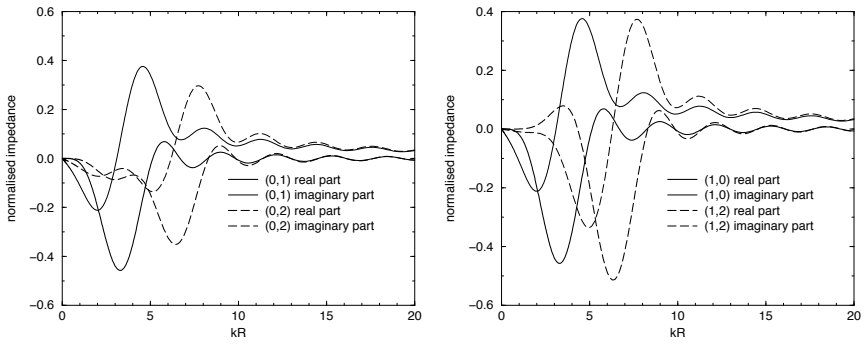

(a) Normalised coupled radiation impedance of the plane wave pressure and mth velocity mode for $m = 1, 2$.

(b) Normalised coupled radiation impedance of the pressure mode with one nodal circle ($n = 1$) and the mth velocity mode for $m = 0, 2$.

Figure 3.3: Coupled radiation impedances of a circular duct of radius R

suited to the infinite baffle approximation.

The radiation impedance for the modes of simply supported rectangular plates is also closely related to the current problem and is reviewed in Nelisse et al. [53].

3.7.1 Analysis

Consider a rectangular duct of half widths a and b terminated in an infinite baffle, as shown in figure 3.4.

Expressing (3.13) in rectangular coordinates for a rectangular duct of half-

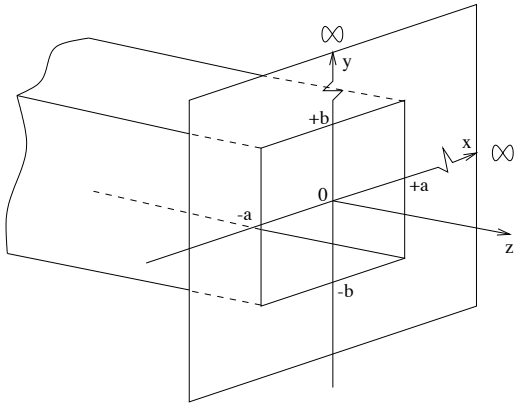

Figure 3.4: Geometry of infinitely flanged rectangular duct

widths a and b gives:

$$Z_{nm} = \frac{i\omega\rho}{2\pi S^2} \int_{-a}^{a} dx \int_{-b}^{b} dy \int_{-a}^{a} dx_0 \int_{-b}^{b} dy_0 \psi_m(x_0, y_0) \psi_n(x, y) \frac{e^{-ikh}}{h} \tag{3.26}$$

where

$$h = [(x - x_0)^2 + (y - y_0)^2]^{\frac{1}{2}}, \tag{3.27}$$

and

$$\psi_n = \phi_{n_x} \sigma_{n_y}, \tag{3.28}$$

with

$$\phi_{n_x} = N_{n_x} \cos\left(\frac{n_x \pi x}{a}\right), \tag{3.29}$$

$$\sigma_{n_y} = N_{n_y} \cos\left(\frac{n_y \pi y}{b}\right), \tag{3.30}$$

$$N_{n_x} = \begin{cases} 1 & : \quad n_x = 0, \\ \sqrt{2} & : \quad n_x > 0. \end{cases} \tag{3.31}$$

Changing variables as in Swenson et al. [49] and Levine [51] to $\xi = x - x_0$, $\eta = x + x_0$, $\zeta = y - y_0$, and $\mu = y + y_0$ the integral becomes

$$Z_{nm} = \frac{i\omega\rho}{2\pi S^2} \int_0^{2a} d\xi \int_0^{2b} d\zeta \frac{e^{-ikh}}{h} \int_{-2a+\xi}^{2a-\xi} d\eta \phi_{n_x} \phi_{m_{x0}} \int_{-2b+\zeta}^{2b-\zeta} d\mu \sigma_{n_y} \sigma_{m_{y0}} \tag{3.32}$$

where

$$h = \sqrt{\xi^2 + \zeta^2}. \tag{3.33}$$

The quadruple integral can now be reduced to a double integral by performing integration by η and μ analytically. The first step is to expand the cosines in equations (3.29) and (3.30):

$$\begin{aligned} \phi_{n_x} \phi_{m_{x0}} = N_n N_m \times \\ \Big[\cos(\tfrac{n_x \pi \xi}{2a}) \cos(\tfrac{m_x \pi \xi}{2a}) \cos(\tfrac{n_x \pi \eta}{2a}) \cos(\tfrac{m_x \pi \eta}{2a}) + \cos(\tfrac{n_x \pi \xi}{2a}) \sin(\tfrac{m_x \pi \xi}{2a}) \cos(\tfrac{n_x \pi \eta}{2a}) \sin(\tfrac{m_x \pi \eta}{2a}) \\ - \sin(\tfrac{n_x \pi \xi}{2a}) \cos(\tfrac{m_x \pi \xi}{2a}) \cos(\tfrac{n_x \pi \eta}{2a}) \sin(\tfrac{m_x \pi \eta}{2a}) - \sin(\tfrac{n_x \pi \xi}{2a}) \sin(\tfrac{m_x \pi \xi}{2a}) \sin(\tfrac{n_x \pi \eta}{2a}) \sin(\tfrac{m_x \pi \eta}{2a}) \Big]. \end{aligned} \tag{3.34}$$

The second and third terms go to zero since we are integrating over a symmetric

interval in η. Performing integration gives:

$$G(n_x, m_x, \xi, a) = \int_{-2a+\xi}^{2a-\xi} d\eta \phi_{n_x} \phi_{m_{x0}}$$
$$= N_{n_x} N_{m_x} (2a - \xi) \left[\text{sinc}\left((n_x + m_x)\pi \left(1 - \frac{\xi}{2a} \right) \right) \cos\left(\frac{(n_x - m_x)\pi\xi}{2a} \right) + \right.$$
$$\left. \text{sinc}\left((n_x - m_x)\pi \left(1 - \frac{\xi}{2a} \right) \right) \cos\left(\frac{(n_x + m_x)\pi\xi}{2a} \right) \right]. \quad (3.35)$$

The integral for the impedance is then:

$$Z_{nm} = \frac{i\omega\rho}{2\pi S^2} \int_0^{2a} d\xi \int_0^{2b} d\zeta \frac{e^{-ikh}}{h} G(n_x, m_x, \xi, a) G(n_y, m_y, \zeta, b). \quad (3.36)$$

Changing variables to $u = k\xi$ and $v = k\zeta$ means that the radiation impedance is expressed in terms of the dimensionless variables ka and kb:

$$Z_{nm} = \frac{i\rho c}{2\pi S} \int_0^{2ka} du \int_0^{2kb} dv \frac{e^{-i\sqrt{u^2+v^2}}}{\sqrt{u^2+v^2}} G\left(n_x, m_x, \frac{u}{2ka}, \frac{1}{2} \right) G\left(n_y, m_y, \frac{v}{2kb}, \frac{1}{2} \right). \quad (3.37)$$

Note that if we put $n_x = m_x = n_y = m_y = 0$ into equation (3.35) we obtain

$$G\left(n_x, m_x, \frac{u}{2ka}, \frac{1}{2} \right) G\left(n_y, m_y, \frac{v}{2kb}, \frac{1}{2} \right) = 4 \left(1 - \frac{u}{2ka} \right) \left(1 - \frac{v}{2kb} \right). \quad (3.38)$$

The radiation impedance from equation (3.37) is then identical to the radiation impedance of a rectangular piston in an infinite baffle [47, 48, 49, 50, 51] (note that most authors have used a and b as widths rather than half widths). Equation

(3.37) has a singularity at the origin if $n_x = m_x$ and $n_y = m_y$ which must be removed if the radiation impedance is to be calculated by numerical integration. To do this the integral is first split into two parts:

$$Z_{nm} = \frac{i\rho c}{2\pi S}\int_0^{2ka} du \int_0^{2kb} dv \frac{(1-\frac{u}{2ka})(1-\frac{v}{2kb})}{\sqrt{u^2+v^2}} \left[e^{-i\sqrt{u^2+v^2}} \frac{G(n_x, m_x, \frac{u}{2ka}, \frac{1}{2})}{(1-\frac{u}{2ka})} \frac{G(n_y, m_y, \frac{v}{2kb}, \frac{1}{2})}{(1-\frac{v}{2kb})} - f(n,m)\right] + \frac{i\rho c}{2\pi S}\int_0^{2ka} du \int_0^{2kb} dv \frac{(1-\frac{u}{2ka})(1-\frac{v}{2kb})}{\sqrt{u^2+v^2}} f(n,m) \tag{3.39}$$

where

$$f(n,m) = N_{n_x} N_{m_x} N_{n_y} N_{m_y} \times [\mathrm{sinc}((n_x+m_x)\pi) + \mathrm{sinc}((n_x-m_x)\pi)][\mathrm{sinc}((n_y+m_y)\pi) + \mathrm{sinc}((n_y-m_y)\pi)]. \tag{3.40}$$

The first part is non-singular and the singularity in the second half may be removed by integration, giving:

$$
\begin{aligned}
Z_{nm} = & \\
& \frac{i\rho c}{2\pi S} \int_0^{2ka} du \int_0^{2kb} dv \frac{(1-\frac{u}{2ka})(1-\frac{v}{2kb})}{\sqrt{u^2+v^2}} \times \\
& \qquad \left[e^{-i\sqrt{u^2+v^2}} \frac{G(n_x, m_x, \frac{u}{2ka}, \frac{1}{2})}{(1-\frac{u}{2ka})} \frac{G(n_y, m_y, \frac{v}{2kb}, \frac{1}{2})}{(1-\frac{v}{2kb})} - f(n,m) \right] \\
& + \frac{i\rho c}{2\pi S} \int_0^{2ka} du \left(1 - \frac{u}{2ka}\right) \times \\
& \qquad \left[\ln\left(2kb + \sqrt{u^2+(2kb)^2}\right) + \frac{u}{2kb} - \frac{1}{2kb}\sqrt{u^2+(2kb)^2} \right] f(n,m) \\
& + \frac{i\rho c}{2\pi S} \left[-ka \ln(2ka) + \frac{3}{2} ka \right] f(n,m). \qquad (3.41)
\end{aligned}
$$

Equation (3.41) may be evaluated by numerical integration to provide the radiation impedance.

3.7.2 Results

Taking $a = b$ gives the radiation impedance of a square duct terminated in an infinite baffle. It is interesting to compare this with the result derived by Zorumski [37] for the radiation impedance for a circular duct terminated in an infinite baffle. The direct impedance of the plane wave mode ($n = (0,0)$, $m = (0,0)$) for a square duct of half width a is shown in figure 3.5(a). Also shown is the equivalent for a circular duct of the same cross-sectional area (radius $= 2a/\sqrt{\pi}$). The results show very similar behaviour.

Figure 3.5(b) shows the impedance of the plane wave pressure mode ($n = (0,0)$) coupled with the $m = (0,2)$ velocity mode for a square duct of half width

a along with the plane wave pressure mode coupled with the pressure mode with two nodal circles in a cylindrical duct of the same cross-sectional area. While the analogue between the two situations is less strong, the same qualitative behaviour is observed.

Figures 3.6(a) and 3.6(b) display various direct radiation impedances for a square duct. As was the case with circular cross-section, the radiation impedance starts at zero for the zero frequency limit (as for the ideal open end condition). At low frequencies the impedance has a small, positive imaginary value. As with the circular cross-section discussion, this means that the acoustic pressure has a node a small distance from the end of the tube due to out of phase reflection of sound. At high frequencies the impedance converges on the infinite cylindrical pipe termination value of 1 (or $\rho c/S$ before normalisation). Modes with shorter transverse wavelengths converge more slowly.

Figure 3.7(a) and 3.7(b) display coupled radiation impedances for a square duct. Figure 3.7(a) shows examples where the pressure and velocity are direct in one dimension and coupled in the other. Figure 3.7(b) shows examples where the pressure and velocity are coupled in both dimensions with a correspondingly smaller range of impedance values. As with the cylindrical geometry, the coupled radiation impedance and therefore the amount of inter-modal coupling tends to zero in both the zero frequency and high frequency limits.

Figure 3.8(a) shows the effect of varying the aspect ratio (a/b) on the plane

wave pressure and plane wave velocity radiation impedance. This graph is in agreement with the values of the rectangular piston radiation impedance as published by Burnett and Soroka [48]. Making the opening rectangular rather than square while keeping the cross-sectional area constant is observed to make the direct impedance of the plane mode converge much more slowly on the characteristic impedance termination value. Physically this is a consequence of the opening having one very narrow dimension, meaning that higher frequencies must be accessed before the effects of diffraction at the opening disappear. The direct impedance of the plane mode in a duct of a given aspect ratio b/a will equal that of duct of aspect ratio b/a by symmetry. This effect only holds if the pressure distribution has the same number of nodal lines in both the x and y directions (ie. $n_x = n_y$) and the velocity distribution similarly has $m_x = m_y$.

Figure 3.8(b) shows the effect of aspect ratio on a coupled impedance. The velocity distribution has twice as many nodes on the y axis as there are on the x axis while the pressure mode is planar. The $a/b = 1$ case shows the coupled impedance for a square duct. Setting $a/b = 2$, the duct width along y direction is half that along x. The transverse wavelength of the velocity distribution is therefore four times as large along y as along x. The wavelength along one dimension is then very short, and we observe that higher frequencies must be reached before coupling takes place for the rectangular duct in comparison to a square duct of the same area. For $a/b = 0.5$ the duct is twice as wide in the y direction meaning that the transverse wavelength is the same along y as along x.

In this this case we therefore observe that coupling with the plane pressure mode can happen at lower frequencies for the rectangular duct.

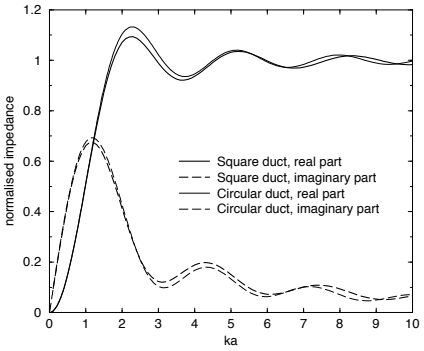

(a) Normalised direct radiation impedance for the plane wave mode in a square duct of half width a and a circular duct of the same area

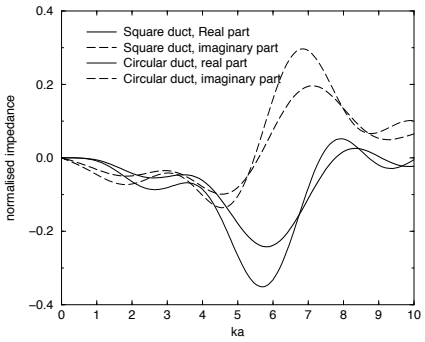

(b) Normalised coupled radiation impedance of the plane wave pressure and (0,2) velocity modes (square duct of half width a), and the plane wave pressure and two nodal circles velocity modes (circular duct of same area)

Figure 3.5: Radiation impedances of square and circular ducts

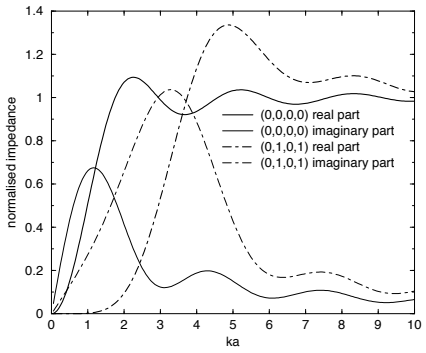

(a) Normalised direct radiation impedance of the $(0,n_y)$ mode in a square duct of half width a for $n_y = 0, 1$.

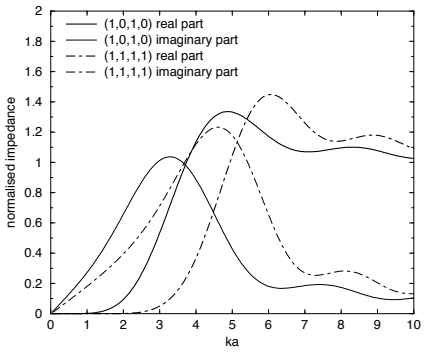

(b) Normalised direct radiation impedance of the $(1,n_y)$ mode in a square duct of half width a for $n_y = 0, 1$.

Figure 3.6: Direct radiation impedances of square ducts

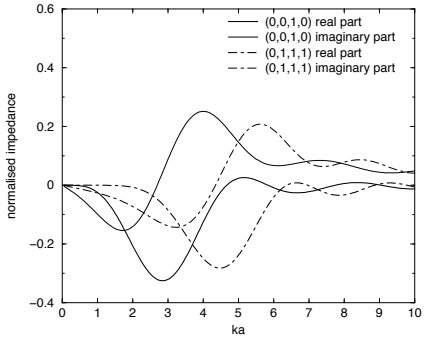

(a) Normalised coupled radiation impedance of the $(0,n_y)$ pressure and $(1,n_y)$ velocity modes in a square duct of half width a for $n_y = 0, 1$.

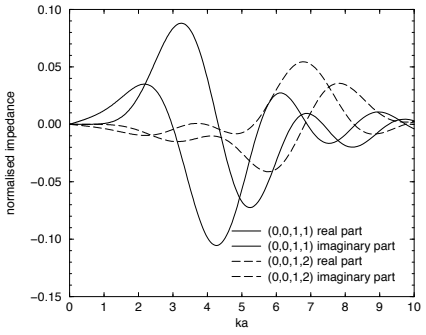

(b) Normalised coupled radiation impedance of the plane pressure and $(1,m_y)$ velocity modes in a square duct of half width a for $m_y = 1, 2$.

Figure 3.7: Coupled radiation impedances of square ducts

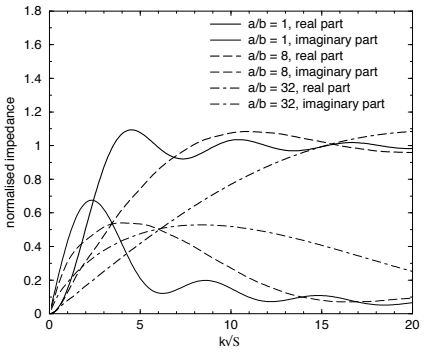

(a) Normalised direct radiation impedance of plane wave mode in a rectangular duct of half width a and half height b

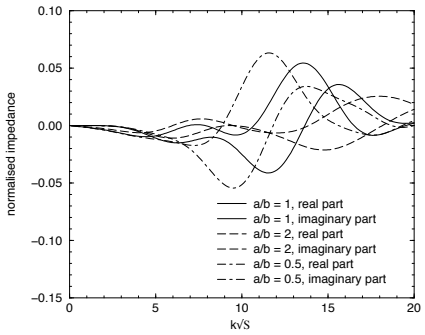

(b) Normalised coupled radiation impedance of plane pressure and (1,2) velocity modes in a rectangular duct of width a and height b

Figure 3.8: Effect of aspect ratio on radiation impedances of rectangular ducts

Chapter 4

Numerical implementation of multimodal theory

4.1 Review of input impedance method

In section 2.6 a multimodal method of calculating the input impedance and pressure field of a duct from a known terminating radiation impedance matrix was presented. In chapter 3 we went on to derive the expression for the radiation impedance matrix of a cylindrical pipe terminated in an infinite baffle. Now we will bring these together, reviewing the equations and giving numerical results for the input impedance and pressure field for an example object of cylindrical cross-section. The theoretical input impedance calculated here will be compared to experimental results in the following chapter.

4.1.1 The radiation impedance matrix

From section 3.6 the radiation impedance matrix for a cylindrical pipe terminated in an infinite baffle is:

$$Z_{nm} = \frac{\rho c}{S} \int_0^{\frac{\pi}{2}} \sin\phi D_n(\sin\phi) D_m(\sin\phi) d\phi + \frac{i\rho c}{S} \int_0^{\infty} \cosh\xi D_n(\cosh\xi) D_m(\cosh\xi) d\xi \tag{4.1}$$

where

$$D_n(\tau) = \frac{-\sqrt{2}\tau J_1(\tau kR)}{(\frac{\gamma_n}{kR})^2 - \tau^2}. \tag{4.2}$$

4.1.2 Projecting the impedance matrix

The equations for projection of the impedance matrix were derived in section 2.6. Remember that the labels (0), (1) and (2) refer to planes 0, 1 and 2 in figure 4.1.

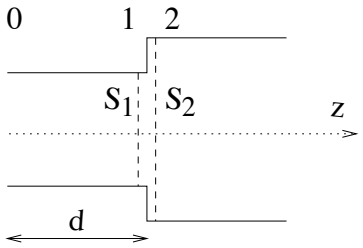

Figure 4.1: Detail of a waveguide consisting of straight sections of length d joined discontinuously

By way of summary, the equation for projection across a discontinuity is

$$Z^{(1)} = F Z^{(2)} F^{\mathrm{T}}, \qquad S_1 < S_2 \tag{4.3}$$

where $S_1 = \pi R_1^2$, $S_2 = \pi R_2^2$ are the cross-sectional areas and

$$Z^{(1)} = V^{-1} Z^{(2)} (V^{\mathrm{T}})^{-1}, \qquad S_1 > S_2. \tag{4.4}$$

The projection matrices are given by

$$F_{nm}(\beta) = \frac{2\beta\gamma_m J_1(\beta\gamma_m)}{(\beta^2\gamma_m^2 - \gamma_n^2) J_0(\gamma_m)} \tag{4.5}$$

where $\beta = R_1/R_2$ with $F(0,0) = 1$ and $V_{nm}(\beta) = F_{nm}(1/\beta)$.

The equation for projection through a distance d is

(N.B. This is a correction to the original version of my thesis and D_2 is given in equation (2.41))

$$Z^{(0)} = \left(iD_3\right)^{-1} Z_c - D_2^{-1} Z_c \left(Z^{(1)} + \left(iD_3\right)^{-1} Z_c\right)^{-1} D_2^{-1} Z_c \tag{4.6}$$

where

$$D_3(n,m) = \begin{cases} \tan(k_n d) & : \quad n = m, \\ 0 & : \quad n \neq m. \end{cases} \tag{4.7}$$

Here

$$k_n = \begin{cases} -\sqrt{k^2 - \left(\frac{\gamma_n}{R}\right)^2} & : \quad k < \frac{\gamma_n}{R}, \\ \sqrt{k^2 - \left(\frac{\gamma_n}{R}\right)^2} & : \quad k > \frac{\gamma_n}{R}. \end{cases} \tag{4.8}$$

is the wavenumber of the nth mode along the tube neglecting the effect of losses; the corresponding expression for lossy propagation is given in section 2.4.1. γ_n is the nth zero of the Bessel function J_1 as tabulated in appendix A.

4.2 Numerical implementation

Starting from the radiation impedance matrix, the equations above can be used to project the impedance matrix along cylinders and across discontinuities alternately until the input end is reached, giving the input impedance matrix. Remembering that the element Z_{nm} gives the contribution to the pressure of the nth mode due to a given volume velocity of the mth mode, the corner value (Z_{00}) gives the component of the plane pressure due to a given plane volume velocity.

If the air column is driven by a plane piston vibrating sinusoidally at the input end with a velocity amplitude of v_z, we know the acoustic volume velocity will be planar with a volume velocity amplitude of $U = v_z S$. Physically, the corner value thus corresponds to the ratio of the plane component of the pressure and the (planar) volume velocity. The objects we are interested in (such as brass musical instruments) are much narrower at the input end than any wavelength present in the excitation meaning that higher modes will not propagate there. On the other hand, in most brass instruments there is a fairly rapid change of area in the mouthpiece. This causes some loss of energy to evanescent higher modes.

In chapter 5 we will verify our theoretical results using the experimental technique of acoustic pulse reflectometry. It is difficult to put significant energy into the main bore of the instrument using this technique when the mouthpiece is in place. In order to compare the experiment with theory effectively we will therefore perform all experiments and theoretical calculations in the absence of the mouthpiece.

The objects we will be looking at will therefore be both narrow and approximately cylindrical at the input. Higher modes will not be excited at the input and both the pressure and volume velocity are plane there. The corner value of the input impedance matrix can then be labelled as the input impedance without ambiguity. The theoretical results which follow plot the corner value of the input impedance matrix calculated at a range of frequencies of musical interest, showing maxima at resonances of the air column.

Because there are, in principle, an infinite number of modes in a cylindrical pipe, the vectors and matrices used in the calculation should ideally be infinite. In practice, however, at high enough mode numbers the pressures represented are insignificant to the propagation of sound. This is because they have very high cut-off frequencies so are strongly damped and have negligible coupling with the plane mode.

The matrices can then be truncated to exclude all modes with mode numbers above a certain value. Note that we cannot exclude all mode numbers which

are in cut-off; energy lost from propagating modes to the many non-propagating modes with lower mode numbers must still be modelled for an accurate analysis. In practice, the number of propagating modes depends on the maximum radius in the object while the number of significant non-propagating modes also depends on the flare rate. The calculation must be repeated including more and more modes until the answer converges (ie. adding more modes only changes the answer by a small factor corresponding to the percentage error required). The length of time taken to perform the calculation increases exponentially as the number of modes increases since matrix multiplication is involved.

In addition to the number of modes under consideration, the number of cylinders used in approximating the bore is another numerical consideration. Obviously the more cylinders used in approximating the bore, the closer the approximate bore will resemble the actual bore of the instrument. The values in the impedance matrix converge on a final answer as the number of cylinders increase with the computational load increasing linearly. The number of cylinders required depends on the flare rate.

As mentioned previously, viscothermal losses may be included in the calculation by using a lossy wavenumber. The effect of losses may be determined by performing calculations with and without losses.

z (cm)	0	0.2	0.7	7.0	11.02	11.87	16.21	20.73	25.0
R (mm)	6.8	6.5	6.5	6.5	6.5	6.72	7.32	8.25	9.12
z (cm)	29.7	34.5	36.9	39.0	42.5	45.4	48.2	49.7	50.4
R (mm)	10.07	11.7	12.7	13.7	16.2	19.8	32.7	47.5	64.5

Table 4.1: Trumpet section dimensions

4.3 Results for a trumpet section

The next step is to calculate the input impedance of an object to give an example of the convergence of the calculation. We chose to perform the calculation on a bore which matches that of the bell section of a standard trumpet. The section was obtained by simply cutting the instrument in two after the valve section and 50.4 cm before the open end of the bell. Physical measurement of the bore was performed using calipers and the results are listed in table 4.1. In order to perform the multimodal calculation, we need to know the radius at any point along the bore, not just at the measured points. This was obtained by 3rd order polynomial interpolation using the two nearest data points on each side of the place of interest.

A calculation of the input impedance of the trumpet section was performed using the lossy wavenumber given in section 2.4.1 and using the non-lossy wavenumber of equation (4.8). The first 11 modes were included in the calculation and the horn was approximated by 1000 cylinders, each of length 0.504 mm. Figure 4.2 shows the absolute value of the input impedance for these calculations.

Inclusion of losses is observed to decrease the strength of resonance behaviour in the instrument. The height and frequency of the peaks in the input impedance are reduced. This is characteristic of loss of energy; less pressure is built up for the same excitation velocity at resonance. The depth of the troughs are reduced at impedance minima when losses are included because the reflections which return from the open end of the instrument are less strong, so decreasing the destructive interference responsible for anti-resonance.

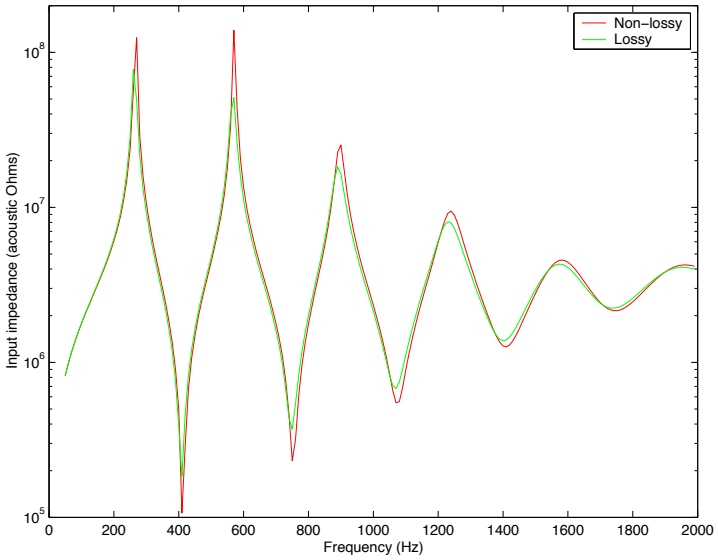

Figure 4.2: Trumpet section input impedance

Figure 4.3 shows the absolute value of the input impedance of the trumpet section calculated with the first 11 modes included and the lossy wavenumber used. The calculation was performed by approximating the horn by 100 cylinders of length 5.04 mm, then the calculation was repeated using 500 cylinders of length 1.008 mm and 1000 cylinders of length 0.504 mm.

The results are very similar, showing that the input impedance calculation is not sensitive to the exact step size chosen. The 500 and 1000 cylinder calculations show convergence to an accuracy of 2%. This accuracy is good enough for this type of calculation because peaks and troughs differ by several orders of magnitude, as can be seen from the logarithmic scale.

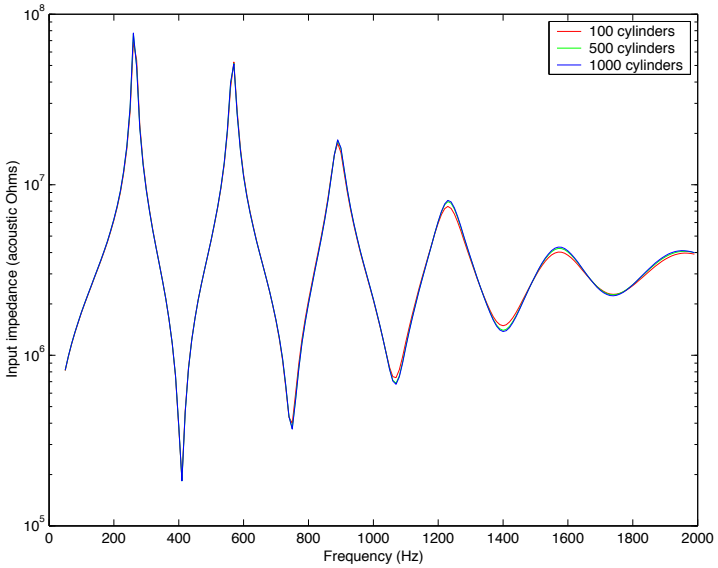

Figure 4.3: Trumpet section input impedance

Figure 4.4 shows how the calculation of the absolute value of the input impedance of the trumpet section (approximated by 1000 cylinders with the lossy wavenumber used) varies with number of modes included. Results are shown when the vectors and matrices in the calculation are truncated to 1 mode (which gives a plane wave calculation), 2, 3, 7 and 11 modes. The 7 and 11 mode calculations show convergence to 2% indicating that the inclusion of more modes in the

calculation would have no significant effect.

It is worth noting the cut-off frequency of the second mode (first non-planar mode) at the bell. Here the radius is maximum at $R = 6.45$ cm and so the cut-off frequency is at its minimum at $f_c = k_c c/(2\pi) \approx 3.83 \times 343/(0.0645 \times 2\pi) \approx 3240$ Hz. All modes except the plane mode are in cut-off (ie. are strongly evanescent) at all points along the trumpet in the frequency range of interest. The input impedance of the first five or so modes clearly still has an effect on the input impedance due to mode coupling. Including extra modes has a similar qualitative effect to the inclusion of viscothermal losses. The frequency and height of the impedance peaks are reduced at resonance while the anti-resonance behaviour is less marked because of the energy lost due to coupling with evanescent modes.

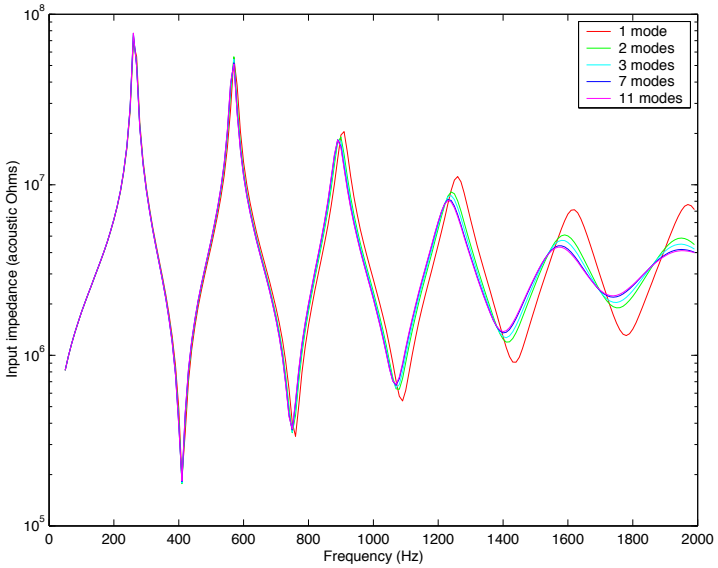

Figure 4.4: Trumpet section input impedance

The impedance matrix was stored at each step along the guide for the 580 Hz excitation, and this information was used to calculate the complex pressure amplitude vector at each step using the method described in section 2.7. Figure 4.5 shows the resulting pressure field when the calculation is truncated to 1, 2, 3, 5 and 11 modes. The frequency 580Hz is just above the second resonance peak. At the input, the phase angle is $\phi_0 = -1.06 = -0.337\pi$ radians which indicates that the volume velocity is leading the pressure. This is characteristic of a tube playing above resonance [2]. Results not presented here for frequencies just below resonance show a very similar pressure field but with the pressure leading the velocity at the input.

Red indicates a global maximum pressure and blue a global minimum pressure while the black lines are equipotential contours. All graphs show the same qualitative pressure along the axis of the horn. There are two pressure anti-nodes along the axis of the horn because we are close to the second resonance frequency of the horn. The first is a pressure maximum at the input end indicated by the red colour. The second anti-node is 180 degrees out of phase with the first and so gives a negative pressure peak (ie. global pressure minimum) at this point in the resonance cycle. It is visible as the dark blue colour 27 cm down the horn. The are two pressure nodes. The first is where the acoustic pressure crosses zero around 15 cm down the horn. The other is where the acoustic pressure approaches zero at the bell. These are represented by a mid-range colour, turquoise.

The plane mode calculation has flat pressure wavefronts as expected. The 2 mode calculation allows the pressure on a cross-section to be the sum of the plane wave and the $n = 2$ mode pressure distribution which has a maximum in the middle, one nodal circle and a local maximum at the edge. The resulting pressure map therefore shows non-planar pressure wavefronts. As more modes are added, the pressure field converges to show wavefronts meeting the wall at 90 degrees as required by the hard walled boundary condition. Notice that the radius and z scales are the same, as required to prevent distortion of the angle at which the equipressure contours meet the wall.

Figure 4.6 shows a close up of the 11 mode pressure field at the bell. Here the equipressure contours can be seen as stripes of uniform colour, without the aid of black lines. Notice that the colour map has been changed in that the full range of colours are used for an area of bore which was previously all the same colour. The node at the bell has an acoustic pressure of approximately zero while the nearest anti-node on the left has negative acoustic pressure. The node at the bell is therefore the maximum pressure on the graph and is represented by red. The increasingly negative acoustic pressures on the left then give the minimum pressures present, represented by dark blue.

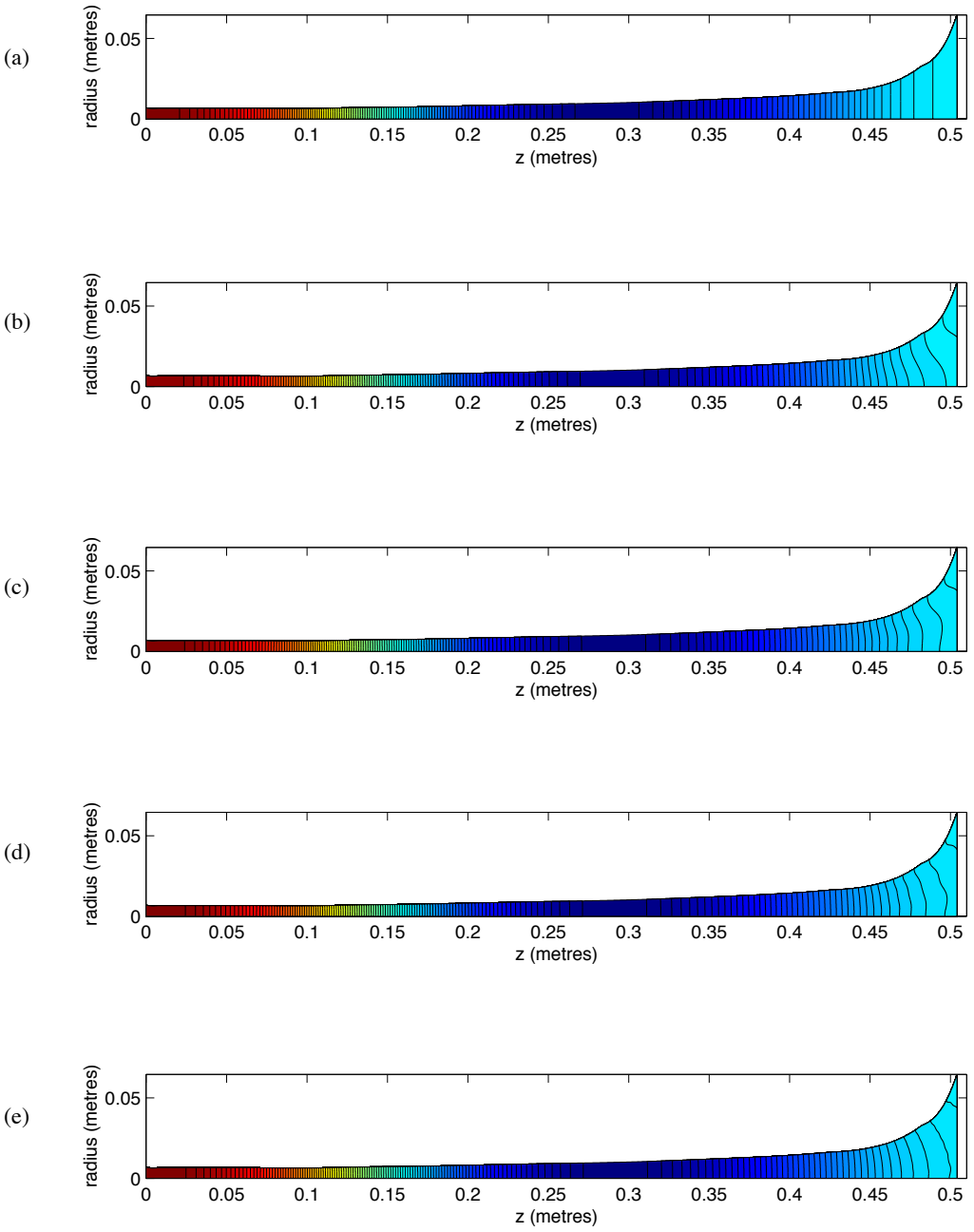

Figure 4.5: Trumpet section pressure field: (a) plane wave approximation, (b) 2 modes, (c) 3 modes, (d) 5 modes, (e) 11 modes

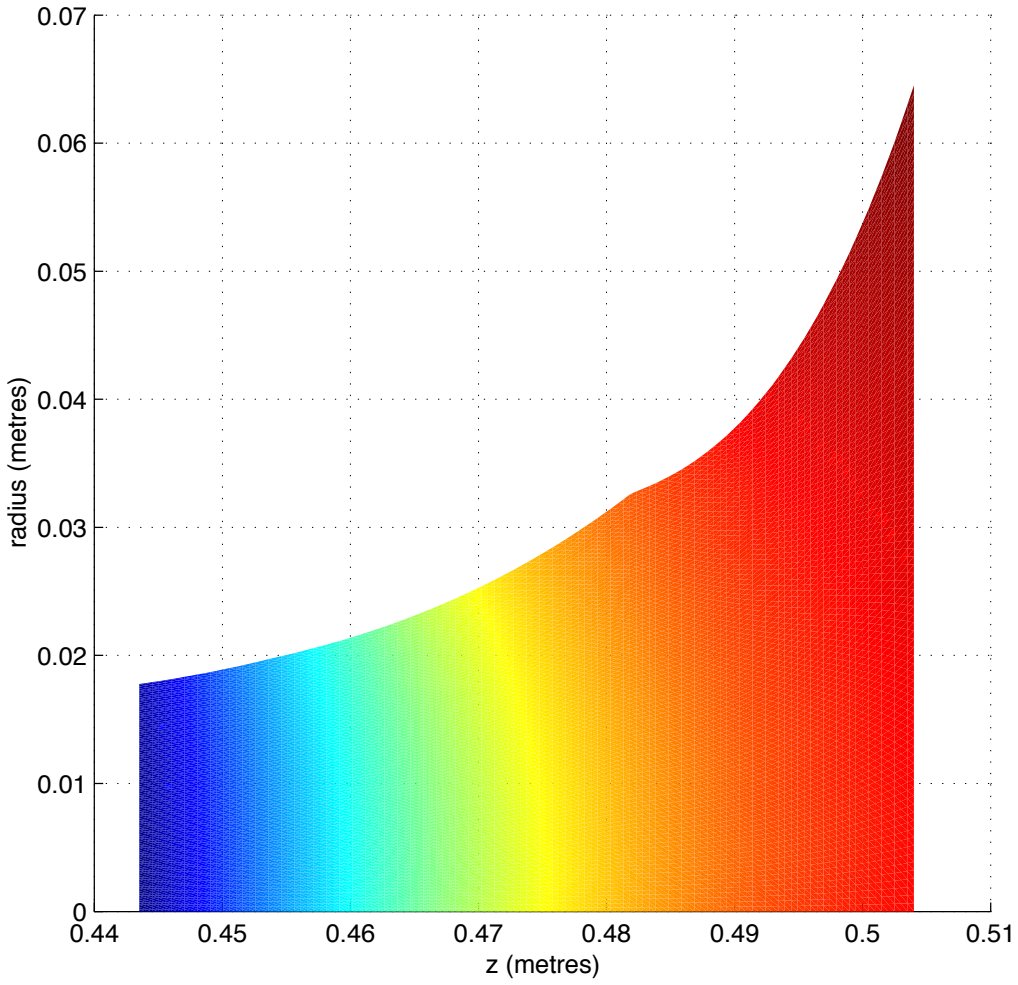

Figure 4.6: Trumpet section pressure field: 11 modes

Chapter 5

Acoustic pulse reflectometry

5.1 Introduction

Acoustic pulse reflectometry was introduced in section 1.5.2. Here we describe the apparatus and theory used in applying the technique for the measurement of musical wind instruments. The apparatus used was developed by Sharp et al. [6, 19, 20]. An acoustic pulse or audible click is produced by a loudspeaker and is directed down a cylindrical source tube and into the object to be measured. The resulting reflections are then measured and analysed to find the internal profile and input impedance.

Since we are sampling digitally, we receive information on the reflections from the instrument once every sample (ie. once every $T = 1/F_s$ seconds where F_s

is the same rate). The result is that information is obtained on the change in internal profile at discrete points along the instrument's bore. The reconstructed bore will therefore be approximated by a series of cylinders whose length is such that the primary reflections from successive cylinders occur at the sample rate.

5.2 Input impulse response

Consider an object connected to a source tube as shown in figure 5.1. Notice that for a musical wind instrument, the input plane is the position at which the mouthpiece must be placed if the instrument is to be played. In order to carry out pulse reflectometry experiments, the mouthpiece must be removed to prevent leaks and to allow efficient transfer of acoustical energy into and out of the instrument. The length of the cylindrical sections is $l = cT/2$ where $T = 1/F_s$ is the sample period such that the time for travel from the left hand side of a cylinder to the right hand side, reflection off the discontinuity and return to the left hand side will correspond to one sample in the time domain.

We label section 1 as the plane at the end of the source tube. The forward and backward going waves here are labelled $p_+^{(1)}$ and $p_-^{(1)}$ respectively. Section 2 is then the plane immediately on the other side of the input plane discontinuity. Section 3 is a distance l away at the other end of the first cylindrical section used in approximating the bore of the object. Section 4 is the plane immediately on

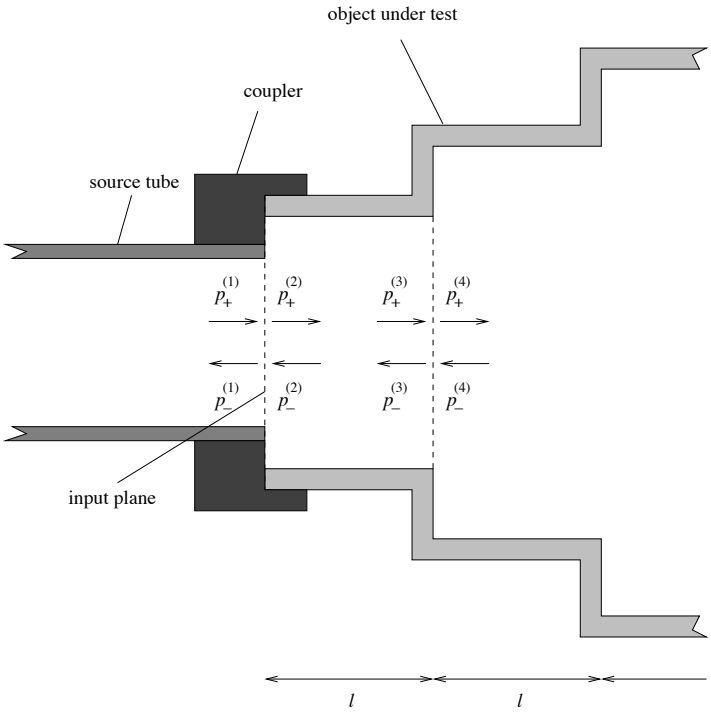

Figure 5.1: Travelling waves in a typical object split into cylindrical sections

the other side of the next discontinuity and so on.

We define the input impulse response as the sequence of reflections which return from the object under test when an ideal delta function impulse is fed into the input. We define $t = 0$ as the time of arrival of the input pulse at the input plane. The forward going wave on section 1 is then an impulse

$$p_+^{(1)}[nT] = \delta[nT] = \begin{cases} 1 & : \quad n = 0, \\ 0 & : \quad n \geq 1 \end{cases} \tag{5.1}$$

where $T = 1/F_s$ is the same period. n is an integer running from 0 to $N - 1$

where N is the total number of samples taken. The backward going wave is the input impulse response:

$$p_{-}^{(1)}[nT] = iir[nT]. \tag{5.2}$$

5.3 Input impedance from the input impulse response

We will use the theory of plane wave propagation as set out at the start of chapter 2 for the analysis which follows in this chapter. The possibility of including higher mode effects in the analysis will be discussed in chapter 7.

The pressure at the input to a tubular object will be the sum of the forward and backward going waves from equations (5.1) and (5.2):

$$p^{(1)}[nT] = \delta[nT] + iir[nT]. \tag{5.3}$$

Similarly, the volume velocity follows from equation (2.7), giving

$$U^{(1)}[nT] = \frac{S}{\rho c}(\delta[nT] - iir[nT]). \tag{5.4}$$

The input impedance is defined as the ratio of the pressure and volume velocity at the input plane. So far we have obtained a time domain expression for the

pressure and volume velocity if the input impulse response is known. The input impedance is generally frequency dependent however, so we must take the Fourier transform of the signals and divide the frequency components to get the input impedance at a particular frequency. The Fourier transform of an impulse is 1 for all frequencies. We define $IIR(\omega)$ as the Fourier transform of $iir[nT]$. The Fourier transform of the pressure is then

$$p^{(1)}(\omega) = 1 + IIR(\omega) \tag{5.5}$$

and the volume velocity is

$$U^{(1)}(\omega) = \frac{S}{\rho c}(1 - IIR(\omega)). \tag{5.6}$$

Dividing in the frequency domain gives the input impedance as

$$Z^{(1)}(\omega) = \frac{\rho c}{S}\frac{1 + IIR(\omega)}{1 - IIR(\omega)}. \tag{5.7}$$

This equation lets us easily calculate the input impedance of an object once the input impulse response is obtained by measurement. Since it is impossible to produce a perfect impulse, measurement of the input impulse response is not a straight forward task and will be discussed later in the chapter. For now we proceed with the background theory to pulse reflectometry.

5.4 Layer peeling bore reconstruction

We now want to analyse the input impulse response to find out the reflection coefficients (and therefore the changes in cross-section) at each step along the bore. This will enable us to reconstruct the bore profile. Bore reconstruction was first performed using the algorithm developed by Ware and Aki [7] as reviewed in [6]. Since losses cannot be incorporated in the Ware Aki algorithm, we will instead use the lossy reconstruction method developed by Amir et al. [17] as used by Sharp [6, 19, 20].

Consider a junction between two infinite tubes. If a pressure wave is incident from negative infinity and no wave is incident from positive infinity, then the ratio of the backward and forward going waves is given by the reflection coefficient of equation (2.20).

Going back to the general case of an object attached to the source tube of a reflectometer from figure 5.1, at the first time step (ie. when the forward going pulse arrives at the input plane), there cannot be any backward going waves on surface 2. The ratio of the first term in the reflection sequence (or input impulse response) and the first term in the input sequence (which is unity) is therefore equal to the reflection coefficient from equation (2.20). We will label this reflection coefficient as $r_{1,2}$. The subscripts indicate that this reflection coefficient is for reflection from the discontinuity between surfaces 1 and 2 when waves are

incident from the surface 1 side only.

$$r_{1,2} = \frac{S_1/S_2 - 1}{S_1/S_2 + 1}, \tag{5.8}$$

$$r_{1,2} = \frac{p_-^{(1)}[0T]}{p_+^{(1)}[0T]} = iir[0T], \tag{5.9}$$

where we have labelled the surface area of surface 1 as S_1 and the surface area of surface 2 as S_2. Now S_2 follows from S_1 and $r_{1,2}$ by rearranging equation (5.8):

$$S_2 = S_1 \left(\frac{1 - r_{1,2}}{1 + r_{1,2}} \right). \tag{5.10}$$

Now we know the cross-section on section 2, we will proceed to calculate the forward and backward going time sequences there. The forward going wave on section 2 is equal to the sum of the transmission of the forward going wave on section 1 and reflection of the backward going wave on section 2. Similarly, the backward going wave on section 1 is equal to the sum of the transmission of the backward going wave on section 2 and the reflection of the forward going wave on section 1. It can be expressed in matrix notation as follows:

$$\begin{pmatrix} p_+^{(2)}[nT] \\ p_-^{(1)}[nT] \end{pmatrix} = \begin{pmatrix} t_{1,2} & r_{2,1} \\ r_{1,2} & t_{2,1} \end{pmatrix} \begin{pmatrix} p_+^{(1)}[nT] \\ p_-^{(2)}[nT] \end{pmatrix}. \tag{5.11}$$

$r_{2,1}$ gives the reflection coefficient from the discontinuity between surfaces 2 and

1 when waves are incident from the surface 2 side only:

$$r_{2,1} = \frac{S_2/S_1 - 1}{S_2/S_1 + 1} = \frac{1 - S_1/S_2}{S_1/S_2 + 1} = -r_{1,2}. \tag{5.12}$$

$t_{1,2}$ gives the transmission coefficient from the discontinuity between surfaces 1 and 2 when waves are incident from the surface 1 side only. From equation (2.21) this is

$$t_{1,2} = \frac{2S_1/S_2}{S_1/S_2 + 1} = 1 + \frac{S_1/S_2 - 1}{S_1/S_2 + 1} = 1 + r_{1,2}. \tag{5.13}$$

$t_{2,1}$ gives the transmission coefficient from the discontinuity between surfaces 2 and 1 when waves are incident from the surface 2 side only:

$$t_{1,2} = \frac{2S_2/S_1}{S_2/S_1 + 1} = 1 - \frac{S_1/S_2 - 1}{S_1/S_2 + 1} = 1 - r_{1,2}. \tag{5.14}$$

We may rearrange the simultaneous equations in equation (5.11) to give the travelling waves on the right of the discontinuity in terms of the travelling waves on the left of the discontinuity:

$$\begin{pmatrix} p_+^{(2)}[nT] \\ p_-^{(2)}[nT] \end{pmatrix} = \frac{1}{1 - r_{1,2}} \begin{pmatrix} 1 & -r_{1,2} \\ -r_{1,2} & 1 \end{pmatrix} \begin{pmatrix} p_+^{(1)}[nT] \\ p_-^{(1)}[nT] \end{pmatrix}. \tag{5.15}$$

This equation is performed for all values of n from 0 to $N-1$. For the current situation, the forward going sequence on surface 1 is an impulse, $p_+^{(1)}[nT] = \delta[nT]$, and the backward going pressure sequence on surface 1 is the input impulse

response, $p_{-}^{(1)}[nT] = iir[nT]$. Notice that

$$p_{-}^{(2)}[0] = -r_{1,2} \times \delta[0] + 1 \times iir[0] = 0 \tag{5.16}$$

as no reflections return from surface 3 until $t = T$.

The forward travelling pressure sequence, at the right hand side of the cylindrical section, will be found simply by adding a delay time of $T/2 = l/c$ to the forward going wave on the left, to account for the time taken to travel a distance of l.

$$p_{+}^{(3)}\left[\left(n + \frac{1}{2}\right)T\right] = p_{+}^{(2)}[nT]. \tag{5.17}$$

$p_{+}^{(3)}$ is therefore known at $t = T/2$ and in steps of T up to $t = (N - 1/2)T$.

The backward travelling wave at surface 3 is found by subtracting a delay of $T/2$ from the backward travelling wave at surface 2.

$$p_{-}^{(3)}\left[\left(n - \frac{1}{2}\right)T\right] = p_{-}^{(2)}[nT]. \tag{5.18}$$

$p_{-}^{(3)}$ is therefore known at $t = -T/2$ and in steps of T up to $t = (N - 3/2)T$. Notice that there is no backward going wave on surface 3 until $t = T/2$:

$$p_{-}^{(3)}[-T/2] = p_{-}^{(2)}[0] = 0 \tag{5.19}$$

since no waves reach surface 3 until this time.

The ratio of the backward and forward travelling waves at surface 3, at time $t = T/2$, is equal to the reflection coefficient $r_{3,4}$ since this corresponds to a primary reflection.

$$r_{3,4} = \frac{p_{-}^{(3)}[T/2]}{p_{+}^{(3)}[T/2]}. \tag{5.20}$$

5.4.1 Numerical implementation issues

In terms of numerical implementation of the algorithm, the time domain pressure travelling waves are stored in vectors with elements referred to by an index (which we shall call i) which runs from 1 to N. Care must be taken over what time is represented by the index. On surfaces 1 and 2 we know the pressure at $t = 0$, T, $2T, \ldots, (N-1)T$ so the ith element of the vector in the numerical implementation therefore corresponds to the pressure at time $t = (i-1)T$.

Equations (5.9) and (5.15) are then simply

$$r_{1,2} = \frac{p_{-}^{(1)}(i=1)}{p_{+}^{(1)}(i=1)}, \tag{5.21}$$

$$\begin{pmatrix} p_{+}^{(2)}(i) \\ p_{-}^{(2)}(i) \end{pmatrix} = \frac{1}{1-r_{1,2}} \begin{pmatrix} 1 & -r_{1,2} \\ -r_{1,2} & 1 \end{pmatrix} \begin{pmatrix} p_{+}^{(1)}(i) \\ p_{-}^{(1)}(i) \end{pmatrix}. \tag{5.22}$$

The forward going pressure wave on surface 3 is sampled at $t = T/2$, $3T/2$, $5T/2$, ..., $(N-1/2)T$ and the ith element refers to the time $t = (i-1/2)T$.

Comparison with equation (5.17) then yields

$$p_+^{(3)}(i) = p_+^{(2)}(i). \tag{5.23}$$

For the pressure on surface 3, we know the backward going pressure at $t = -T/2$, $T/2$, $3T/2$, ..., $(N - 3/2)T$. At $t = -T/2$ the backward going pressure is zero, so we only need to carry on using the non-zero pressures at $t = T/2$,$3T/2$, ..., $(N - 3/2)T$. The ith element refers to the time at $t = (i - 1/2)T$. Comparison with equation (5.18) gives

$$p_-^{(3)}(i) = p_-^{(2)}(i + 1). \tag{5.24}$$

The pressure waves $p_+^{(3)}(i)$ and $p_-^{(3)}(i)$ are then the forward going and backward going sequences for the left hand side of the junction at surface 3. We have therefore peeled off the first layer in the object. Equations (5.21) to (5.24) can then be used to peel off the next layer. First the primary reflection coefficient for the junction from surface 3 to surface 4 is calculated, then the forward and backward travelling waves on surface 4 are obtained and then the delay for travel along the cylinder to next discontinuity is added. The algorithm repeats as necessary, peeling off successive layers in the object, calculating the new cross-section using equation (5.10) each time.

5.4.2 Losses

So far the effect of propagating waves down each cylindrical section is simply represented by a delay of $T/2$, therefore ignoring losses. A way of including losses in the layer peeling algorithm has been presented by Amir et al. [18].

The frequency domain formula for losses associated with propagation of plane acoustic waves down a tube of length L, due to Keefe [54], forms the basis of the inclusion of losses in the layer peeling algorithm. The effect of losses are characterised by the complex wavenumber, k:

$$k = \chi + i\kappa \tag{5.25}$$

where κ is the frequency dependent attenuation due to boundary layer effects, while $\chi = \omega/v_p$ is the ratio of the angular frequency and the phase velocity for propagation of sound along the tube. They are given by Keefe [54] as:

$$\chi = \frac{\omega}{c}\left[1 + \frac{A}{r_v} - \frac{C}{r_v^3}\right], \qquad \kappa = -\frac{\omega}{c}\left[\frac{A}{r_v} + \frac{B}{r_v^2} + \frac{C}{r_v^3}\right] \tag{5.26}$$

where the normalised boundary layer thickness is $r_v = R(\rho\omega/\eta)^{1/2}$ and depends on the tube radius, R. ρ is the density and η is the coefficient of viscosity of air. The coefficients A, B and C are also functions of the thermodynamic constants

ρ	=	$1.1769(1-0.00335\Delta T)$kg m^{-3}
η	=	$1.846\times10^{-5}(1+0.0025\Delta T)$Pa s
γ	=	$1.4017(1-0.00002\Delta T)$
ν	=	$0.8410(1-0.0002\Delta T)$
c	=	$347.23(1+0.00166\Delta T)$m s^{-1}

Table 5.1: Thermodynamic constants

of air:

$$A=\frac{1+b_1}{\sqrt{2}},\qquad B=1+b_1-\frac{b_1}{2\nu}-\frac{b_1^2}{2},$$
$$C=\frac{1}{\sqrt{2}}\left(\frac{7}{8}+b_1-\frac{b_1}{2\nu}-\frac{b_1}{8\nu^2}-\frac{b_1^2}{2}+\frac{b_1^2}{2\nu}+\frac{b_1^3}{2}\right) \tag{5.27}$$

with $\nu=\frac{\eta C_p}{\kappa}$ where C_p is the specific heat of air at constant pressure, κ is the thermal conductivity of air and $b_1=\frac{\gamma-1}{\nu}$ where γ is the ratio of the specific heats of air. Temperature dependent values of the thermodynamic constants of air due to Keefe [54] are provided in table 5.1. The imaginary part of the wavenumber responsible for attenuation is then $-2.92\times10^{-5}f^{1/2}/R$ for $T=20^o$, which agrees with the value quoted in Kinsler et al. [40] to within 1% and differs from the plane wave value from the multimodal losses theory due to Bruneau [44] by 3%.

This means that the resulting transmission coefficient is:

$$\Gamma(\omega)=\exp(-ikL) \tag{5.28}$$

There are numerical difficulties which arise when trying to use this as a filter

within the bore reconstruction algorithm. These issues are treated in detail by Amir et al. [18].

5.5 Apparatus

A schematic diagram of the apparatus used is shown in figure 5.2 and a photograph of the apparatus is shown in figure 5.3.

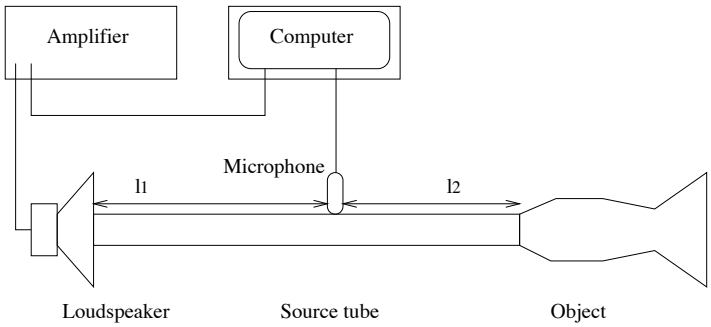

Figure 5.2: Schematic diagram of the apparatus

The computer sends out a 5 V electrical pulse of 80 μs duration to an audio amplifier. A horn driver loudspeaker attached to the output then produces an acoustic pulse (audible click) which travels down the air column of a cylindrical source tube of internal radius 5 mm and then enters the object to be measured. The complicated object reflections are then picked up by a microphone in the side wall of the source tube and sampled by the computer at a sample rate of $F_s = 50,000$ Hz. This experiment is repeated 1000 times and the result averaged to increase the signal to noise ratio. Length l_2 is chosen so that the input pulse

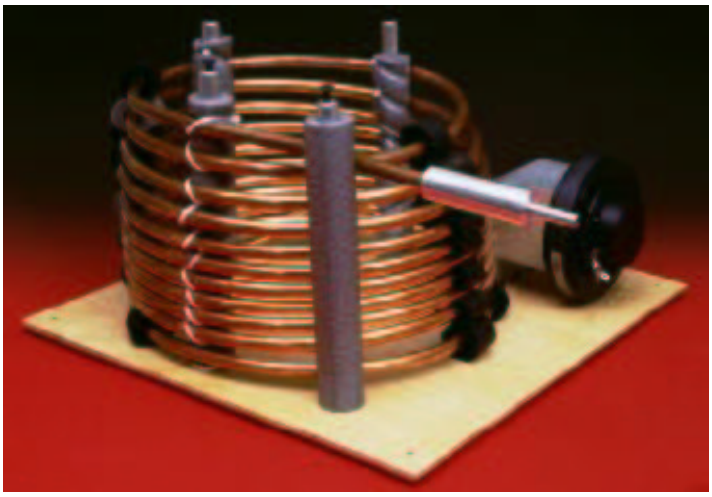

Figure 5.3: The acoustic pulse reflectometer

has completely passed the microphone before the first reflections return from the object. The length l_1 is ideally chosen so that the round trip time $t = c/(2l_1)$ is sufficient to record the full object reflections without interference from reflections from the source. This is of course dependent on the length of the instrument; longer instruments have reflections which carry on for more time meaning that a longer distance is required for l_1. The reflectometer used in this chapter has lengths $l_1 = 7.37$ m and $l_2 = 3.10$ m.

5.6 Experimental measurement of the input impulse response

Figure 5.4 shows the reflections measured at the microphone from a test object consisting of stepped cylinders. A schematic diagram of the stepped tube attached to the source tube is shown in figure 5.5. A coupler is attached to the source tube which contributes a 50 mm long section with a radius of 5 mm (the same as the source tube) to the bore of the object. The first section of the stepped tube object is 129 mm long with an internal radius of 6.25 mm and the second section is 177 mm long with an internal radius of 9.4 mm. At the end of the second section, the object is open, allowing sound to radiate.

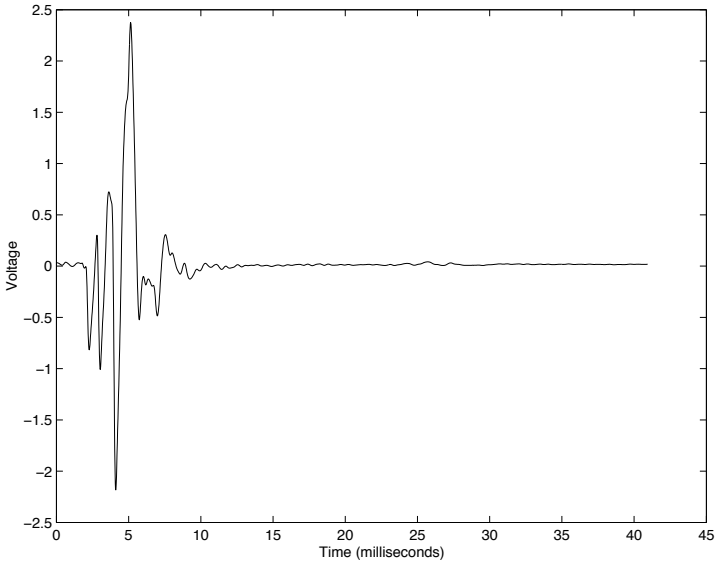

Figure 5.4: Object reflections

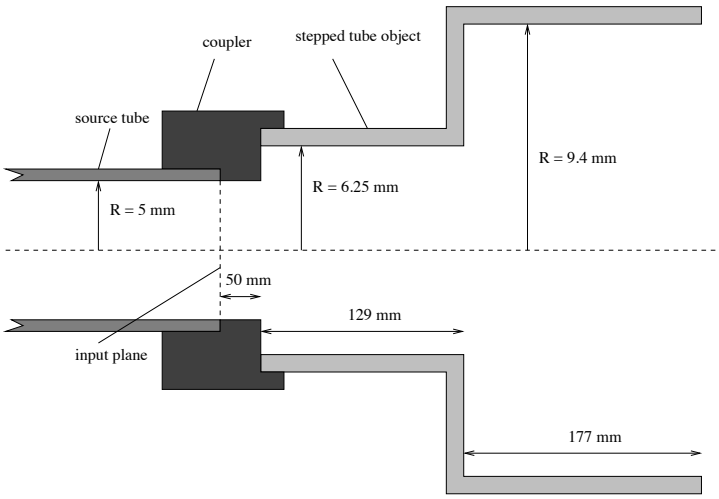

Figure 5.5: Stepped tube connected to source tube

The pressure signal can be understood as follows. Since the recording is triggered to start just before the reflections from the test object arrive at the microphone, the first few milliseconds consist only of background noise. There is no significant reflection of sound between the cylindrical source tube and the first section of the test object since the radii match. There is then a negative spike corresponding to the reflection of the input pulse from the expansion at the first step. The second negative spike corresponds to sound transmitted into the second section of test object, then reflected from the expansion at the second step before transmission to the microphone. The only sign change is due to the reflection from the expansion because transmission is always positive. The third negative spike is the component of the input pulse that is transmitted to the open end where it receives a negative reflection and is transmitted back to the microphone. These are the primary reflections, where the input pulse experiences only one

reflection process before reaching the microphone. The remaining parts of the recorded pressure signal are secondary reflections where the pulse experiences at least one reflection back down towards the open end before returning to the microphone.

5.6.1 Deconvolution

The input impulse response of a system is defined as the reflections resulting from excitation by an ideal acoustic impulse. The acoustic pulse that is produced experimentally is not an ideal impulse because of its finite duration. To get the input impulse response, we need to deconvolve the pulse entering the object's input from the reflections which return to the object's input. However, the measurement we make is of the object reflections when they have experienced losses corresponding to travel down the distance l_2 back to the microphone. By terminating the source tube in a flat plate or cap, we can give a 100% reflection of the input pulse down the same length of tube to the microphone. This measurement is referred to as the calibration pulse.

The input impulse response at the input plane is the deconvolution of the backward and forward going signals there. Our measurement records these signals once they have travelled an extra distance of l_2. In order to recover the signals present at the input plane we could apply the same loss filter to both. This corresponds to multiplying both by the same function in the frequency domain.

Since deconvolution is frequency domain division, the effect of the loss filter will be divided out. The input impulse response is therefore equal to the deconvolution of the signals measured at the microphone:

$$IIR(\omega) = \frac{R(\omega)I^*(\omega)}{I(\omega)I^*(\omega) + q} \tag{5.29}$$

where I is the Fourier transform of the calibration pressure pulse and R is the Fourier transform of the reflected pressure signal. q is a constraining factor used to prevent division by zero which would otherwise occur since the calibration pulse measurement consists only of background noise at high frequencies. In practice it low pass filters the input impulse response, removing high frequency noise. Choosing too large a value for q introduces errors into the deconvolution. For the current set up, $q = 0.00001$ was found to remove much of the high frequency noise, with a small change in q having no effect on the input impulse response within the bandwidth of our calibration pulse.

Figure 5.6 shows a measurement of the calibration pulse and figure 5.7 shows the input impulse response resulting from the deconvolution of the calibration pulse from the object reflections. The characteristic shape of the calibration pulse has been removed from the object reflections, making the individual reflections from the steps in the bore impulsive as is expected.

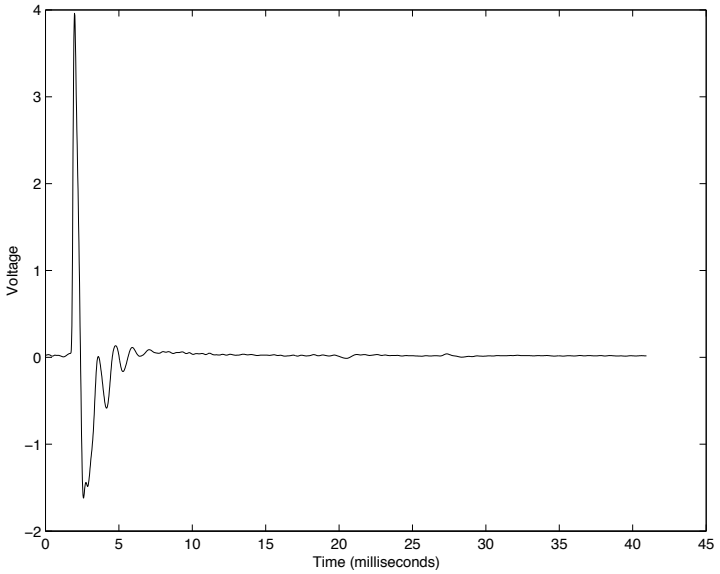

Figure 5.6: Calibration pulse

5.7 Experimental measurement of the input impedance

The input impedance of the stepped tube object was calculated from the measured input impulse response shown in figure 5.7 using equation (5.7). This result is shown in figure 5.8. Also shown is the test object consisting of stepped cylinders plotted against the multimodal theory results. These results were generated using the method described in chapter 4.

The agreement is very good between the plane wave calculation, the two mode calculation and the three mode calculation showing that the effect of higher modes is not significant in the frequency range we are considering. In fact, the lowest cut-

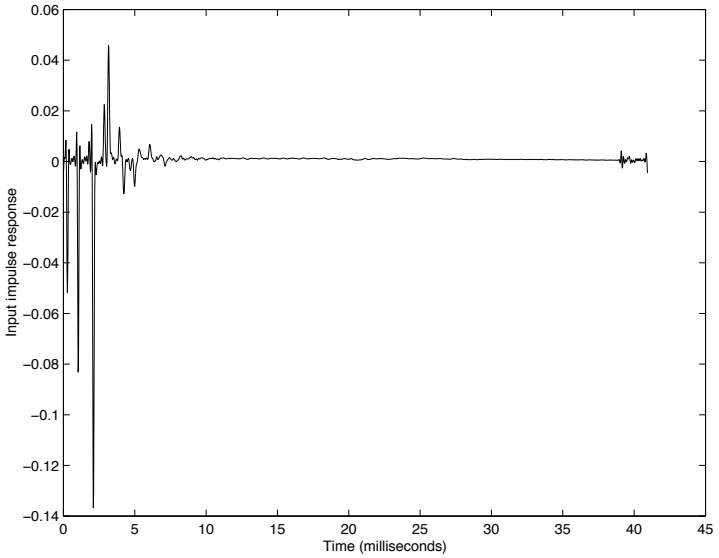

Figure 5.7: Input impulse response

off frequency is that belonging to the mode with one nodal circle in the wider of the two cylinders. This has a frequency of $f_c = c\gamma/(2\pi R) \approx 22$ kHz, considerably higher than the range of interest. The higher modes are therefore all strongly exponentially damped in the object and, similarly, very little mode conversion takes place at the discontinuities and at the open end.

The experimental and theoretical input impedance peaks agree best at low frequencies, with the deviation increasing as frequency is increased. In fact, the experimental peaks are at higher frequency than the theoretical peaks by a factor of 1.015 ± 0.005. A calculation of the musical pitch interval implied (see [1]) gives an answer of around 17 percent of a semitone. Notice that the theory assumes that the object is terminated in an infinite baffle and no baffle was used in the

experiment. The length correction at the open end for a baffled duct is slightly larger than the end correction for the unbaffled duct, hence the theoretical result (which assumes a flange) has lower frequency resonances than the experiment (which was on an unbaffled object). Still, the reasonable agreement between experiment and theory indicates that the resonance peaks are sufficiently well defined by the geometry of the object to ensure that the effect of small changes at the open end is minimal.

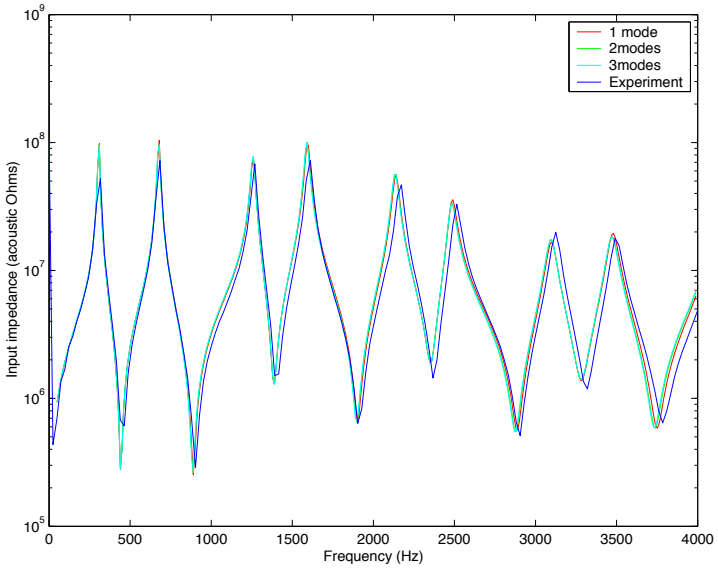

Figure 5.8: Stepped cylinder test object input impedance

Figure 5.9 shows the experimentally measured input impedance of the trumpet bell section described in section 4.3. The experimental data is plotted against the results of multimodal theory. Because the theory assumes that the object is terminated in an infinite baffle, in order for experimental results to verify the

accuracy of the theory, the experiment was performed with the trumpet section opening out onto a circular hole in a square hardboard baffle section of width 1 m. This time there is a significant drop in the sharpness and position of the higher frequency resonance peaks when more modes are included. The lowest cut-off frequency is the one nodal circle mode at the bell which has a frequency of $f_c = c\gamma/(2\pi R) \approx 3242$ Hz. All the modes are therefore still in cut-off throughout the frequency range of interest. The fact that there is a significant difference in the plane wave impedance depending on how many modes are included indicates that a significant amount of energy is lost by conversion of plane waves into the evanescent higher modes.

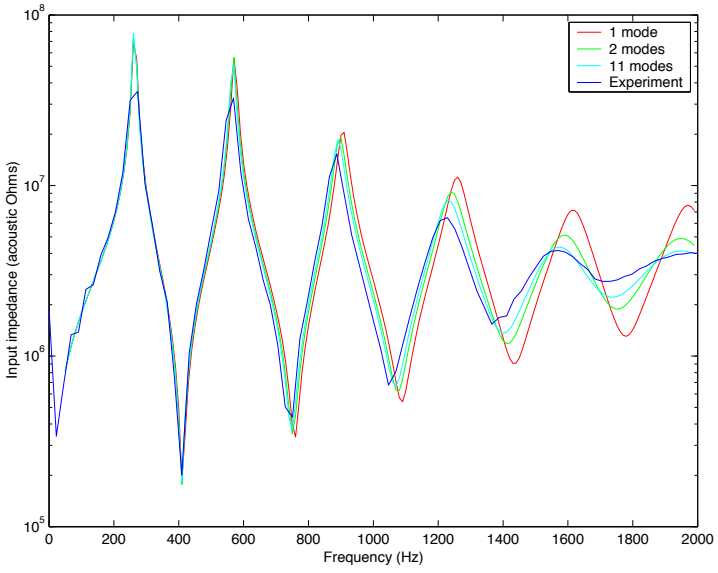

Figure 5.9: Trumpet section input impedance

5.8 DC offset

The bore reconstruction is very sensitive to the dc offset since a small constant positive value will be interpreted by the bore reconstruction algorithm as a small positive reflection coefficient. For this reason Sharp et al. [19] placed a 40.3 cm long cylindrical connector with a radius of 4.8 mm (here referred to as the dc tube) between the source tube and the object. There will be no reflected signal from the dc tube (because there are no expansions and contractions) and the object reflections will arrive at the microphone 2 ms later because of the round trip time taken to travel in the dc tube. The average value of the input impulse response within the first 2 ms range may be subtracted from the whole input impulse response, so removing the dc offset.

Figure 5.11 shows the reflections from the dc tube and stepped cylinder object. The reflections from the stepped cylinder object are preceded by the reflections from the join between the source tube and the dc tube. A schematic diagram of the test object attached to the source tube through the dc tube is shown in figure 5.10.

We can observe reflections from the stepped cylinder object are preceded by the reflections from the join between the source tube and the dc tube. This small reflection will also be present in the input impulse response. Ideally, this small bump in the internal profile would be perfectly reconstructed by the bore

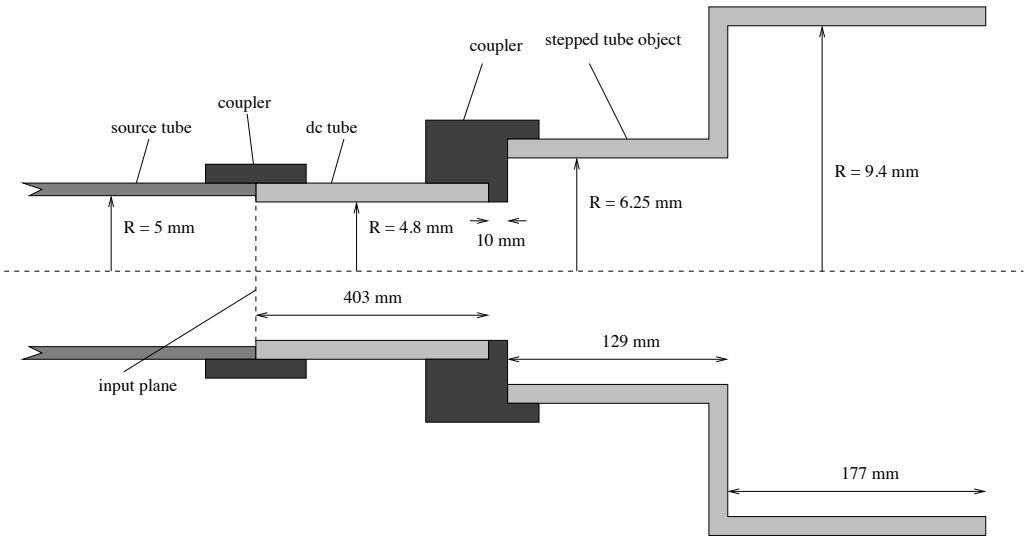

Figure 5.10: Stepped tube connected to source tube through dc tube

reconstruction algorithm. However, because the input impulse response is limited in frequency range, the impulsive reflection is spread out to make the pulse a small number of samples wide in the time domain. This means that the small leading edge occurs before the first sample. In accordance with signal processing theory, this small leading edge shows up in the last few samples in the time domain input impulse response. Errors result in the dc offset and bore reconstruction if this problem is ignored. The solution is to calculate the average value of the input impulse response between 1ms and 2ms and subtract this from the whole input impulse response. The response between 0ms and 1ms can then be replaced with zeros.

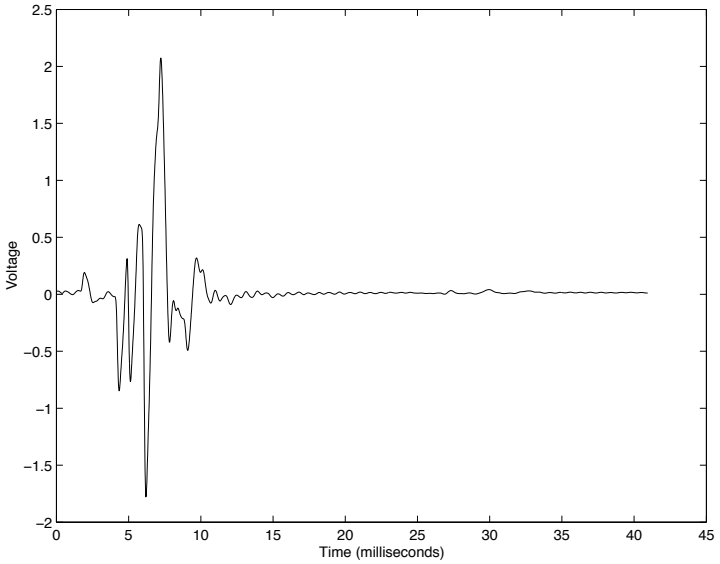

Figure 5.11: Object reflections using dc tube

5.9 Experimental measurement of the bore profile

Figure 5.12 shows the bore reconstruction of the test object consisting of stepped cylinders. The bore profile was calculated by putting the input impulse response from figure 5.7 into the lossy bore reconstruction algorithm developed by Amir et al. [17] as set out in section 5.4. Dotted lines show the radii of the cylindrical sections of the object. The first 40.3 cm of the bore reconstruction reproduces the cylindrical dc tube of radius 4.8 mm. The initial 0.17 m is perfectly flat because the input impulse response has been set to zero for the corresponding round trip travel time of 1ms and the next 0.26 m of the bore consists of the

remaining length of dc tube. Since no reflections occur within this section, the small changes in the bore reconstruction are due to background noise in the input impulse response.

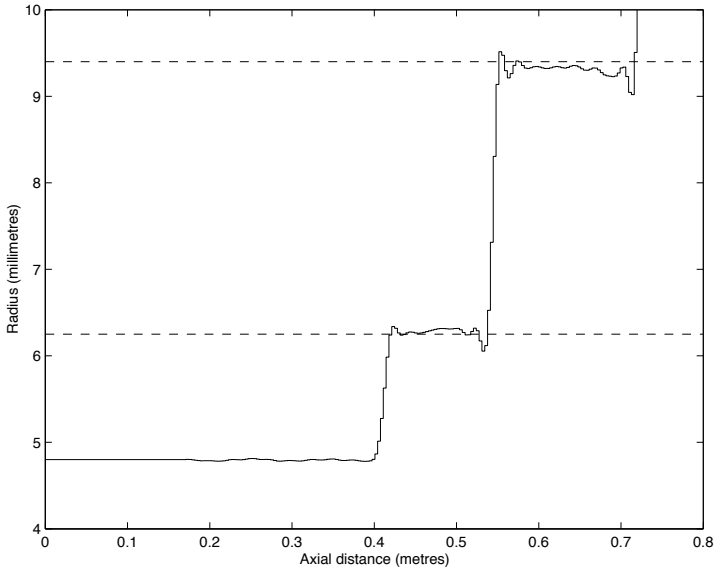

Figure 5.12: Reconstruction of test object consisting of stepped cylinders

The step up from the dc tube and coupler radius of 4.8 mm to the test object cylindrical section of radius of 6.25 mm is spread over a distance of 2 cm along the axis of the bore reconstruction when in reality the bore stepped up sharply. The reason for this spread is that the input impulse response measurement has a limited bandwidth; there were no significant components of the measured input impulse response above about 10 kHz because losses in the source tube damped out high frequency information in the pulse before it was able to enter the object under test. Removing the high frequencies in the impulsive reflection from a step

widens the pulse, hence the algorithm interprets the reflections as coming from a more gradual expansion. The behaviour is also an example of Gibb's phenomenon [6]. When a sharp step is represented as a set of frequency components, if the high frequencies are removed, the resulting step will be oscillatory such that the filtered version is too low on the lower side of the step and over shoots to be too high at the higher side [55] pp.601-603. This effect can be more clearly seen in the step from 6.25 mm to 9.4 mm. Here the over shoot and under-shoot in the bore reconstruction is about 0.3 mm.

Within the cylindrical sections, the bore reconstruction oscillates with an amplitude of less than 0.1 mm. The average value during each cylindrical section is accurate to 0.1 mm, with the largest error at the open end of the object. In the bore reconstruction algorithm, the cross-section at each point is worked out as a fraction of the cross-section at the previous point. Hence errors accumulate as the reconstruction continues. The object chosen for measurement was useful for a test of the accuracy of the technique.

Actual musical instruments tend to have more smoothly varying bores so preventing problems due to Gibb's phenomenon. The typical accuracy of 0.1 mm for short objects has recently been successfully used to aid a manufacturer to distinguish between different trumpet leadpipes [56].

The theory in this chapter all assumed plane wave propagation in the object under test. We will see in later examples that this means that the bore recon-

struction algorithm will produce errors in tubes with a large flare rate. In the following chapter we will go on to study the reflection of sound when multimodal effects are taken into account and consider how these effects might be included in a bore reconstruction algorithm.

Chapter 6

Multimodal reflections

6.1 Introduction

The reflectance is a quantity which gives the relative amplitudes of the forward and backward going waves at a particular place in an acoustic system. In the plane wave approximation it is a scalar ratio. For a simple discontinuity between two tubes, if the waves are incident from only one side, the reflectance does not vary with frequency. In general, however, the reflectance of an object is frequency dependent, equivalent to the frequency spectrum of the input impulse response.

In chapter 2 we presented a multimodal method of calculating the impedance throughout a tubular object provided the impedance at one end is known. Here we show how the impedance matrix can be used to derive the multimodal reflectance,

a matrix relating the amount of each mode reflected due to each mode incident. Because the non-planar modes always have frequency dependent impedances, the reflectance matrix will be frequency dependent, even for the special case of a plane wave incident from only one side. Theoretical results follow for this situation, showing both the frequency spectrum of the reflectance and the input impulse response obtained by performing an inverse Fourier transform on the reflectance.

In order to accurately reconstruct the bore of an instrument with a rapidly flaring bell, the effects of higher modes should be included. However, the layer peeling algorithm discussed in chapter 5 assumed plane wave propagation. This chapter concludes with a discussion of two possible solutions to this problem and the difficulties involved.

6.2 Multimodal reflectance matrix

A formula relating the forward and backward components of the volume velocity amplitude vector in terms of the impedance matrix was quoted in Pagneux et al. [32] p.2046. Here we show the derivation for the pressure amplitude vector. The first step is to express the total pressure amplitude vector $\mathbf{P}$ as the sum of the forward going ($\mathbf{P}_+$) and backward going ($\mathbf{P}_-$) components:

$$\mathbf{P} = \mathbf{P}_+ + \mathbf{P}_-. \tag{6.1}$$

Now the total volume velocity is expressed using the same notation for forward and backward components:

$$\mathbf{U} = \mathbf{U}_+ + \mathbf{U}_-. \tag{6.2}$$

Recalling the characteristic impedance of higher modes from equation (2.36), the ratio of the nth element in the forward going pressure vector to the nth element in the forward going volume velocity vector is $k\rho c/k_n S$. Using Z_c, the diagonal characteristic impedance matrix defined in equation (2.42):

$$\mathbf{U}_+ = Z_c^{-1}\mathbf{P}_+. \tag{6.3}$$

Similarly for the backward going waves,

$$\mathbf{U}_- = -Z_c^{-1}\mathbf{P}_-. \tag{6.4}$$

Defining the impedance matrix at a particular point as Z with $\mathbf{P} = Z\mathbf{U}$ we get

$$\mathbf{P}_+ + \mathbf{P}_- = ZZ_c^{-1}(\mathbf{P}_+ - \mathbf{P}_-) \tag{6.5}$$

which may be rearranged to give

$$(ZZ_c^{-1} + I)\mathbf{P}_- = (ZZ_c^{-1} - I)\mathbf{P}_+ \tag{6.6}$$

so the result is

$$\mathbf{P}_- = \mathcal{R}\mathbf{P}_+ \tag{6.7}$$

where $\mathcal{R}$ is the reflectance matrix:

$$\mathcal{R}(\omega) = \left(ZZ_c^{-1} + I\right)^{-1}\left(ZZ_c^{-1} - I\right). \tag{6.8}$$

Notice that this is a correction to the reflectance matrix quoted in [41]. The correction arises because $ABA^{-1} \neq B$ in general, even when A is a diagonal matrix. The correction only has an effect on the non-diagonal entries in $\mathcal{R}$. The graphs presented in [41] are of the $\mathcal{R}_{00}$ element and are unaffected by the correction.

6.3 Multimodal reflectance of a single discontinuity

The simplest case of a multimodal calculation of the reflectance matrix is for the reflection of plane waves from a single discontinuity in cross-section between two semi-infinite cylinders. We will define the plane on the left of the discontinuity as plane 1 and the plane on the right as plane 2 (see figure 2.2). If a plane sine-wave is incident from the left, it will be partially reflected and partially transmitted at the boundary. The impedance matrix on the right hand side of the boundary will

be equal to the characteristic impedance matrix because only forward propagating waves are present there:

$$Z^{(2)} = Z_c^{(2)} \tag{6.9}$$

where $Z_c^{(2)}$ is simply the characteristic impedance matrix defined in equation (2.42) when $S = S_2$. This matrix can then be projected to get the impedance matrix on the left by substitution into equation (2.97):

$$Z^{(1)} = F Z_c^{(2)} F^{\mathrm{T}}. \tag{6.10}$$

The reflectance matrix at surface 1 can then be found from equation (6.8) by substituting in $Z = Z^{(1)}$ from equation (6.10), also noting that $Z_c = Z_c^{(1)}$ is the characteristic impedance matrix on surface 1 with $S = S_1$:

$$\mathcal{R}(\omega) = \left(F Z_c^{(2)} F^{\mathrm{T}} \left(Z_c^{(1)} \right)^{-1} + I \right)^{-1} \left(F Z_c^{(2)} F^{\mathrm{T}} \left(Z_c^{(1)} \right)^{-1} - I \right). \tag{6.11}$$

If particular values of the cylinder radii, R_1 and R_2 are chosen, the reflectance matrix can be calculated for a number of frequency values. However, as with the radiation impedance calculations in chapter 3, the results may be presented in a form valid for all radius values by reformulating the equations in terms of the dimensionless frequency variable kR_1 and the radius ratio $\beta = R_1/R_2$. The characteristic impedance of the nth mode on the left of the discontinuity becomes $Z_c^{(1)} = (kR_1\rho c)/(k_n R_1 S_1)$ where $k_n R_1 = \pm\sqrt{(kR_1)^2 - \gamma_n^2}$. Dividing by

$\rho c/S_1$ normalises the characteristic impedance of the nth mode to give

$$C_n^{(1)}(kR_1) = \frac{S_1}{\rho c} Z_c^{(1)} = \frac{kR_1}{\pm\sqrt{(kR_1)^2 - \gamma_n^2}} \tag{6.12}$$

Similarly, the normalised characteristic impedance of the nth mode on surface 2 is

$$C_n^{(2)}(kR_1, \beta) = \frac{S_2}{\rho c} Z_c^{(2)} = \frac{kR_1/\beta}{\pm\sqrt{(kR_1/\beta)^2 - \gamma_n^2}} \tag{6.13}$$

using $kR_2 = kR_1/\beta$. The reflectance matrix is then

$$\mathcal{R} = \left(\beta^2 \left(FC^{(2)}F^{\mathrm{T}}\right)\left(C^{(1)}\right)^{-1} + I\right)^{-1} \left(\beta^2 \left(FC^{(2)}F^{\mathrm{T}}\right)\left(C^{(1)}\right)^{-1} - I\right) \tag{6.14}$$

where $C^{(1)}$ and $C^{(2)}$ are diagonal matrices with the entries on the nth diagonals given by equations (6.12) and (6.13) respectively. The reflectance is now a function of the dimensionless variables kR_1 and β only.

Before proceeding to produce graphs from the reflectance matrix we should consider which elements determine the reflected sound. For our example we have a plane sine-wave of unit amplitude incident on the discontinuity from the left.

This forward travelling wave is represented by

$$\mathbf{P}_+ = \begin{pmatrix} 1 \\ 0 \\ 0 \\ 0 \\ \vdots \end{pmatrix}. \tag{6.15}$$

From equation (6.7) the reflection is then

$$\mathbf{P}_- = \mathcal{R}\mathbf{P}_+ = \begin{pmatrix} \mathcal{R}_{00} \\ \mathcal{R}_{10} \\ \mathcal{R}_{20} \\ \mathcal{R}_{30} \\ \vdots \end{pmatrix}. \tag{6.16}$$

The plane wave component of the reflection is therefore simply given by the corner value of the reflectance matrix, $\mathcal{R}_{00}$. We will refer to the $\mathcal{R}_{00}$ value as the plane reflectance. Although we will discuss only the plane reflection from an incident plane wave, it is important to note that we are doing a multimodal calculation. Depending on the frequency, some of the incident energy is converted into the other modes. In turn the plane reflectance will vary with frequency.

Figure 6.1 displays the absolute value of the plane reflectance for radius ratio

of $R_1/R_2 = 0.5$ against the dimensionless frequency variable, kR_1 as a green line. At low frequencies the plane reflectance matches the plane wave reflection coefficient of equation (2.20) which is -0.6 for $R_1/R_2 = 0.5$. The maximum in the graph corresponds to the cut-off of the first non-plane mode in the larger of the ducts. A blue line shows the absolute value of the plane reflectance from the inductance method published by Kergomard and Garcia [57]. The use of the inductance method to calculate reflectance is summarised in appendix C. The inductance method is designed to be accurate in the region $kR_2 < 3.5$, ie. $kR_1 < 1.75$ in this example. Agreement between the inductance method and the current multimodal method is very good in this region.

Figure 6.2 shows the plane reflectance decaying to zero at high frequencies. We can understand this by noting that high frequencies do not experience much diffraction meaning almost 100% of the energy is transmitted across an expansion.

Figure 6.3 shows the plane reflectance against frequency for a number of different radius ratios. The low frequency limit shows that large cross-section changes reflect more energy in agreement with the plane wave approximation reflection coefficient. Large cross-section changes also lead to a quicker drop off of plane reflectance with frequency. The detail in the graphs can be understood by considering the cut-off frequencies in the smaller pipe (section 1) and the larger pipe (section 2). The cut-off wavenumber for the $n = 1$ mode in section 1 is $kR_1 \approx 3.83$ and the $n = 2$ cut-off in section 1 is $kR_1 \approx 7.02$. We can see all the graphs have

small minima at these values. The large peaks, however, are due to the cut-off frequencies in the pipe on the right.

In order to show the cut-off frequencies on surface 2, the graphs are replotted using a dimensionless frequency variable of $kR_2 = kR_1 \times R_2/R_1$. The resulting plot is shown in figure 6.4. The lowest cut-off wavenumber present is for the $n = 1$ mode in section 2 with a dimensionless frequency of $kR_2 \approx 3.83$. All the spectra show peaks at this point because above this frequency energy is absorbed from the plane reflection by transmission into the propagating mode. The reduction in reflected amplitude after the $n = 1$ cut-off frequency is particularly marked in the $R_1/R_2 = 0.5$ case. The pressure profile of the $n = 1$ mode on S_2 has a circular amplitude maximum in the centre taking up an area similar to the pressure amplitude of the plane mode on S_1. Since the pressure profile on S_2 must match the pressure profile on S_1, above the cut-off frequency strong transmission of the propagating $n = 1$ mode is favoured. The $n = 2$ mode in section 2 is responsible for the peaks at $kR_2 \approx 7.02$ in the plane reflectance spectra.

6.4 Multimodal input impulse response

Now we will use an inverse Fourier transform of the plane reflectance to give the plane component of the input impulse response of our simple discontinuity between cylindrical pipes. A similar calculation was performed by Boone et al.

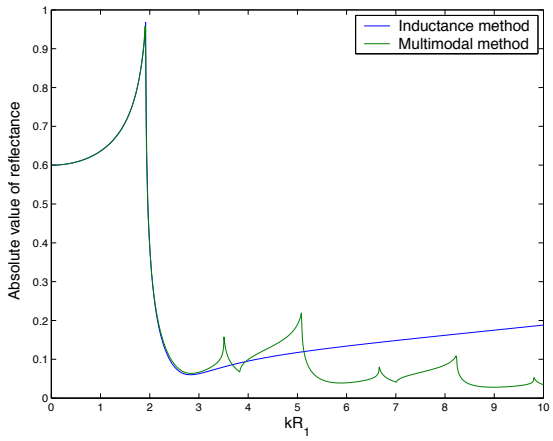

Figure 6.1: Plane reflectance for a single discontinuity with $R_1/R_2 = 0.5$

[58] for the input impulse response of a lightly damped rectangular cavity. In order to work out the inverse Fourier transform we need to calculate the reflectance for a number of equally spaced frequencies. The zero frequency component cannot be worked out with the present multimodal method because $k = 0$ means that Z_c^{-1} has elements which go to infinity. It may, however, be noted that the plane reflectance tends to the plane wave approximation reflection coefficient at low frequency, so the $k = 0$ plane reflectance is taken from equation (2.20) in what follows.

When the Fourier transform of a real signal is performed the result is a conjugate symmetric spectrum. That is, the real part of the spectrum is symmetric and the imaginary part anti-symmetric. The point of symmetry is called the Nyquist frequency, and has a value half that of the sample frequency. We require that

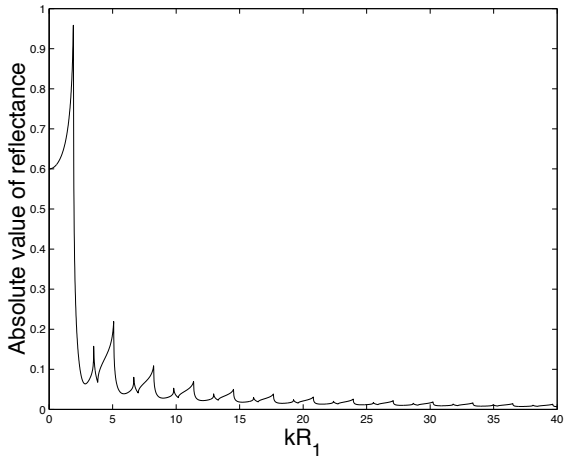

Figure 6.2: Plane reflectance for a single discontinuity with $R_1/R_2 = 0.5$ showing high frequency behaviour

there are no significant components in the signal above the Nyquist frequency to prevent numerical errors due to aliasing. Similarly, when we calculate an inverse Fourier transform, we require that the spectrum decays to zero by the Nyquist frequency. From figure 6.2 we note that if we go to very high frequencies the plane reflectance does indeed decay to zero, meaning that numerical problems may be avoided if the Nyquist frequency chosen is high enough. The vector of the plane reflectance must then be made conjugate symmetric for the inverse Fourier transform to be calculated [59].

The result of an inverse Fourier transform of the plane reflectance is shown in figure 6.5 for a radius ratio of R_1/R_2. Progressively higher values for the Nyquist frequency in the calculation of the plane reflectance were taken until the inverse transform showed convergence on a final answer. The appearance of

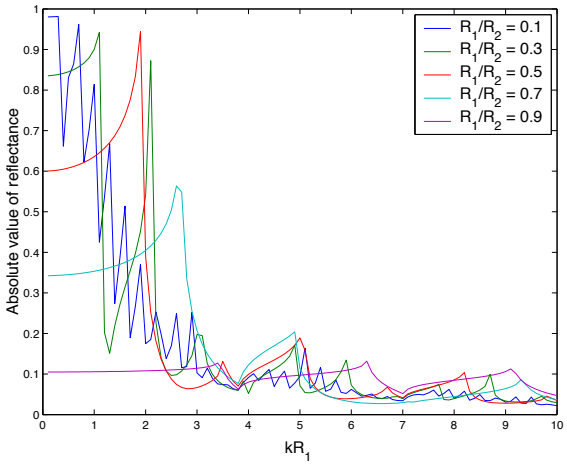

Figure 6.3: Plane reflection spectrum for different discontinuity ratios against kR_1

the time response is that of a negative pulse. This is to be expected as we are calculating the reflection of an impulse from a expansion which has a negative reflection coefficient. The finite width of the pulse shows how the high frequency components have been removed and the oscillations in the time domain response correspond to the peak in the plane reflectance due to the lowest frequency cut-off.

The results presented so far are for scattering from a junction between two infinite pipes. In order to treat physically realisable systems we want to have a method of calculating the input impulse response of any musical instrument approximated by a series of cylinders. This is achievable by first calculating the input impedance matrix by the multimodal method described in section 2.6. The reflectance matrix can then be found using equation (6.8). The plane wave component of the input impulse response can be calculated by taking the inverse Fourier transform of the plane reflectance in the same manner as in section 6.4. It

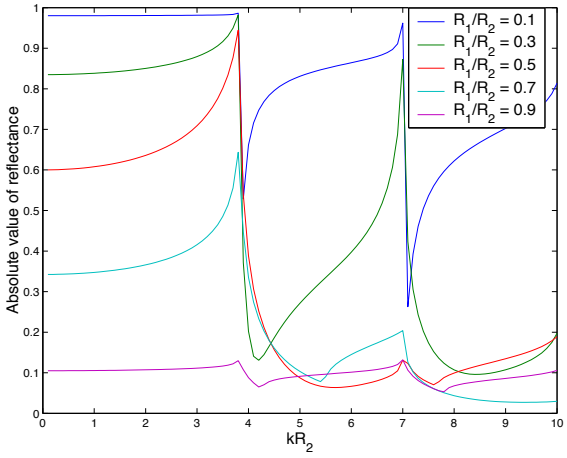

Figure 6.4: Plane reflection spectrum for different discontinuity ratios against kR_2

should be noted that this method involves calculating the multimodal radiation impedance; this can be readily done if the instrument is assumed to have an infinite baffle termination. It is logical that the input impulse response should not depend on the radiation impedance for the first $t = 2L/c$ seconds taken for sound to reflect from the radiating end and arrive back at the input where L is the length of the instrument.

6.5 Issues in multimodal bore reconstruction

Now we will discuss possible approaches to the inclusion of multimodal calculations in acoustic pulse reflectometry bore reconstruction. This procedure has yet to be implemented because of the difficulties arising from the frequency dependent reflections and the additional computation power required for computing

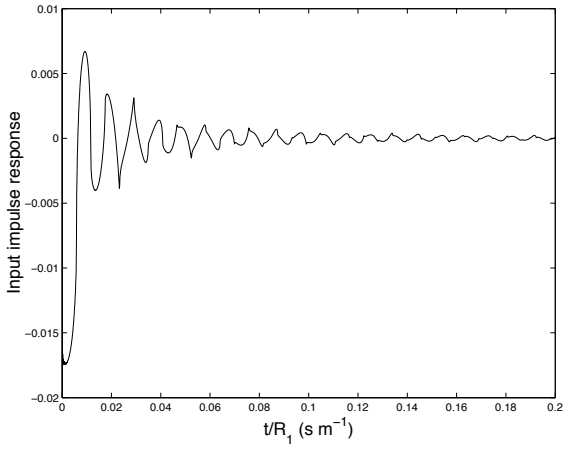

Figure 6.5: Plane input impulse response calculated for a single discontinuity with $R_1/R_2 = 0.5$

multimodal behaviour in an already computationally expensive procedure. This section therefore is a review of the theoretical background on which future work may be based, and a discussion of the problems and possible solutions. To start, it is useful to present a brief summary of the plane wave approximation algorithm set out in chapter 5.

In an acoustic pulse reflectometry measurement the first step is the experimental measurement of the input impulse response. If a forward going ideal impulse enters the input, by definition the reflections are the input impulse response sequence. We therefore know both the forward and backward going waves at the input. The plane reflection coefficient of equation (2.20) gives the amplitude of the primary reflection of an incident wave in terms of the change in cross-section. The plane reflection coefficient (and therefore the change in cross-section) are

found from the the ratio of the first entries in the forward and backward going pressure vectors respectively, since they correspond to a primary reflection.

Scattering equations are then used to find the forward and backward going waves in the next cylindrical section. This process is then repeated, working out the forward and backward going waves and the change in bore at each step along the bore in turn untill the output end is reached. The scattering equations used are equations (5.11), (5.17) and (5.18):

$$\begin{pmatrix} p_+^{(2)}[nT] \\ p_-^{(2)}[nT] \end{pmatrix} = \frac{1}{1-r_{1,2}} \begin{pmatrix} 1 & -r_{1,2} \\ -r_{1,2} & 1 \end{pmatrix} \begin{pmatrix} p_+^{(1)}[nT] \\ p_-^{(1)}[nT] \end{pmatrix}. \tag{6.17}$$

$$p_+^{(3)}\left[\left(n+\frac{1}{2}\right)T\right] = p_+^{(2)}[nT]. \tag{6.18}$$

$$p_-^{(3)}\left[\left(n-\frac{1}{2}\right)T\right] = p_-^{(2)}[nT]. \tag{6.19}$$

Here surfaces 1 and 2 are on the left and right of the initial discontinuity respectively and section 3 is a distance $cT/2$ to the right of surface 2 (see figure 5.1).

For a multimodal theory, the reflection coefficient is frequency dependent, meaning that the primary reflection of an impulse from the first step is not impulsive, but is spread out over a finite time. Ideally, the primary reflections then should not simply be calculated from the ratio of the first time step in the forward and backward going pressure vectors. A rigorous analysis should look at the plane

reflectance, the frequency spectrum of the impulse response of the step in the absence of secondary reflections. As with figure 6.4 the plane wave approximation reflection coefficient corresponding to the cross-section change would then be equal to the low frequency limiting behaviour of this plane reflectance. The problem with this is that the secondary reflections are present in the input impulse response and are as yet unknown; after the first time step the primary reflection from the first cross-section change is swamped by information about the rest of the instrument.

Further investigation is necessary to see if the plane wave approximation reflection coefficient from the first time step of the primary reflection can give accurate enough results. The bore reconstruction algorithm may still incorporate multimodal effects by the use of a multimodal scattering equation. While the first change in cross-section would be calculated without multimodal effects, the forward and backward going waves on the other side of the step would be calculated including the loss of energy to higher modes. The value of the primary reflection from the next step would therefore be effected by the multimodal treatment.

6.5.1 Multimodal scattering matrix

In sections 6.3 and 6.4 we performed multimodal scattering from a discontinuity for an example in which there was no backward going wave on the right hand side. In order to create the multimodal version of our scattering equation (6.17),

we must drop this assumption and express the pressure and volume velocity as the sum of forward and backward going waves on both sides. The aim then is to start with the known forward going and backward going waves at the input to a discontinuity (ie. from an experimentally measured input impulse response), and calculate the forward and backward going waves on the other side of the discontinuity. This method was suggested by van Walstijn [60].

We will denote the forward going pressures on surface 1 and surface 2 respectively as $\mathbf{P}_{+}^{(1)}$ and $\mathbf{P}_{+}^{(2)}$. The backward going pressure on surface 1 and surface 2 respectively will be $\mathbf{P}_{-}^{(1)}$ and $\mathbf{P}_{-}^{(2)}$. Again the surfaces are as shown in figure 5.1. Using the pressure projection equation (2.79) we get:

$$\left(\mathbf{P}_{+}^{(1)} + \mathbf{P}_{-}^{(1)}\right) = F\left(\mathbf{P}_{+}^{(2)} - \mathbf{P}_{-}^{(2)}\right), \qquad S_1 < S_2. \tag{6.20}$$

Putting equations (6.3) and (6.4) into the volume velocity projection equation (2.83) gives:

$$\left(Z_c^{(2)}\right)^{-1}\left(\mathbf{P}_{+}^{(2)} - \mathbf{P}_{-}^{(2)}\right) = F^{\mathrm{T}}\left(Z_c^{(1)}\right)^{-1}\left(\mathbf{P}_{+}^{(1)} - \mathbf{P}_{-}^{(1)}\right), \qquad S_1 < S_2 \tag{6.21}$$

These two simultaneous equations can be solved by eliminating $\mathbf{P}_{-}^{(2)}$ to give

$$\mathbf{P}_{+}^{(2)} = \frac{1}{2}\left(Z_c^{(2)} F^{\mathrm{T}} \left(Z_c^{(1)}\right)^{-1} + F^{-1}\right)\mathbf{P}_{+}^{(1)} + \frac{1}{2}\left(Z_c^{(2)} F^{\mathrm{T}} \left(Z_c^{(1)}\right)^{-1} - F^{-1}\right)\mathbf{P}_{-}^{(1)}. \tag{6.22}$$

Eliminating $\mathbf{P}_{+}^{(2)}$ in the simultaneous equations gives

$$\mathbf{P}_{-}^{(2)} = -\frac{1}{2}\left(Z_c^{(2)} F^{\mathrm{T}} \left(Z_c^{(1)}\right)^{-1} - F^{-1}\right)\mathbf{P}_{+}^{(1)} + \frac{1}{2}\left(Z_c^{(2)} F^{\mathrm{T}} \left(Z_c^{(1)}\right)^{-1} + F^{-1}\right)\mathbf{P}_{-}^{(1)}. \tag{6.23}$$

It is possible to express both equations (6.22) and (6.23) in one equation. This is done by making column vectors consisting of the forward going and backward going pressure vectors end to end. If the vectors $\mathbf{P}_{+}^{(2)}$ and $\mathbf{P}_{-}^{(2)}$ are each truncated to have N elements, the resulting end to end vector will have a length of $2N$ elements. This is then set equal to a single scattering matrix with $2N \times 2N$ elements multiplied by a vector of length $2N$ consisting of the pressure vectors $\mathbf{P}_{+}^{(1)}$ and $\mathbf{P}_{-}^{(1)}$ placed end to end. The first N columns in our scattering matrix then come from the coefficients of $\mathbf{P}_{+}^{(1)}$ in the previous equations and the second N columns from the coefficients for $\mathbf{P}_{-}^{(1)}$. The resulting equation is

$$\begin{pmatrix} \mathbf{P}_{+}^{(2)} \\ \mathbf{P}_{-}^{(2)} \end{pmatrix} = \begin{pmatrix} \mathcal{E} & \mathcal{F} \\ -\mathcal{F} & \mathcal{E} \end{pmatrix} \begin{pmatrix} \mathbf{P}_{+}^{(1)} \\ \mathbf{P}_{-}^{(1)} \end{pmatrix} \tag{6.24}$$

where $\mathcal{E}$ is an $N \times N$ matrix given by

$$\mathcal{E} = \frac{1}{2}\left(Z_c^{(2)} F^{\mathrm{T}} \left(Z_c^{(1)}\right)^{-1} + F^{-1}\right) \tag{6.25}$$

and $\mathcal{F}$ is an $N \times N$ matrix given by

$$\mathcal{F} = \frac{1}{2}\left(Z_c^{(2)} F^{\mathrm{T}} \left(Z_c^{(1)}\right)^{-1} - F^{-1}\right). \tag{6.26}$$

Notice that if there is no backward going wave in section 2, then $\mathbf{P}_-^{(2)} = 0$, and from equation (6.24), $\mathbf{P}_-^{(1)} = \mathcal{E}^{-1}\mathcal{F}\mathbf{P}_+^{(1)}$ which agrees with the results of section 6.3.

Each of the elements in equation (6.24) is frequency dependent so we must compute the scattering matrix for each frequency in the Fourier transform of the pressure signals and perform the matrix multiplication in the frequency domain. This method means a significant increase in the computational load. Only a small number of modes could be added for this method of bore reconstruction to be feasible.

In addition to scattering across discontinuities, scattering along cylindrical sections is also necessary. We will therefore require multimodal versions of equations (6.18) and (6.19) which give the pressure value at surface 3 from the pressure value at surface 2 in figure 5.1. The modes propagate independently between these surfaces because the cross-section remains constant. For a given frequency

of sound, the wavelength along the axis of the duct depends on the mode under consideration, with higher order modes having longer wavelengths untill at high enough mode numbers the waves are exponentially damped. This means the pressure is not just delayed by travel along the pipe, it also experiences dispersion.

The dispersion is described in the time domain by Morse and Ingard [22] p.498. Firstly, below cut-off the $n \geq 1$ modes are exponentially damped meaning that the low frequencies are filtered out. Above cut-off, the phase velocity is larger than c and the group velocity is smaller than c, with both converging on c in the high frequency limit. The time domain impulse transfer function for a higher mode pressure distribution is calculated by Fourier transform to give an impulse travelling at the speed of sound c with a wake trailing behind. Physically this is realistic since an impulse contains all frequency components, with the very high frequencies responsible for the sharp impulse travelling with a group velocity of c and the lower frequency components following behind.

Using this impulse transfer function for time domain convolution with the forward and backward going pressure vectors is a possible solution for scattering down a cylindrical section. Alternatively, frequency domain multiplication can be used. The pressure amplitude of the nth higher mode in a uniform pipe is described in equation (2.33). Projecting the forward going part gives

$$P_+^{(3)} = e^{-ik_n d} P_+^{(2)} \tag{6.27}$$

and the backward going part gives

$$P_{-}^{(3)} = e^{ik_n d} P_{-}^{(2)}. \tag{6.28}$$

6.5.2 Iteration method with multimodal control

We have shown how including higher modes within a layer peeling bore reconstruction algorithm may be possible and have highlighted the problems which must be addressed before it is achieved. It is also worthwhile presenting an alternative way of including multimodal effects in reconstructing the bore. This section discusses how a multimodal calculation of the input impulse response may provide the control for an iteration procedure designed to arrive at the correct bore.

Iterative bore reconstruction has been studied by Kausel [61] for the case of deducing the bore from measured input impedance. As a starting point, a fairly arbitrary starting bore was chosen and the iteration procedure used to minimise the difference between a plane wave calculation of the input impedance of the bore and that which was measured. We will refer to the result as the "plane wave equivalent bore" since it is the bore whose input impedance, according to the plane wave approximation, would match that which was measured experimentally.

Our aim is to find a bore where the multimodal method calculation of some

acoustic variable matches that which was measured experimentally. We do not know the multimodal open end condition without assuming an infinite baffle so it may be helpful to use the time domain response as a control for iteration. This does not depend on the choice of end condition until the primary reflections from the open end arrive. Our starting point is to calculate the plane approximation bore reconstruction from the measured input impulse response. This is also a "plane wave equivalent bore."

In the experimental impulse response measurement some energy was lost to the non-planar modes within the instrument. The measured reflected amplitudes are therefore smaller than we would expect from plane wave approximation scattering. A slight under-prediction of the cross-section changes within the real instrument is therefore expected in a plane wave equivalent bore.

The impulse response of the plane wave equivalent bore may then be calculated by the multimodal method. This calculation will not match the experimentally measured input impulse response. Firstly, we expect the amplitude of the reflections to be reduced because the plane wave equivalent bore slightly under-predicts the cross-section changes within the real instrument. Secondly, as mentioned before, the correct radiation impedance is not known. We must assume that the instrument is terminated in an infinite baffle, so the impulse responses may differ slightly after the primary reflection from the open end returns to the input.

By comparing the impulse response of the plane wave equivalent bore with

that measured experimentally, we have information on how the reconstructed bore needs to be changed to bring it in line with the experimental results. An iteration procedure could be used where we modify the reconstructed bore, calculate the impulse response including higher modes, compare the result with experiment and continue. The final result would be achieved when the difference between the multimodal calculation of the impulse response of the bore profile and the experimental impulse response is minimised. Obviously, the information in the impulse response after the primary reflection from the end condition would not be used in such a procedure because of the end condition problem.

In order to provide a guide for how the bore reconstruction deviates from the actual bore, the difference between the measured input impulse response and the calculated input impulse response of the bore reconstruction could be fed into the reconstruction algorithm. This would return an almost cylindrical bore which expands at points along the bore where the reconstruction is under-predicting and contracts where the bore is over-predicting. The iteration procedure should then proceed quickly towards a final answer.

The iteration procedure may be too computationally taxing if every point in the bore is varied separately by the iteration procedure. The bore profile could instead be represented by a polynomial fit to a number of points along the bore. This gives a number of degrees of freedom which can be changed by the iteration procedure before their effect on the response is calculated. In general, convergence

will be faster if the number of degrees of freedom is reduced. Too low a number of degrees of freedom however will mean any improvement due to the modelling of multimodal effects will be counteracted by over simplification of the bore. Since a multimodal calculation must be performed at each step of the procedure, the computational power required would be large.

Chapter 7

Improvements to pulse reflectometry

7.1 Introduction

In this chapter refinements to pulse reflectometry are presented. First we remove the need for a dc tube between the source tube and the instrument under test. The main improvement this provides is a greater level of convenience but the elimination of the inevitable small discontinuity between the source tube and dc tube is another benefit. Next we show changes which increase the length of the time window in which the object reflections can be measured, allowing the measurement of longer instruments. Using a longer source tube means that there is more time to sample the object reflections before they suffer interference from

the source reflections. A post-processing method for source reflection cancellation is also presented.

All experiments presented so far use a pulse-like excitation signal. The obvious advantage of this is to minimise the processing which must be done to determine the input impulse response. However, the corresponding disadvantage is that we are limiting the amount of energy input into the system. This chapter therefore also includes the use of pseudo-random noise signals called maximum length sequences (MLS) in pulse reflectometry. These signals share many properties with white noise, but one significant difference is that the phase response of the system can be extracted in addition to the frequency response.

7.2 The virtual DC tube method

Physically, having a dc tube between the source tube and object under test is inconvenient. Also the join between source tube and dc tube will not be perfectly smooth, so a small reflection will be present at the start of the input impulse response. As discussed in section 5.8 the result is that only half of the available two milliseconds in the input impulse response data is used in the dc offset calculation. As an alternative we present a new method described as the virtual dc tube method [62]. The effect of the dc tube is simulated by starting recording the reflections from the object under test 2ms earlier, using a digital filter (see section

5.4.2) to add the losses that would have occurred if the sound had travelled across a dc tube.

In effect, the last 40cm of the source tube has been turned into a virtual dc tube, perfectly joined onto the source tube. Notice how about 2ms into the dc tube method reflections in figure 5.11 there was a small reflection from the join between the source tube and the dc tube. The object reflections measured using the virtual dc tube method from figure 7.1 show that the problem has been avoided entirely.

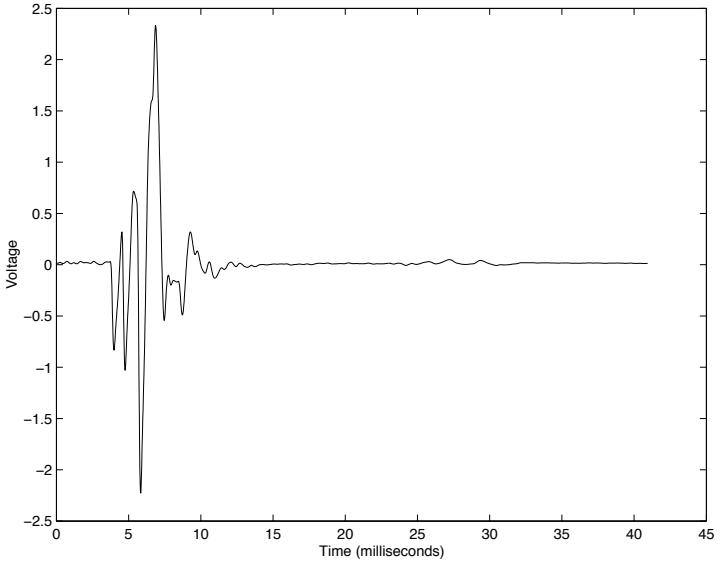

Figure 7.1: Object reflections using virtual dc tube

A bore reconstruction achieved using the virtual dc tube method is shown in figure 7.2. The reconstruction is much the same as that achieved using the dc tube method (see figure 5.12) except that the small error of about 0.1mm in the

average value of the radius of the last cylindrical section is absent in the new method. Because the frequency bandwidth of the measurement is not altered, the oscillations at the changes of cross-section and at the open end are of the same size irrespective of whether the virtual dc tube method is used.

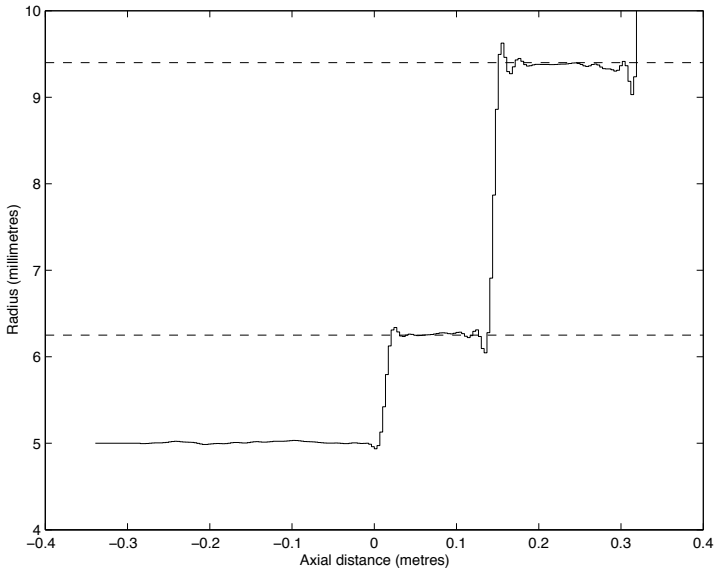

Figure 7.2: Reconstruction of test object consisting of stepped cylinders

7.3 Measuring longer objects

If the leading edge of the object reflections undergoes a further reflection from the loudspeaker and returns to the microphone before the original trailing edge arrives, then the measurement of the object reflections will be disturbed. For this reason the measurements presented so far have a time length of $2l_1/c = 2 \times 7.37/343 = 0.043$secs where l_1 is the length of source tube between the mi-

crophone and the source (see figure 5.2). The length of instrument that can be measured must be less then $2l_1$ since the primary reflections from the end of such an instrument would arrive at the end of our time window simultaneously with the source reflections. It is not realistic to expect that such a limit will be approached in practice, however, since we would lose the secondary reflections from the object which carry on after the last primary reflection has arrived. In practice the maximum length measurable depends both on l_1 and the radius of the object in question since long sections of large radius will mean low losses and many secondary reflections will return before all of the reflection sequence is finished.

Increasing l_1 will mean that the source reflections will arrive later and the measurement time window will be longer. The aim of this section is to measure long objects so we will therefore use a reflectometer with $l_1 = 9.68$m rather than the 7.37m used up to now. This option is not without its drawbacks. Firstly, since the losses in the source tube reduce all frequency components, a higher amplitude of sound must be input in order to preserve the signal to noise ratio on sampling the reflections. This is easily achieved by turning up the volume on the audio amplifier used in pulse production, although when taken to extremes this could damage the amplifier and speaker or cause non-linear sound propagation not accounted for in the analysis. Also, the high frequencies are attenuated proportionally more than the low frequencies meaning that the further a pulse travels, the wider it gets. The source tube section l_2 must therefore also be

lengthened to allow the longer input pulse to completely pass the microphone before the object reflections arrive. For the reflectometer in this section $l_2 =$ 6.52m was chosen (3.10m was used previously).

7.3.1 Source reflection cancellation method

The increase of the length of the source tube to measure longer objects is clearly limited by the resulting larger losses in the source tube. Since the aim is to isolate the backward going object reflections from the waves going forward from the source, the use of multiple microphones is a possible technique. This has been attempted by Louis et al. [63]. Active real-time cancellation of the source reflections has also been attempted by Sharp [64] with limited success. Here we discuss a method of cancelling the source reflections by post-processing [62].

We define the backward travelling calibration pulse as I_i. This is shown in the first 40ms of figure 7.3. The last 40ms of figure 7.3 shows the forward going reflections of the calibration pulse from the source which we will refer to as I_j. The filter H representing the source reflection function can be derived from these signals by deconvolution:

$$H(\omega) = \frac{I_j(\omega)I_i^*(\omega)}{I_i(\omega)I_i^*(\omega) + q}. \tag{7.1}$$

Now consider the reflections from a extended object. We define R_i as the first

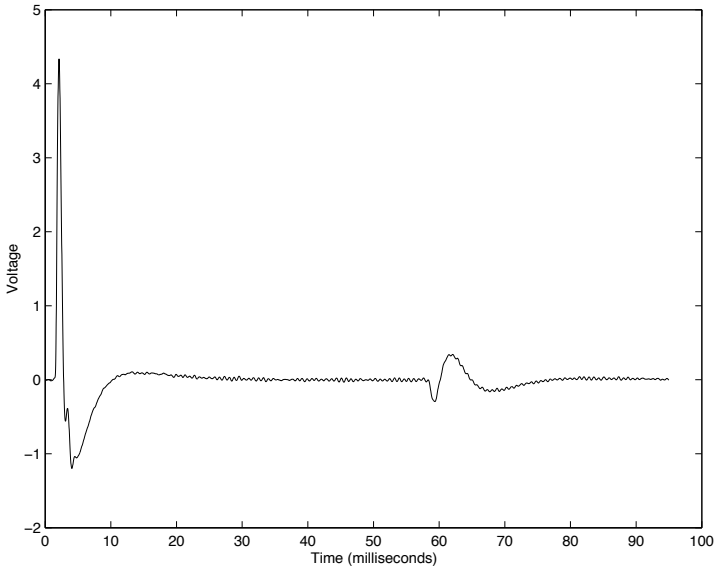

Figure 7.3: Calibration pulse including source reflections

part of the object reflections, consisting entirely of backward travelling waves. R_j, the second part of the object reflections, however, is in general $R_j = R_j^+ + R_j^-$ where R_j^+ is the forward travelling reflection of R_i off the loudspeaker and R_j^- is the remains of the backward travelling wave. In order to reconstruct the bore we want to isolate R_j^- by calculating R_j^+ and subtracting:

$$R_j^+(\omega) = H(\omega) \times R_i(\omega) \tag{7.2}$$

and $R_j^- = R_j - R_j^+$.

7.4 Results

Figure 7.4 shows the object reflection data for a test object consisting of stepped cylinders and is a longer version of the test object used in chapter 5. The first section of the object is a 50 mm long section with a radius of 5mm (the same as the source tube), the second section is 650 mm long with an internal radius of 6.25 mm and the third section is 650 mm long with an internal radius of 9.4 mm. The object reflections are not long enough in this example to overlap with the source reflections, which can clearly be seen starting at around 60 ms.

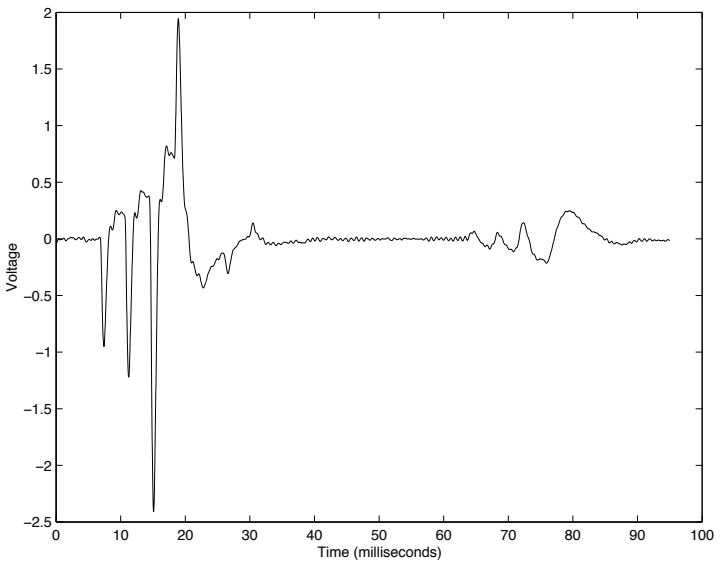

Figure 7.4: Reflections from long stepped cylinder test object including source reflections

Figure 7.5 displays the second half of the object reflection data, labelled R_j. Also shown is R_j^+, the result of applying the source reflection filter to give the

forward travelling component of R_j, due to source reflections. R_j^- is the result of subtracting R_j^+ from R_j to give the backward travelling component, due to any remaining object reflections, with the source reflections cancelled. As we expect for this example, the data in the region shown consists entirely of source reflections with R_j^- equal to zero, give or take a small amount of noise. Figure 7.6 shows the full object reflection data, before and after the cancellation of the source reflections. The success of the post-processing subtraction of the source reflections can be clearly seen.

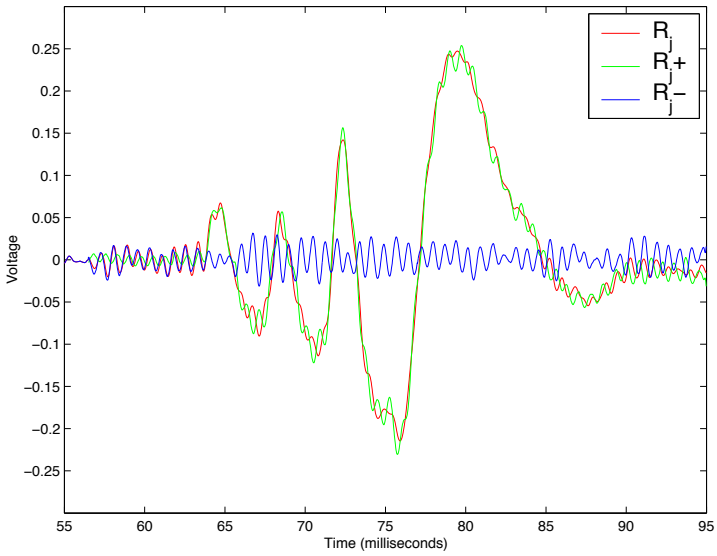

Figure 7.5: Second half of long stepped cylinder test object reflections

Figure 7.7 on the other hand shows the reflections from a French horn. The object reflections are too long to be separated in the time domain from the source reflections. Subtracting the source reflections is therefore vital if the response of the instrument is to be measured.

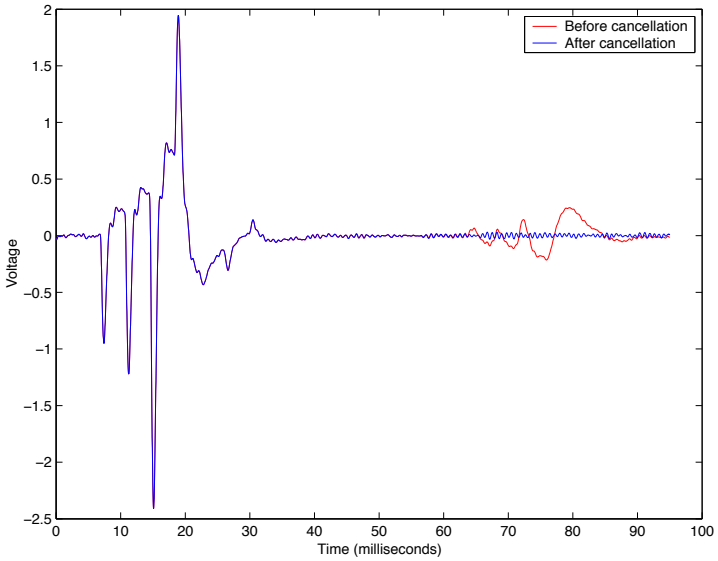

Figure 7.6: Long stepped cylinder test object reflections

Figure 7.8 and figure 7.9 show bore reconstructions of the French Horn. Both use the virtual dc tube method. The line labelled "Old method" shows the reconstructed bore of a French horn using the pressure signal shown in figure 7.7 truncated just before the source reflections arrive. There is an upward trend in the bore reconstruction of a section of the pipe which is, in reality, cylindrical. The reconstruction is not accurate because the object reflections have not completely died out at this point. Also shown is a line labelled "Crook," which shows the reconstructed bore of the detached crook (the section of tubing between the mouthpiece and the rest of the instrument). Since the crook section is short, the object and source reflections are separated in the pressure recording and, in this case, truncation of the signal gives an accurate reconstruction. The "New method" result uses the post processed version of the figure 7.7 object reflections

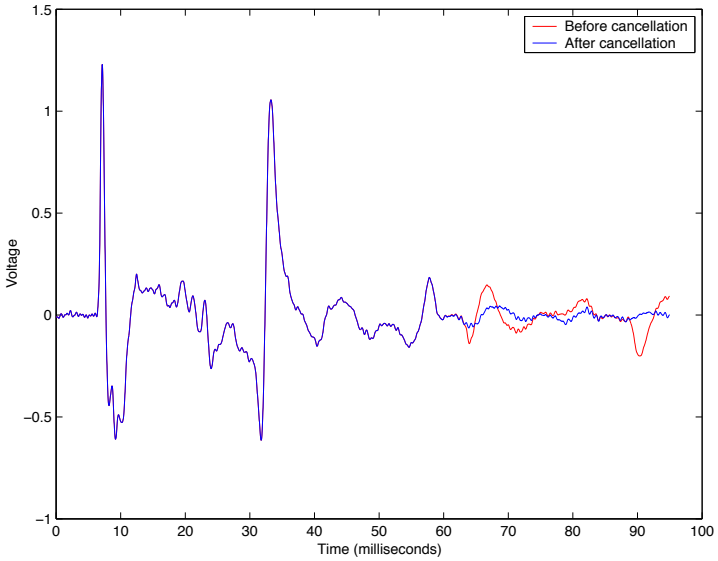

Figure 7.7: French horn object reflections

with the source reflections removed.

The source reflection cancellation reconstruction of the French horn agrees with the reconstruction of the crook section showing that the technique enables longer objects to be measured accurately. While we have not verified that the remainder of the horn is reconstructed correctly (in fact there will still be errors due to higher mode propagation at the bell), it is clear that deviation has been greatly reduced.

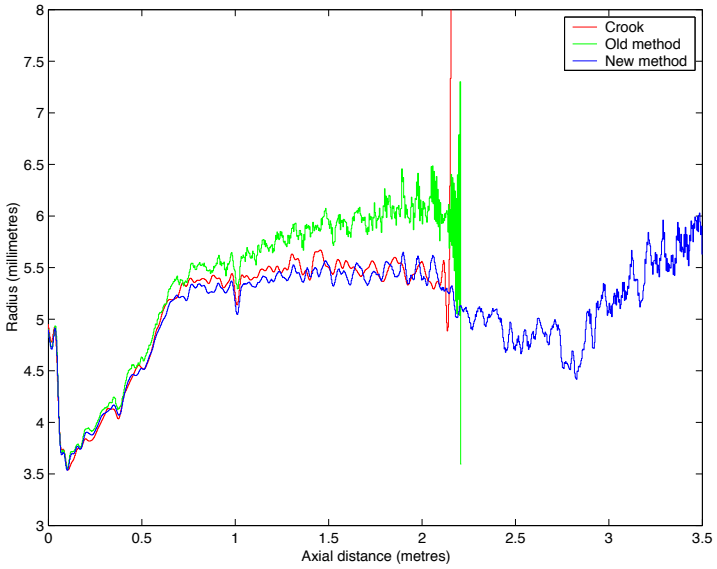

Figure 7.8: French horn bore reconstruction, first 3.5 metres

7.5 Maximum length sequences

The method used so far for measuring the input impulse response involves injecting a pulse into the source tube and measuring the reflections. By using a signal that continues over a longer time interval we may put more energy into the system, improving the signal to noise ratio and removing the need to average over 1000 measurements. Obviously, white noise cannot be used because we need the phase information as well as frequency response. Equivalently there must be some way of analysing the measured reflections to recover the time domain response to a single pulse.

One solution is to use a pseudo-random binary signal called a maximum length

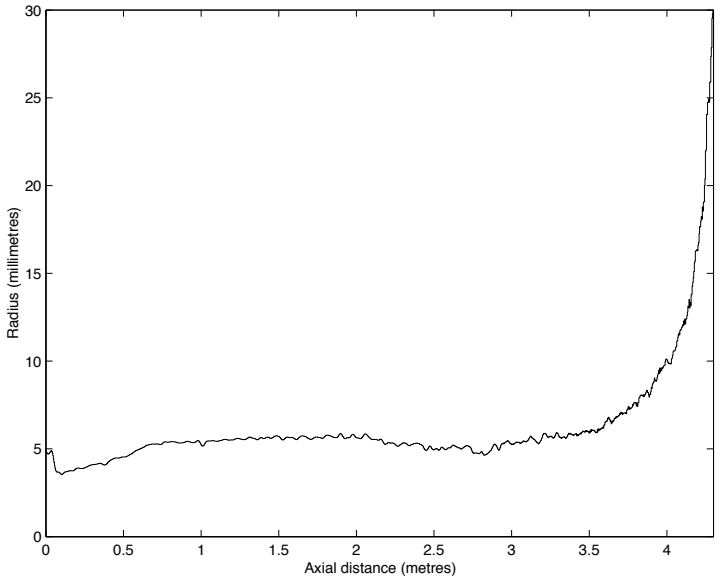

Figure 7.9: French horn bore reconstruction, first 4.3 metres

sequence (MLS). An MLS signal consists of an apparently random sequence of 0's and 1's that has a flat frequency spectrum for all frequencies up to the Nyquist frequency with the exception of the dc value. It is also computationally efficient to generate such a sequence on computer and unlike white noise an MLS signal is deterministic and therefore repeatable. The input impulse response of a system can be extracted by a cross-correlation procedure. This method of excitation has been employed frequently in measuring the input impulse response of rooms for reverberation measurement [65, 66, 67]. Here we discuss how MLS signals may be generated and the resulting measurements analysed. The discussion leads on to the application of MLS excitation in acoustic pulse reflectometry.

7.5.1 Generating an MLS sequence

Generation of an MLS signal can be done using a feedback shift register [68, 65]. The shift register consists of a group of m binary memory elements in a line. At each time unit the numbers held in the memory elements are passed on one step to the right and the vacated element on the left is generated by a recursion relation which depends on the number of memory elements, m. The values which exit the element group on the right hand side form the output sequence.

There are several recursion relations that may be used to generate an MLS. We will not derive these, rather we will use the simplest (and therefore most computationally efficient) available. As an example, consider a shift register of $m = 4$ elements. The recursion relation we use is directly related to the primitive polynomial [69]

$$h(x) = x^4 + x + 1. \tag{7.3}$$

The memory elements corresponding to the terms in $h(x)$ are added and the result taken modulo 2 (ie. the remainder when divided by two) to give the left entry on the following time step. As is shown in figure 7.10, the term 1 in $h(x)$ corresponds to the value held in a_i, the term x refers to the term a_{i+1} and the term x^4 is not part of the sum because there are only 4 memory elements. The primitive polynomial therefore corresponds to the recursion relation $a_{i+4} = a_{i+1} + a_i$. The last and second last elements are therefore used to calculate the new left hand

element, and since the sum is taken modulo 2 the operation is equivalent to the exclusive OR gate as shown in the figure.

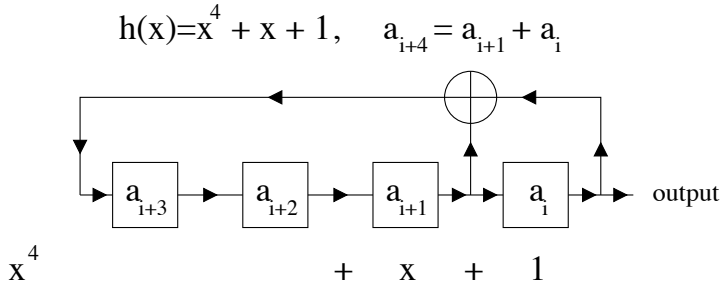

Figure 7.10: Feedback shift register and recurrence relation for $m = 4$

In order to generate an MLS in practice we have to specify an initial state for the memory elements. Here we will use 1111. The last and second last elements are both 1, so the sum is 2, which when taken modulo 2 gives a result of 0 for the left hand element at the next step. The other elements shift one step to the right, giving 0111 as the next state of the four elements, and the 1 which exited on the right is the first term in the output sequence.

Table 7.1 shows the state of the memory element group at each time step and the MLS can be seen building up vertically down the right hand column. The MLS sequence appears random, but repeats with a period of 15. In fact, the element group takes every binary value possible except 0000 which would be a dead end for the sequence since a 1 would never be generated. The number of possible values for a binary number with m digits is 2^m so the maximum length for an MLS signal must therefore be $2^m - 1$, hence the name maximum length

Time step, i	Elements, $(a_{i+3}, a_{i+2}, a_{i+1}, a_i)$	MLS signal, a_i
0	1111	1
1	0111	1
2	0011	1
3	0001	1
4	1000	0
5	0100	0
6	0010	0
7	1001	1
8	1100	0
9	0110	0
10	1011	1
11	0101	1
12	1010	0
13	1101	1
14	1110	0
15	1111	1
16	0111	1
:	:	:

Table 7.1: MLS element sequence for $m = 4$

sequence. It follows that the initial state is unimportant to the properties of the MLS signal (as long as 0000 is not taken) since the sequence covers all non-zero states and is periodic.

For other values of m, the only difference in the method for generating an MLS is that we use m memory elements and we must use a different primitive polynomial, of order m. The polynomials up to $m = 168$ are listed by Stahnke [69] and are shown in recursion relation form up to $m = 20$ in table 7.2. The length of an $m = 20$ sequence is $2^{20} - 1 = 1048575$ samples which corresponds to over 23 seconds of sound when played as an acoustic signal at 44.1 kHz.

m	Recursion relation
1	$a_{i+1} = a_i$
2	$a_{i+2} = a_{i+1} + a_i$
3	$a_{i+3} = a_{i+1} + a_i$
4	$a_{i+4} = a_{i+1} + a_i$
5	$a_{i+5} = a_{i+2} + a_i$
6	$a_{i+6} = a_{i+1} + a_i$
7	$a_{i+7} = a_{i+1} + a_i$
8	$a_{i+8} = a_{i+6} + a_{i+5} + a_{i+1} + a_i$
9	$a_{i+9} = a_{i+4} + a_i$
10	$a_{i+10} = a_{i+3} + a_i$
11	$a_{i+11} = a_{i+2} + a_i$
12	$a_{i+12} = a_{i+7} + a_{i+4} + a_{i+3} + a_i$
13	$a_{i+13} = a_{i+4} + a_{i+3} + a_{i+1} + a_i$
14	$a_{i+14} = a_{i+12} + a_{i+11} + a_{i+1} + a_i$
15	$a_{i+15} = a_{i+1} + a_i$
16	$a_{i+16} = a_{i+5} + a_{i+3} + a_{i+2} + a_i$
17	$a_{i+17} = a_{i+3} + a_i$
18	$a_{i+18} = a_{i+7} + a_i$
19	$a_{i+19} = a_{i+6} + a_{i+5} + a_{i+1} + a_i$
20	$a_{i+20} = a_{i+3} + a_i$

Table 7.2: Recursion relations for MLS of length $2^m - 1$

7.5.2 Auto-correlation property of MLS

In order to use an MLS in a measurement, it is preferable to convert the signal to one which oscillates around zero rather than above zero because this reduces the dc offset and therefore improves the efficiency of loudspeakers and measurement systems. This can be done by defining s as a sequence obtained by replacing every 0 with 1 and replacing every 1 with -1 as follows:

$$s_0, s_1, s_2, s_3.... = (-1)^{a_0}, (-1)^{a_1}, (-1)^{a_2}, (-1)^{a_3}.... \tag{7.4}$$

The auto-correlation function, ρ, is defined as [68]

$$\rho(i) = \frac{1}{n} \sum_{j=0}^{n-1} s_j s_{i+j}^*. \tag{7.5}$$

where $n = 2^m - 1$ is the length of the sequence. Note that the subscript $i+j$ can exceed n. When this happens the subscript is taken modulo n (ie. n is subtracted so that s_{i+j} is a circularly shifted version of s). The symbol * denotes complex conjugation which may be dropped in the current application because all entries in the sequence are real.

For the MLS defined in equation (7.4), the auto-correlation becomes:

$$\rho(i) = \frac{A - D}{n}, \tag{7.6}$$

where A is the number of times the elements s_j and s_{i+j} agree and D is the number of times they disagree. The first term in ρ is given by $i = 0$ so s_j and s_{i+j} agree for all values of j giving $\rho(0) = 1$. When $1 \leq i \leq n-1$ we are calculating the agreement between the signal and a circularly shifted version. Since the signals appear random, it is intuitive that the agreement and disagreement should be almost equal. The proof in [68] shows that $A - D = -1$ for $1 \leq i \leq n-1$. The auto-correlation of the MLS is therefore

$$\rho(i) = \begin{cases} 1 & : \quad i = 0, \\ -1/n & : \quad 1 \leq i \leq n-1, \end{cases} \tag{7.7}$$

which is distinguished from a perfect digital impulse by the presence of the small non-zero value when $i \neq 0$. While the frequency spectrum of an ideal digital impulse is equal for all frequencies, the frequency spectrum of ρ is the same for all frequencies except for the zero frequency component.

7.5.3 Extracting the system impulse response from MLS measurement

The frequency content of the signal recorded at the microphone will contain information on the frequency response of the system under test. In order to go beyond this and get the impulse response of the system, we must use the auto-correlation property of the MLS signals. First recognise that the measured

signal is the convolution of the MLS and the system impulse response. We will define the input impulse response of our system as h. We will refer to h as the system impulse response to prevent confusion with the input impulse response of a pulse reflectometry test object. This distinction will be discussed in more detail in section 7.5.4. The MLS signal is s, so the pressure, y, measured at the microphone will be

$$y = s * h \tag{7.8}$$

where $*$ here denotes convolution. Performing correlation with respect to s on both sides of equation (7.8) gives [70]:

$$\phi_{sy} = \phi_{ss} * h = \rho * h \tag{7.9}$$

where ϕ_{ab} is notation for the correlation of a and b. Note that convolution in the time domain is multiplication in the frequency domain, so the fact that the frequency spectrum of ρ is flat, except for the zero frequency component, means that h is left unchanged by convolution with ρ except for a small dc offset of the order of $1/n$. The impulse response of the system can therefore be extracted from the measurement of the system response by correlation with the MLS input. Correlation is defined as

$$\phi_{sy}(i) = \frac{1}{n}\sum_{j=0}^{n-1} s_j y^*_{i+j} = \frac{1}{n}\sum_{j=0}^{n-1} s_{j-i} y^*_j \tag{7.10}$$

which can be converted to a matrix notation by making a matrix S_n consisting of n circularly shifted versions of s [70]:

$$\mathbf{\Phi}_{sy} = \frac{1}{n} S_n \mathbf{Y}. \tag{7.11}$$

The elements of S_n are given by $S_n(i,j) = s_{j-i}$ where $j-i$ is taken modulo n so that the successive rows of the matrix contain s shifted one step to the right each time with the values leaving on the right appearing on the left. $\mathbf{Y}$ is a column vector of the measured system response and $\mathbf{\Phi}_{sy}$ a column vector of the resulting correlation.

The cross-correlation can also be performed in the frequency domain by considering the close relationship between cross-correlation and convolution. Deconvolution was performed by frequency domain division in chapter 5. Convolution on the other hand may performed by multiplication in the frequency domain. Cross-correlation of two signals is the reverse of the first sequence convolved with the second sequence [59] pp.92–96:

$$\phi_{ab}(t) = a(-t) * b(t). \tag{7.12}$$

Reversal in the time domain means complex conjugation in the frequency domain:

$$\text{fft(a(}-\text{t))} = (\text{fft(a(t))})^*. \tag{7.13}$$

It therefore follows that the cross-correlation of two signals in the time domain becomes the conjugate of the first signal multiplied by the second signal in the frequency domain.

$$\mathrm{fft}(\phi_{\mathrm{ab}}) = \frac{1}{\mathrm{n}}(\mathrm{fft(a)})^* \times (\mathrm{fft(b)}). \tag{7.14}$$

Discrete Fourier transforms are used for the analysis in this chapter. The speed of analysis is acceptable for the measurements we present here. Before acceptable computational power was available, it was necessary to perform interpolation to make the length of the sequence up to 2^m, enabling the use of fast Fourier transforms [66]. Another option is the fast Hadamard transform technique as set out in Borish and Angell [70] which does not require interpolation and is less computationally expensive.

7.5.4 Acoustic pulse reflectometry measurement with MLS excitation

It is important to realise at this stage that the system impulse response, h, of a reflectometer is not simply the input impulse response of the object on the output end of the reflectometer; it includes the impulse response of the loudspeaker, the losses in the source tube, the input pulse passing the microphone on its way to the loudspeaker, the source reflections and so on. The system impulse response, h, that we have calculated can be chopped to isolate the object reflections. These

object reflections are equivalent to those that can be measured by the conventional pulse excitation except that our signal to noise ratio is much improved. The deconvolution of object reflection and calibration pulse measurements is still necessary when using MLS excitation.

MLS signals are inherently periodic with a period of $2^m - 1$. In equation (7.8) the system impulse response, h, (which is not periodic) is convolved with the MLS signal, s. The result is that y is the periodic response of the system to continuous excitation by the periodic MLS. When we perform our experiments, we must choose an MLS signal whose period time is larger than the total response time of the system in order to prevent the end of our calculation of the system response folding back onto the start. Similarly, we must play the MLS signal end to end twice and ignore the response during the first run through in order to make sure that the response we are measuring conforms to the periodicity condition.

Figure 7.11 shows the signal recorded at the microphone when an MLS signal of order $m = 15$ is fed into the loudspeaker. The shorter reflectometer with $l_1 = 7.37$m and $l_2 = 3.10$m is used and data acquisition is performed in Matlab for Windows with a Guillemot soundcard at a sample rate of $F_s = 44100$Hz. Sampling of the microphone reflections is started and then the start of the MLS signal is fed to the loudspeaker. The signal from the loudspeaker should take $l_1/c = 7.37/343 \approx 0.02$s to reach the microphone. In fact, the first 0.04 seconds of the recording consists only of undesired background noise, showing that there

is delay of 0.02 seconds between the start of the sampling and the start of the MLS signal leaving the loudspeaker. This delay is caused by computer processing time and means that care must be taken when we are isolating the part of the system impulse response corresponding to the object reflections or calibration pulse.

The time period for a $m = 15$ sequence is $(2^m - 1)/F_s = 0.743$ s which will also be the time length of our resulting measurement data for the system impulse response. This is considerably longer than the total time taken for an acoustic pulse to decay to zero as can be deduced from the fact that the pressure waves are much reduced by losses and reflection from the loudspeaker after 0.1 seconds in say figure 7.3. As mentioned previously, both the MLS and measured response are assumed to be periodic by the theory. Figure 7.11 shows the microphone pressure sampled while two periods of the MLS are played by the loudspeaker, end to end. The microphone signal during the second period therefore features the response to the last part of the previous period of excitation so satisfying the periodicity requirement. This signal is shown isolated in figure 7.12.

The auto-correlation of the MLS input and the recorded response from figure 7.12 was performed in the frequency domain using equation (7.14). Figure 7.13 shows the result. This is the full system impulse response and features the input pulse passing the microphone, the reflection of the pulse from the closed end of the source tube and the source reflections. The response shows that all acoustic

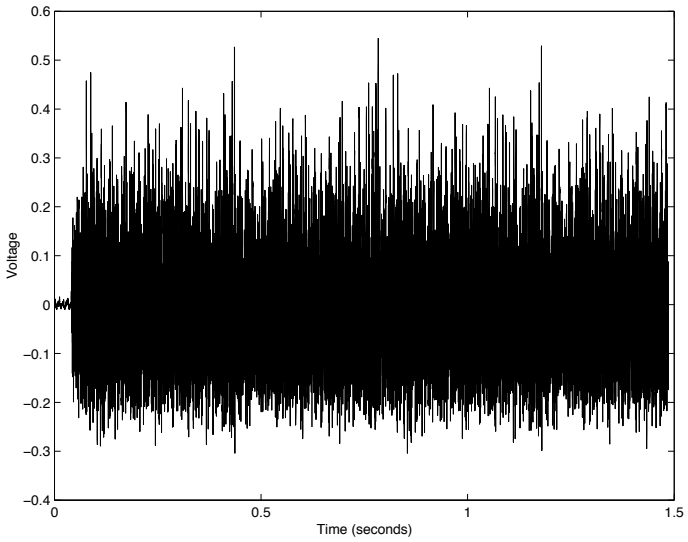

Figure 7.11: Microphone signal for excitation with a $m = 15$ MLS signal repeated twice

energy decays to zero about 0.2 seconds after a pulse is produced as was expected.

Figure 7.14 shows the calibration pulse or reflections from the closed end of the source tube obtained by chopping the system impulse response. The exact recorded time at which the calibration pulse arrives in the system impulse response depends on the time lag between the starting of sampling and the starting of the excitation as mentioned previously. This time lag depends on the software, hardware specifications and the computational load. In order to avoid this problem, the sample in the system impulse response with the maximum value (corresponding to the maximum of the input pulse) is first found. The position of the reflections from the closed end or test object can be defined relative to this point, meaning that the input/output time lag does not effect the results.

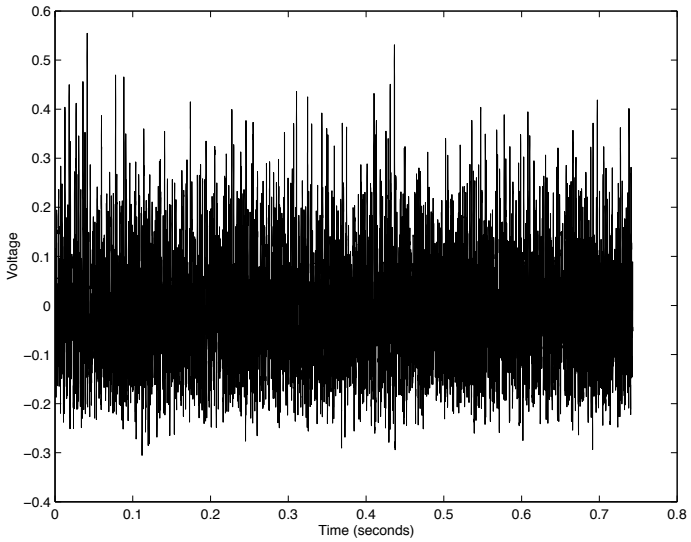

Figure 7.12: Microphone signal chopped to show one period of response to continuous excitation with a $m = 15$ MLS signal

This experiment can be repeated with a musical instrument or test object on the end of the source tube and analysed with the calibration pulse measurement to obtain the bore reconstruction and input impedance. By selecting appropriate delay times, the virtual dc tube and source reflection cancellation methods can be used.

Figure 7.15 shows the object reflections obtained by chopping a system impulse response measurement performed with the short stepped cylinder test object used in chapter 5 on the end of the source tube. As with the previous experiment an MLS of order $m = 15$ was used. The object reflections were isolated from the system impulse response 2ms earlier than for the calibration pulse, meaning that

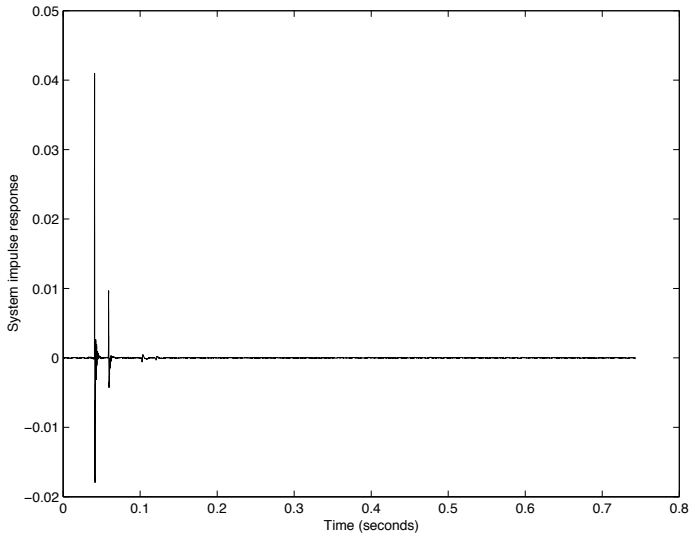

Figure 7.13: System impulse response

the virtual dc tube method can be applied.

Figure 7.16 shows the resulting bore reconstruction with $m = 15$. Also shown is the result of performing the experiment with excitation with a much longer MLS signal of $m = 19$. Such an MLS signal will have a time length of $(2^m - 1)/F_s = 11.89$ s. Calculating the discrete Fourier transform of a signal this length takes several seconds with the current computational power available. Using an increased order means that more energy is added to the system, so improving the signal to noise ratio. The bore reconstruction with $m = 15$ measures the radius of the final cylindrical section to be 0.4 mm too large, while the $m = 19$ measurement is much improved, averaging just 0.1 mm more than the correct value. The level of oscillations in supposedly cylindrical sections of bore are

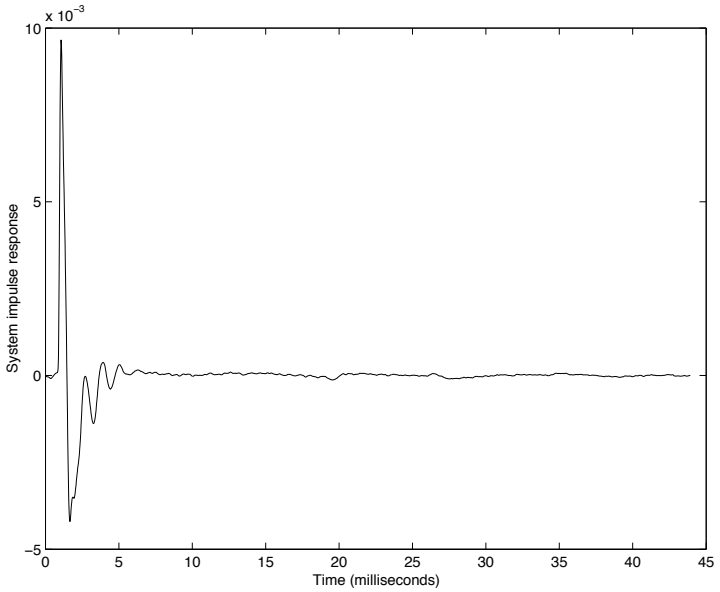

Figure 7.14: Calibration pulse isolated from system impulse response

slightly reduced by the increase in order. This implies that the noise level at high frequency is reduced by the fact that we have added more energy to the system. The fact that the $m = 19$ reconstruction of the last cylinder has an average value closer to the correct radius is evidence of greater accuracy at low frequencies.

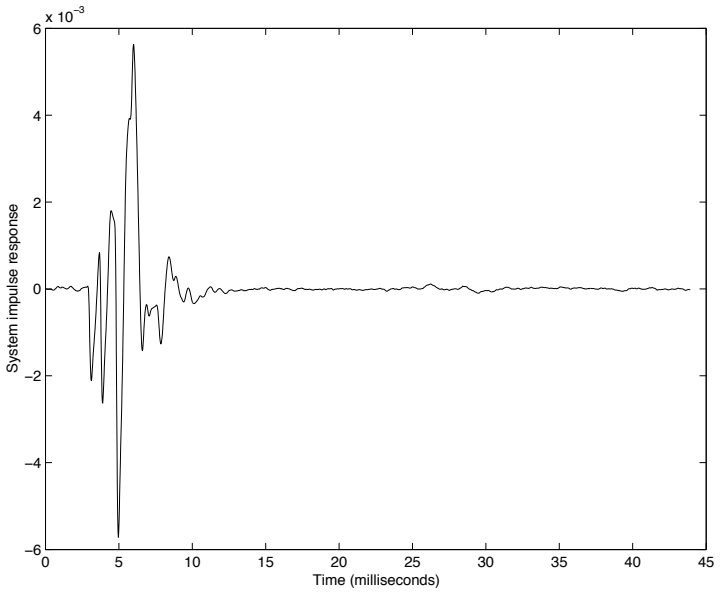

Figure 7.15: Object reflections isolated from system impulse response

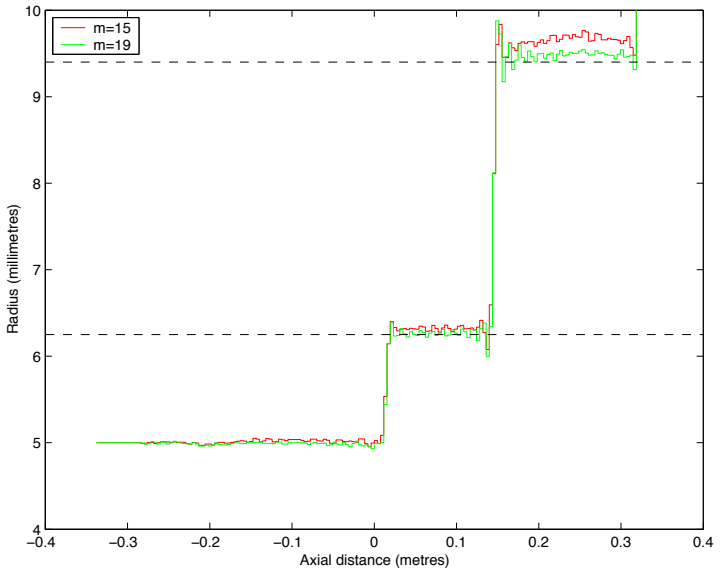

Figure 7.16: Reconstructions for different orders of MLS excitation

Chapter 8

Conclusions

8.1 Achievement of aims

8.1.1 Aim 1

The first aim was to study and develop the theory of multimodal propagation in acoustic horns, in order to enable the influence of higher mode propagation to be assessed.

The theory of propagation of modes in pipes has been reviewed. Plane wave propagation was discussed, followed by the theory of multimodal propagation. This work centred on a method of calculation of the input impedance of an acoustic horn. This quantity gives information on the resonance properties. Also

discussed was a method for studying the pressure field inside the horn. New work presented includes the treatment of ducts of rectangular cross-section in addition to the existing theory for circular cross-section. In order to perform calculations, the properties of radiation of sound from the open end must be characterised by calculation of the radiation impedance.

An expression for the multimodal radiation impedance of both cylindrical and rectangular ducts terminated in an infinite baffle has been derived. From the initial quadruple integral expression the problem was reduced to one dimension in cylindrical geometry and two dimensions in rectangular geometry with the singularity removed to allow practical numerical integration. Results are presented highlighting the difference between direct and coupled impedances and comparisons made between the geometries.

Numerical calculations of the input impedance and pressure field of the bell section of a trumpet then followed. The inclusion of just one extra mode made a large difference in the input impedance, modelling the absorption of energy from plane wave propagation by mode conversion. Inclusion of each successive extra mode made changes of ever decreasing magnitude to the input impedance calculation.

The reflection of sound from a single step between two infinite tubes is trivial if the plane wave approximation is used. We went on to discuss the reflection from such a geometry when multimodal propagation is used. In this case the reflected

amplitude of a sinusoidal pressure wave is frequency dependent. Calculations of the frequency response were presented. The results demonstrate how the reflected amplitude increases with frequency in the low frequency range where only the plane wave mode can propagate. The time domain input impulse response was then calculated by Fourier transform. If an ideal impulse is incident from one side of the geometry, the plane wave component of the reflection is a pulse with a wake consisting of oscillations. These oscillations are caused by a peak in the frequency domain reflection at the first cut-off frequency; only the plane wave mode is propagating below the cut-off frequency but the plane wave mode and one higher mode may propagate above cut-off.

8.1.2 Aim 2

The second aim was to review acoustic pulse reflectometry as a means of measuring the properties of brass musical instruments, and to perform experiments to give examples of its use.

The theory behind acoustic pulse reflectometry has been reviewed. This included the calculation of the input impedance and bore profile from the input impulse response. An existing practical system used for the measurement of the input impulse response of brass instruments was then set out. Measurements of the input impulse response, input impedance and bore profile were carried out on a test object consisting of two cylindrical sections. Because the actual bore

profile was well known, the accuracy of the of the layer-peeling algorithm was readily quantified to be around 0.1mm for this object. Also, the input impedance was compared with theoretical calculations using the multimodal theory for both the stepped tube test object and the bell section of a trumpet.

8.1.3 Aim 3

The third aim was to develop acoustic pulse reflectometry to enable the measurement of longer instruments and to speed up the measurement process.

In the original pulse reflectometry method, a cylindrical connector called the "dc tube" was placed between the source tube and the object under test. This was necessary to enable easy removal of the dc offset in the measurement upon which the bore reconstruction is highly sensitive. By developing the virtual dc tube method, the need for attaching this cylindrical connector was eliminated, making the measurement process quicker, more reliable and compact. In addition to this, a source reflection cancellation method was shown to successfully remove the reflections from the source, enabling the measurement of longer objects. MLS excitation has been shown to be useful for improving signal to noise ratio, thereby removing the need to perform many measurements and average the results.

8.1.4 Aim 4

The fourth aim was to discuss the possibility of including higher modes in the analysis of pulse reflectometry data.

The existing algorithm used to calculate the bore profile of an object from the measured input impulse response assumes plane wave propagation. The possibility of including the frequency dependence of primary reflections derived from multimodal theory within the bore reconstruction algorithm has been discussed. Projection matrices have been derived which allow projection of forward and backward going multimodal pressure waves across discontinuities and cylinders. Deducing the cross-section changes is complicated by the frequency dependence of the reflections, even when the forward and backward going waves are known from multimodal calculation. This problem is an area suitable for further work. A large increase in computational load is another problem.

An iteration procedure could be an alternative option. The multimodal impedance method could be used to calculate the input impulse response of the bore profile obtained by the plane wave bore reconstruction. Comparison with the actual measured input impulse response would then give a useful estimate of the error in the bore reconstruction calculated using the plane wave algorithm. The bore could then be corrected to compensate for this difference and the process of correction repeated iteratively until a bore is obtained for which the input impulse response agrees with that measured experimentally.

8.2 Future work

Ideas for the development of pulse reflectometry which may be useful for improving the technique will now be reviewed, followed by a discussion of possible future work on multimodal propagation.

One of the fundamental limitations of the pulse reflectometry is the bandwidth of the source of acoustic energy. The compression driver loudspeakers used at present give little energy above 10 kHz, due to their limited frequency response and due to losses in the source tube. This means that sharp steps in the bore are reconstructed relatively poorly. More of a problem, however, are the very low frequencies (50 Hz and below) which have long wavelengths, so will have an influence on the general upward and downward trend of the reconstructed bore. In particular, no energy may be produced by the loudspeaker at the zero of frequency, hence the zero frequency bin in the frequency domain response is not accurately measured. This means a lack of accuracy in the dc offset in the time domain input impulse response, which is why the dc offset must be calculated by averaging the response from a cylindrical tube section (an actual or virtual dc tube) and subtracted in post-processing.

An alternative is to deduce the value of the zero frequency bin from first principles. The zero frequency bin of the input impedance must be zero for all open ended instruments because pressure will not build up due to a steady velocity.

Studying the equations relating the frequency domain input impedance and input impulse response reveals that the zero frequency bin of the input impulse response will have a value of -1. Setting the zero frequency bin of the frequency domain input impulse response to -1 before inverse Fourier transforming to the time domain should then remove the dc offset. While much effort has been expended in removing the dc offset in more complicated ways, preliminary results suggest that this simple technique is effective for dc offset removal. It should be noted that this method has not been implemented previously due to bandwidth problems which we will now discuss.

There is an inevitable discontinuity between the end of the source tube and the object under test. Ideally this would show as a small impulse at the start of the input impulse response. Because of the limited bandwidth of the measurement this impulse is spread over several samples in the time domain, both before and after the $t = 0$ sample. There are no samples before $t = 0$, so the measurement is in some way corrupted. A signal introduced "before" the first sample is actually observed in the final few samples of the signal because Fourier transforms are inherently periodic. This apparently non-causal signal represents part of the energy of the reflection from the first step however, and should be present after the first sample in the input impulse response if a bore reconstruction is to be accurate. We may achieve this by using the virtual dc tube method to delay the object reflections. Because the dc offset was calculated by averaging the response over the first couple of milliseconds, the dc tube was previously around 40 cm

long. The method suggested here would only require a very short virtual dc tube whose length corresponds to the distance sound propagates in a few time samples.

As mentioned previously, the bandwidth is partly controlled by losses. High frequencies are attenuated by travel in the source tube much more strongly than low frequencies. The use of longer source tubes to enable measurement of longer objects accentuates this problem. A solution currently being investigated is to use multiple microphones. This enables the forward and backward going waves to be separated, so removing the problem of interference between the input signal, the reflected signal and the source reflections. The source tube can then be made far shorter, decreasing the losses at high frequency and increasing the bandwidth. A source tube with five microphones is currently being developed to enable large bandwidth measurement. Preliminary results for two microphones have been presented recently by van Walstijn et al. [71].

The formula used in deconvolution of the object reflections and calibration pulse to produce the input impulse response is another area of useful study. A constraining factor is included in the frequency domain division to prevent high frequency noise occurring. The effect of this is to filter out any high frequencies in the input impulse response. This is not mathematically rigorous; the answer depends slightly on the arbitrary choice of constraining factor. Work on applying truncated singular value decomposition, a more advanced method of deconvolution, to pulse reflectometry data is discussed by Forbes et al. [72].

A more minor improvement to the single microphone method of acoustic pulse reflectometry which may be applied to increase the speed at which experiments can be performed is to measure the calibration pulse simultaneously with the object reflections. At present, the calibration pulse (the reflection from closing the end of the source tube) is deconvolved from the object reflections to calculate the input impulse response of the object. We may improve upon this by recording the full system impulse response, including the pulse passing the microphone on the way to the object under test. The calibration pulse may then be calculated by applying a loss filter to the recording of the pulse passing the microphone the first time, to account for the difference in propagation distance between the pulse passing the microphone initially and the reflections which return from the end of the source tube. The object reflections may be isolated as normal. This method will be especially easy to apply with MLS excitation because full system impulse response measurements have already been performed.

The derivation of an expression for the multimodal radiation impedance of an open ended pipe without a baffle would be a productive area of research as it would enable increased realism, and therefore accuracy, in input impedance calculations. Further work is also necessary to include higher modes in a pulse reflectometry bore reconstruction algorithm using the approaches discussed in chapter 6. Optimisation methods are currently being studied with a view to correcting the plane wave bore reconstruction algorithm results by minimising the difference between the theoretical input impulse response of the bore reconstruc-

tion and the measured input impulse response.

Appendix A

Properties of Bessel functions

n	γ_n	n	γ_n	n	γ_n
0	0.0000000	16	51.0435352	32	101.3126618
1	3.8317060	17	54.1855536	33	104.4543658
2	7.0155867	18	57.3275254	34	107.5960633
3	10.1734681	19	60.4694578	35	110.7377548
4	13.3236919	20	63.6113567	36	113.8794408
5	16.4706301	21	66.7532267	37	117.0211219
6	19.6158585	22	69.8950718	38	120.1627983
7	22.7600844	23	73.0368952	39	123.3044705
8	25.9036721	24	76.1786996	40	126.4460139
9	29.0468285	25	79.3204872	41	129.5878033
10	32.1896799	26	82.4622599	42	132.7294644
11	35.3323076	27	85.6040194	43	135.8711224
12	38.4747662	28	88.7457671	44	139.0127774
13	41.6170942	29	91.8875043	45	142.1544297
14	44.7593190	30	95.0292318		
15	47.9014609	31	98.1709507		

Table A.1: Zeros of the Bessel function J_1 to 7 decimal places

Standard integral from Jahnke and Emde [73] p146:

$$\int xJ_p(\alpha x)J_p(\beta x)dx = \frac{\beta xJ_p(\alpha x)J_{p-1}(\beta x) - \alpha xJ_{p-1}(\alpha x)J_p(\beta x)}{\alpha^2 - \beta^2} \tag{A.1}$$

From Kreyszig [55] p230:

$$J_{-n}(x) = (-1)^n J_n(x) \tag{A.2}$$

and p232:

$$\frac{d}{dx}[x^{-\nu}J_\nu(x)] = -x^{-\nu}J_{\nu+1}(x) \tag{A.3}$$

Appendix B

Projection at a discontinuity

B.1 General expression

In this section we will derive the general equations resulting from matching the acoustic pressure and velocity fields on the air shared at a discontinuous join between two tubes of differing cross-sectional area. The geometry we are considering is shown in figure B.1.

B.1.1 Pressure

We denote the pressure field on surface 1 as $p^{(1)}(x, y)$ and the pressure field on surface 2 as $p^{(2)}(x, y)$. In plane wave propagation we saw that the pressure is taken to be the same on both sides of the discontinuity. In the multimodal case

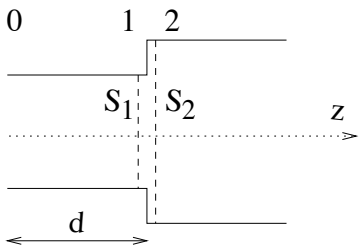

Figure B.1: Detail of a waveguide consisting of straight sections of length d joined discontinuously

the pressure field is matched at either side. For the case shown where $S_2 > S_1$ the pressure is matched on the air they share, S_1.

$$p^{(1)} = p^{(2)} \quad \text{on} \quad S_1, \quad S_1 < S_2 \tag{B.1}$$

Now the concept of orthogonality of the modes is used. Recalling our orthogonality relation from equation (2.47):

$$\int_S \psi_n \psi_m dS = S\delta_{nm} \tag{B.2}$$

it follows that the integration of the mode profile ψ_n with a general pressure field, p will extract the component of the nth mode in the pressure field. Using the fact that the pressure may be expressed as a sum of the modes from equation 2.26 (ignoring the $\exp(i\omega t)$ time factor):

$$\int_S \psi_n p dS = \int_S \psi_n \sum_{m=0}^{\infty} \psi_m P_m dS = P_n S. \tag{B.3}$$

We will use $P_n^{(1)}$ and $P_n^{(2)}$ to denote the complex mode amplitudes on surfaces 1 and 2 respectively. $\psi_n^{(1)}$ and $\psi_n^{(2)}$ are the corresponding mode profiles on surfaces 1 and 2. Combining equations (B.1) and B.3) gives

$$P_n^{(1)} = \frac{1}{S_1}\int_{S_1} \psi_n^{(1)} p^{(1)} dS = \frac{1}{S_1}\int_{S_1} \psi_n^{(1)} p^{(2)} dS = \frac{1}{S_1}\int_{S_1} \psi_n^{(1)} \sum_{m=0}^{\infty} \psi_m^{(2)} P_m^{(2)} dS \qquad \text{(B.4)}$$

which may be written as

$$P_n^{(1)} = \sum_{m=0}^{\infty} F_{nm} P_m^{(2)} \qquad \text{(B.5)}$$

where

$$F_{nm} = \frac{1}{S_1}\int_{S_1} \psi_n^{(1)} \psi_m^{(2)} dS. \qquad \text{(B.6)}$$

Using matrix notation, $\mathbf{P}^{(2)}$ is a column vector whose entries are given by $P_m^{(2)}$ and

$$\mathbf{P}^{(1)} = F\mathbf{P}^{(2)}, \qquad S_1 < S_2 \qquad \text{(B.7)}$$

where F is a matrix with elements F_{nm}. We have now proved equations (2.79) and (2.80) from chapter 2.

We now have a formula giving the pressure on a smaller cross-section at a discontinuity from the pressure on a larger cross-section on the other side. Since S_1 and S_2 are assumed to not be separated by any distance along the z axis the formula holds whatever side the largest cross-section is on. Consider if $S_1 > S_2$. Now section 1 is the larger cross-section meaning that we just have to interchange

the labels 1 and 2 in equation (B.7):

$$\mathbf{P}^{(2)} = V\mathbf{P}^{(1)}, \qquad S_1 > S_2 \tag{B.8}$$

where V is a matrix with the elements defined by

$$V_{nm} = \frac{1}{S_2}\int_{S_2} \psi_n^{(2)}\psi_m^{(1)} dS \tag{B.9}$$

B.1.2 Volume velocity

In plane wave propagation the continuity condition was that the volume velocity must be equal on S_1 and S_2 meaning that the mass of air flowing out of S_1 equals the flow of mass into S_2 at any given time. This implies that the velocity, which is assumed to be constant over the cross-section, is different on either side because of the difference of cross-sectional area. When we are treating the velocity field accurately in three dimensions it is clear that the velocity on the two surfaces should match and that the velocity into the x-y plane wall on the larger cross-section is zero. For the case where $S_2 > S_1$ we have

$$\begin{aligned} v_z^{(1)} &= v_z^{(2)} \quad \text{on} \quad S_1, \quad S_1 < S_2 \\ v_z^{(2)} &= 0 \quad \text{on} \quad S_2 - S_1, \quad S_1 < S_2 \end{aligned} \tag{B.10}$$

where $S_2 - S_1$ is a shorthand for the x-y plane wall resulting from the part of surface 2 which is not shared with surface 1. In terms of volume velocities this means that $U^{(1)}/S_1 = U^{(2)}/S_2$ on S_1 and $U^{(2)} = 0$ on $S_2 - S_1$. Now we will use equation (2.27) (again ignoring the $\exp(i\omega t)$ time factor) and use the orthogonality of the modes. This time in order to include the fact that the volume velocity is zero on $S_2 - S_1$ we must perform the integration over surface 2:

$$U_n^{(2)} = \int_{S_2} \psi_n^{(2)} v_z^{(2)} dS = \int_{S_1} \psi_n^{(2)} v_z^{(1)} dS + \int_{S_2 - S_1} \psi_n^{(2)} 0 dS = \frac{1}{S_1} \int_{S_1} \psi_n^{(2)} \sum_{m=0}^{\infty} \psi_m^{(1)} U_m^{(1)} dS \tag{B.11}$$

which may be written as

$$U_n^{(2)} = \sum_{m=0}^{\infty} F_{mn} U_m^{(1)} \tag{B.12}$$

where F is given in equation (B.6). It should be noted that the integration in F is this time over the ψ_m on surface 1 and over ψ_n on surface 2, hence m and n in the subscript to F are swapped for equation (B.12). In matrix notation the result is

$$\mathbf{U}^{(2)} = F^{\mathrm{T}} \mathbf{U}^{(1)}, \qquad S_1 < S_2 \tag{B.13}$$

proving equation (2.83). The swapping of indices in F is denoted by the transpose operation represented by the superscript T.

As with the pressure, when $S_1 > S_2$ the volume velocity calculation can be

performed simply be interchanging the labels 1 and 2 giving equation (2.84):

$$\mathbf{U}^{(1)} = V^{\mathrm{T}}\mathbf{U}^{(2)}, \qquad S_1 > S_2. \tag{B.14}$$

with V given in equation (B.9).

B.2 Projection matrix in cylindrical geometry

In polar coordinates equation (B.6) becomes

$$F_{nm} = \frac{1}{\pi R_1^2} \int_0^{R_1} \int_0^{2\pi} \psi_n^{(1)} \psi_m^{(2)} r d\theta dr. \tag{B.15}$$

Substituting in equation (2.48) for $\psi_n(r)$ and performing the integration with respect to θ gives:

$$F_{nm} = \frac{2}{R_1^2 J_0(\gamma_n) J_0(\gamma_m)} \int_0^{R_1} r J_0(\gamma_n r/R_1) J_0(\gamma_m r/R_2) dr. \tag{B.16}$$

This is in the form of the standard integral from equation (A.1) of appendix A. Substituting in the variables: $x = r$, $p = q = 0$, $\alpha = \gamma_n/R_1$ and $\beta = \gamma_m/R_2$ gives

$$F_{nm} = \left(\frac{2}{R_1^2 J_0(\gamma_n) J_0(\gamma_m)} \right) \times \left[\frac{(\gamma_m r/R_2) J_0(\gamma_n r/R_1) J_{-1}(\gamma_m r/R_2) - (\gamma_n r/R_1) J_{-1}(\gamma_n r/R_1) J_0(\gamma_m r/R_2)}{(\gamma_n/R_1)^2 - (\gamma_m/R_2)^2} \right]_{r=0}^{r=R_1}. \tag{B.17}$$

When the evaluation is carried out the contribution when $r = 0$ is zero giving:

$$F_{nm} = \left(\frac{2}{R_1^2 J_0(\gamma_n) J_0(\gamma_m)}\right) \times \frac{(\gamma_m R_1/R_2) J_0(\gamma_n) J_{-1}(\gamma_m R_1/R_2) - (\gamma_n) J_{-1}(\gamma_n) J_0(\gamma_m R_1/R_2)}{(\gamma_n/R_1)^2 - (\gamma_m/R_2)^2}. \quad \text{(B.18)}$$

Now noticing from equation (A.2) that $J_{-1}(x) = -J_1(x)$ and using the fact that γ_n is a zero of J_1 the second term vanishes:

$$F_{nm} = \left(\frac{2}{R_1^2 J_0(\gamma_n) J_0(\gamma_m)}\right) \frac{(\gamma_m R_1/R_2) J_0(\gamma_n) J_1(\gamma_m R_1/R_2)}{(\gamma_m/R_2)^2 - (\gamma_n/R_1)^2}. \quad \text{(B.19)}$$

Expressing this in terms of the ratio of the radii, $\beta = R_1/R_2$ we get

$$F_{nm} = \frac{2\beta\gamma_m J_1(\beta\gamma_m)}{(\beta^2\gamma_m^2 - \gamma_n^2) J_0(\gamma_m)} \quad \text{(B.20)}$$

hence we have proved equation (2.85).

The integration used to obtain the analytical expression for V_{nm} is identical to that for F_{nm} except that the labels are interchanged for surface 1 and surface 2. Interchanging R_1 and R_2 means that $\beta = R_1/R_2$ will be replaced with $1/\beta = R_2/R_1$ giving $V_{nm}(\beta) = F_{nm}(1/\beta)$.

Appendix C

Inductance method

The inductance method due to Kergomard and Garcia [57] is reviewed here. The multimodal method was treated and the results used to get a polynomial for the frequency dependent inductance, L, so that the formula

$$p_1 = p_2 + i\omega LU, \qquad U_1 = U_2 = U \tag{C.1}$$

matches the multimodal treatment when $0.05 < R_1/R_2 < 0.95$ and $0.001 < kR_2 < 3.5$. Here p_1 is the pressure immediately to the left of the discontinuity and p_2 is the pressure immediately to the right of the discontinuity. U is the volume velocity, matched on both sides as with the plane wave approximation. The pressures and volume velocity are scalars here, not vectors since the multimodal effects are represented by the inductance.

Now we will work out the reflectance for a plane wave incident on a discontinuity between two infinite cylinders. We do this by expressing both the equations in (C.1) in terms of forward and backward going waves and solving. The pressure on the left is the sum of incident and reflected waves: $p_1 = p_1^+ + p_1^-$. The pressure on the right is simply the transmitted term $p_2 = p_2^+$.

The volume velocity on the left is then

$$U_1 = (p_1^+ - p_1^-)(S_1/\rho c) \tag{C.2}$$

while on the right the volume velocity is

$$U_2 = p_2^+(S_2/\rho c). \tag{C.3}$$

From equation (C.1) the volume velocity is the same on each side of the discontinuity for this method giving:

$$p_2^+ = (p_1^+ - p_1^-)(S_1/S_2). \tag{C.4}$$

Now we turn to the first part of equation (C.1). Substituting in the pressure as the sum of the forward and backward going waves and putting $U = U_1 = (p_1^+ - p_1^-)(S_1/\rho c)$ gives

$$p_1^+ + p_1^- = p_2^+ + i\omega L(p_1^+ - p_1^-)(S_1/\rho c). \tag{C.5}$$

In order to work out the reflectance we need to remove p_2^+ to obtain an expression featuring only p_1^+ and p_1^-. We therefore substitute p_2^+ from equation (C.4) into equation (C.5).

$$p_1^+ + p_1^- = (p_1^+ - p_1^-)(S_1/S_2) + i\omega L(p_1^+ - p_1^-)(S_1/\rho c). \tag{C.6}$$

Rearranging we get the reflection coefficient, the ratio of the reflected and incident waves:

$$\frac{p_1^-}{p_1^+} = \frac{(S_1/S_2) - 1 + i\omega L(S_1/\rho c)}{(S_1/S_2) + 1 + i\omega L(S_1/\rho c)}. \tag{C.7}$$

As with the multimodal method this may be expressed in terms of dimensionless variables kR_1 and $\beta = R_1/R_2$;

$$\frac{p_1^-}{p_1^+} = \frac{\beta^2 - 1 + i\pi(kR_1)(LR_1/\rho)}{\beta^2 + 1 + i\pi(kR_1)(LR_1/\rho)} \tag{C.8}$$

where LR_1/ρ is a function of the dimensionless variables and is tabulated in table 2 (A) of [57]. This formula is used to calculate the inductance method reflectance shown in figure 6.1 of section 6.4.

Bibliography

[1] D. M. Campbell and C. A. Greated. *The musician's guide to acoustics*. Dent, 1987.

[2] D. M. Campbell. Nonlinear dynamics of musical reed and brass wind instruments. *Contemporary Physics*, 40(6):415–431, 1999.

[3] J. Backus. Input impedance curves for the reed woodwind instruments. *J. Acoust. Soc. Am.*, 56(4):1266–1279, 1974.

[4] J. Backus. Acoustic impedance of an annular capillary. *J. Acoust. Soc. Am.*, 58(5):1078–1081, 1975.

[5] J. Backus. Input impedance curves for the brass instruments. *J. Acoust. Soc. Am.*, 60(2):470–480, 1976.

[6] D. B. Sharp. *Acoustic pulse reflectometry for the measurement of musical wind instruments*. PhD thesis, University of Edinburgh, 1996.

[7] J. A. Ware and K. Aki. Continuous and discrete inverse scattering problems in a stratified elastic medium. i: Planes at normal incidence. *J. Acoust. Soc. Am.*, 45(4):911–921, 1969.

[8] M. M. Sondhi and B. Gopinath. Determination of vocal-tract shape from impulse response at the lips. *J. Acoust. Soc. Am.*, 49(6):1867–1873, 1971.

[9] M. M. Sondhi and J. R. Resnick. The inverse problem for the vocal tract: numerical methods, acoustical experiments and speech synthesis. *J. Acoust. Soc. Am.*, 73(3):985–1002, 1983.

[10] A. C. Jackson, J. P. Butler, E. J. Millet, F. G. Hoppin, and S. V. Dawson. Airway geometry by analysis of acoustic pulse response measurements. *J. Appl. Physiol.*, 43(3):523–536, 1977.

[11] A. C. Jackson and D. E. Olsen. Comparison of direct and acoustical area measurements in physical models of human central airways. *J. Appl. Physiol.*, 48(5):896–902, 1980.

[12] J. J. Fredberg, M. E. B. Wohl, G. M. Glass, and H. L. Dorkin. Airway area by acoustic reflections measured at the mouth. *J. Appl. Physiol.*, 48(5):749–758, 1980.

[13] L. J. Brooks, R. G. Castile, G. M. Glass, and N. T. Griscom. Reproducibility and accuracy of airway area by acoustic reflection. *J. Appl. Physiol.*, 57(3):777–787, 1984.

[14] A. H. Benade and J. H. Smith. Brass wind instrument impulse response measurements. *J. Acoust. Soc. Am.*, 70:S22, 1981.

[15] R. A. Smith. It's all in the bore! *Journal of the International Trumpeters Guild*, 12:42–45, 1988.

[16] A. P. Watson and J. M. Bowsher. Impulse measurements on brass musical instruments. *Acustica*, 66:170–174, 1988.

[17] N. Amir, G. Rosenhouse, and U. Shimony. A discrete model for tubular acoustic systems with varying cross section - the direct and inverse problems. parts 1 and 2: Theory and experiment. *Acustica*, 81:450–474, 1995.

[18] N. Amir, G. Rosenhouse, and U. Shimony. Losses in tubular acoustic systems - theory and experiment in the sampled time and frequency domains. *Acustica*, 82:1–8, 1996.

[19] D. B. Sharp and D. M. Campbell. Leak detection in pipes using acoustic pulse reflectometry. *Acustica*, 83:560–566, 1997.

[20] D. B. Sharp, A. Myers, R. Parks, and D. M. Campbell. Bore reconstruction by pulse reflectometry and its potential for the taxonomy of brass instruments. In *Proc. 15th International Congress on Acoustics, Trondheim, Norway*, pages 481–484, 1995.

[21] A. H. Benade and E. V. Jansson. On plane and spherical waves in horns with nonuniform flare. 1. theory of radiation, resonance frequencies, and mode conversion. *Acustica*, 31:79–98, 1974.

[22] P. M. Morse and K. U. Ingard. *Theoretical Acoustics*. McGraw-Hill, 1st edition, 1968.

[23] E. Eisner. Complete solution of the webster horn equation. *J. Acoust. Soc. Am.*, 41(4):1126–1146, 1967.

[24] G. R. Putland. Every one-parameter acoustic field obeys webster's horn equation. *J. Audio Eng. Soc.*, 41(6):435–451, 1993.

[25] J. W. Miles. The reflection of sound due to a change in cross section of a circular tube. *J. Acoust. Soc. Am.*, 16(1):14–19, 1944.

[26] J. W. Miles. The analysis of plane discontinuities in cylindrical tubes. part 1. *J. Acoust. Soc. Am.*, 17(3):259–271, 1946.

[27] J. W. Miles. The analysis of plane discontinuities in cylindrical tubes. part 2. *J. Acoust. Soc. Am.*, 17(3):272–284, 1946.

[28] A. F. Stevenson. Exact and approximate equations for wave propagation in acoustic horn. *Journal of Applied Physics*, 22(12):1461–1463, 1951.

[29] A. F. Stevenson. General theory of electromagnetic horns. *Journal of Applied Physics*, 22(12):1447–1460, 1951.

[30] R. J. Alfredson. The propagation of sound in a circular duct of continuously varying cross-sectional area. *Journal of Sound and Vibration*, 23(4):433–442, 1972.

[31] S. Oie, R. Takeuchi, and T. Shindo. Sound radiation from a concave radiator in an infinite baffle. *Acustica*, 46:268–275, 1980.

[32] V. Pagneux, N. Amir, and J. Kergomard. A study of wave propagation in varying cross-section waveguides by modal decomposition. part 1. theory and validation. *J. Acoust. Soc. Am.*, 100(4):2034–2048, 1996.

[33] N. Amir, V. Pagneux, and J. Kergomard. A study of wave propagation in varying cross-section waveguides by modal decomposition. part 2. results. *J. Acoust. Soc. Am.*, 101(5):2504–2517, 1997.

[34] H. Levine and J. Schwinger. On the radiation of sound from an unflanged circular pipe. *Physical review*, 73(4):383–406, 1948.

[35] Y. Ando. On the sound radiation from semi-infinite circular pipe of certain wall thickness. *Acustica*, 22:219–225, 1969-1970.

[36] Y. Ando and T. Koizumi. Sound radiation from a semi-infinite circular pipe having an arbitrary profile of orifice. *J. Acoust. Soc. Am.*, 59(5):1033–1039, 1976.

[37] W. E. Zorumski. Generalized radiation impedances and reflection coefficients of circular and annular ducts. *J. Acoust. Soc. Am.*, 54(6):1667–1673, 1973.

[38] J. A. Kemp, N. Amir, and D. M. Campbell. Calculation of input impedance including higher modes. In *Proc. 5th French Congress on Acoustics, Lausanne, Switzerland*, pages 314–317, 2000.

[39] J. A. Kemp, D. M. Campbell, and N. Amir. Multimodal radiation impedance of a rectangular duct terminated in an infinite baffle. *Acustica*, 87:11–15, 2001.

[40] L. E. Kinsler, A. R. Frey, A. B. Coppens, and J. V. Sanders. *Fundamentals of acoustics*. Wiley, 3rd edition, 1982.

[41] J. A. Kemp, N. Amir, D. M. Campbell, and M. van Walstijn. Multimodal propagation in acoustic horns. In *Proc. International Symposium on Musical Acoustics (ISMA), Perugia, Italy*, pages 521–524, 2001.

[42] J. Kergomard. Calculation of discontinuities in waveguides using mode-matching method: an alternative to the scattering matrix approach. *J. Acoustique*, 4:111–138, 1991.

[43] K. F. Riley, M. P. Hobson, and S. J. Bence. *Mathematical methods for physics and engineering*. Cambridge University Press, 1st edition, 1998.

[44] A. M. Bruneau, M. Bruneau, Ph. Herzog, and J. Kergomard. Boundary layer attenuation of higher order modes in waveguides. *Journal of Sound and Vibration*, 119(1):15–27, 1987.

[45] N. H. Fletcher and T. D. Rossing. *The physics of musical instruments.* Springer, 1st edition, 1991.

[46] Lord Rayleigh. *Theory of sound.* Macmillan, 1940.

[47] J. Lee and I. Seo. Radiation impedance computations of a square piston in a rigid infinite baffle. *Journal of Sound and Vibration*, 198(3):299–312, 1996.

[48] D. S. Burnett and W. W. Soroka. Tables of rectangular piston radiation impedance functions, with application to sound transmission loss through deep apertures. *J. Acoust. Soc. Am.*, 51(2):1618–1623, 1972.

[49] Jr. G. W. Swenson and W. E. Johnson. Radiation impedance of a rigid square piston in an infinite baffle. *J. Acoust. Soc. Am.*, 24(1):84, 1952.

[50] E. M. Arase. Mutual radiation impedance of square and rectangular pistons in a rigid infinite baffle. *J. Acoust. Soc. Am.*, 36(8):1521–1525, 1964.

[51] H. Levine. On the radiation impedance of a rectangular piston. *Journal of Sound and Vibration*, 89(4):447–455, 1983.

[52] G. N. Watson. *A treatise on the theory of Bessel functions.* Cambridge University Press, 2nd edition, 1962.

[53] H. Nelisse, O. Beslin, and J. Nicolas. A generalised approach for the acoustic radiation from a baffled or unbaffled plate with arbitrary boundary conditions, immersed in a light or heavy fluid. *Journal of sound and vibration*, 211(2):207–225, 1998.

[54] D. H. Keefe. Acoustical wave propagation in cylindrical ducts: Transmission line parameter approximations for isothermal and nonisothermal boundary conditions. *J. Acoust. Soc. Am.*, 75(1):58–62, 1984.

[55] E. Kreyszig. *Advanced engineering mathematics.* Wiley, 7th edition, 1993.

[56] J. M. Buick, J. A. Kemp, D. B. Sharp, M. van Walstijn, D. M. Campbell, and R. A. Smith. Distinguishing between similar tubular objects using pulse reflectometry: a study of trumpet and cornet leadpipes. *Measurement Science Technology*, 13:750–757, 2002.

[57] J. Kergomard and A. Garcia. Simple discontinuities in acoustical waveguides at low frequencies: critical analysis and formulae. *Journal of Sound and Vibration*, 114(3):465–479, 1987.

[58] M. M. Boone, G. Janssen, and M. van Overbeek. Modal superposition in the time domain: Theory and experimental results. *J. Acoust. Soc. Am.*, 97(1):92–97, 1995.

[59] F. de Coulon. *Signal theory and processing.* Artech House Inc., 1st edition, 1986.

[60] M. van Walstijn, J. A. Kemp, N. Amir, and D. M. Campbell. Acoustic bore reconstruction using the layer-peeling algorithm: signal processing aspects and future development involving the inclusion of higher modes. In *Proc. 17th International Congress on Acoustics, Rome, Italy*, 2001.

[61] W. Kausel. Bore reconstruction from measured acoustical input impedance; equipment, signal processing, algorithms and prerequisites. In *Proc. International Symposium on Musical Acoustics (ISMA), Perugia, Italy*, pages 373–378, 2001.

[62] J. A. Kemp, J. M. Buick, and D. M. Campbell. Practical improvements to acoustic pulse reflectometry: the virtual dc tube method and source reflection cancellation. In *Proc. International Symposium on Musical Acoustics (ISMA), Perugia, Italy*, pages 387–390, 2001.

[63] B. Louis, G. Glass, B. Kresen, and J. Fredberg. Airway area by acoustic reflection: the two-microphone method. *Journal of Biomechanical Engineering*, 115:278–285, 1993.

[64] D. B. Sharp. Increasing the length of tubular objects that can be measured using acoustic pulse reflectometry. *Measurement Science Technology*, 9:1469–1479, 1998.

[65] K. C. Hsu. *Simulation of room acoustics.* Undergraduate thesis, University of Queensland, Australia, 1996. (Downloadable from website http://www.elec.uq.edu.au/~marks/thesis/thesis96/hsu/).

[66] M. R. Schroeder. Integrating-impulse method measuring sound decay without using impulses. *J. Acoust. Soc. Am.*, 66(2):497–500, 1979.

[67] W. T. Chu. Impulse-response and reverberation-decay measurements made by using a periodic pseudorandom sequence. *Applied Acoustics*, 29:193–205, 1990.

[68] F. J. MacWilliams and N. J. A. Sloane. Pseudo-random sequences and arrays. *Proceedings of the IEEE*, 64(12):1715–1729, 1976.

[69] W. Stahnke. Primitive binary polynomials. *Mathematics of Computation*, 27:977–980, 1973.

[70] J. Borish and J. B. Angell. An efficient algorithm for measuring the impulse response using pseudorandom noise. *Journal of the Audio Engineering Society*, 31(7):478–487, 1983.

[71] M. van Walstijn and D. M. Campbell. Large-bandwidth measurement of acoustic input impedance of tubular objects. In *Proc. Institute of Acoustics Spring Conference, Salford, UK*, 2002.

[72] B. J. Forbes, D. B. Sharp, and J. A. Kemp. Acoustic pulse reflectometry: singular system analysis and regularisation of the inverse problem. In *Proc. Institute of Acoustics Spring Conference, Salford, UK*, 2002.

[73] E. Jahnke and F. Emde. *Tables of functions with formulae and curves*. Dover, 4th edition, 1945.